Impact of Micro-TO Meso-scale Fractures on Sealing Behavior of Argillaceous Cap Rocks For CO2 Sequestration

FINAL REPORT

Dates

PRINCIPAL AUTHOR

PA/PI: James P. Evans
(435) 797-1267 james.evans@usu.edu

August 2015

AWARD NUMBER

DE-SC0004991

SUBMITTED BY

Utah State University
1400 Old Main Hill
Logan, Utah 8432201400

DISCLAIMER

INTRODUCTION

This multi-disciplinary project evaluated seal lithologies for the safety and security of long-term geosequestration of CO_2. We used integrated studies to provide qualitative risk for potential seal failure; we integrated data sets from outcrop, core, geochemical analysis, rock failure properties from mechanical testing, geophysical wireline log analysis, and geomechanical modeling to understand the effects of lithologic heterogeneity and changing mechanical properties have on the mechanical properties of the seal.

The objectives of this study were to characterize cap rock seals using natural field analogs, available drillhole logging data and whole-rock core, geochemical and isotopic analyses. Rock deformation experiments were carried out on collected samples to develop better models of risk estimation for potential cap rock seal failure. We also sampled variably faulted and fractured cap rocks to examine the impacts of mineralization and/or alteration on the mechanical properties. We compared CO_2 reacted systems to non-CO_2 reacted seal rock types to determine response of each to increased pore fluid pressures and potential for the creation of unintentional hydrofractures at depth.

MAJOR RESULTS

We examined the potential impact on CO_2 transport of zones of deformation bands in reservoir rock that transition to opening-mode fractures within overlying caprocks. We performed sedimentological and petrophysical measurements were collected along an approximately 5 m x 5 m outcrop of the Slick Rock and Earthy Members of the Entrada Sandstone on the eastern flank of the San Rafael Swell, Utah, USA. Measured deformation band permeability (2 mD) within the reservoir facies is about three orders of magnitude lower than the host sandstone. Average permeability of the caprock facies (0.0005 mD) is about seven orders of magnitude lower than the host sandstone. Aperture-based permeability estimates of the opening-mode caprock fractures are high (3.3 9 107 mD). High-resolution CO_2–H_2O transport models incorporate these permeability data at the millimeter scale. We varied fault properties at the reservoir/caprock interface between open fractures and deformation bands as part of a sensitivity study. Numerical modeling results suggest that zones of deformation bands within the reservoir strongly compartmentalize

reservoir pressures largely blocking lateral, cross-fault flow of supercritical CO_2. Significant vertical CO_2 transport into the caprock occurred in some scenarios along opening-mode fractures. The magnitude of this vertical CO_2 transport depends on the small-scale geometry of the contact between the opening mode fracture and the zone of deformation bands, as well as the degree to which fractures penetrate caprock. The presence of relatively permeable units within the caprock allows storage of significant volumes of CO_2, particularly when the fracture network does not extend all the way through the caprock.

(Petrie et al. 2014) use laboratory determined tensile and compressive rock strength data from analog clastic rocks to determine their modified Coulomb-Griffith failure envelopes. We examine and model the effect changes in mechanical rock properties have on fracture gradients and the potential for failure at depth under conditions of increased pore pressure. We combine these mechanical properties with fracture gradient analysis for two injection scenarios using injection depth and maximum injection pressures from UIC wells in Ohio and Oklahoma.

Material properties for each rock type results in a different failure envelope shape. These failure envelopes can be used to predict/understand the type of mechanical failure and the conditions under which failure will occur because of increased pore fluid pressure. Incorporating tensile strength into fracture gradient prediction changes the slope of the fracture gradient. Modified Mohr-Coulomb-Griffith modeling, using rock
properties derived from geomechanical testing at depths associated with UIC wells, shows that the max injection pressures can exceed effective stress necessary to induce failure.

1) Cohesionless materials fail very near hydrostatic pressures
2) Cohesionless materials fail in shear
3) A combination of low differential stress and high "relative" tensile strength results is tensile failure
4) Differential stress and rock properties (failure envelope shape) play a role in development of shear, hybrid, or tensile failure.
5) Predictions presented here are made at the borehole –pressure changes some distance away from the site of injection may also result in mechanical rock failure especially if encountering a cohesionless pre-existing fracture or critically stressed fault.

Maximum injection pressure data and depth of injection are based on publicly available databases of UIC Class II wells. The calculations for various fracture gradients account for the existing pore fluid pressure in the zone of interest, we have assumed this to be hydrostatic pressure. Future work will focus on the incorporation of existing/current pressure gradients to better quantify P_{fpmax} and evaluate rock failure at depth.

(Petrie and Evans, in press) characterize the variability in rock strength and the associated changes in subsurface strain distribution that is especially important for modeling the response of low-permeability rocks to changes in effective stress. This paper documents the effect variations in elastic mechanical properties have on the nature and distribution of fractures in the subsurface. Outcrop and geophysical wireline log evaluation

of the Jurassic Carmel Formation and Navajo Sandstone was used to identify mechano-stratigraphic units and model subsurface strain distribution within sedimentary successions and across sedimentary interfaces.

Two finite element models were constructed and populated with elastic moduli derived from geophysical wireline data in order to understand where natural fractures form in rocks with varying layer thickness and elastic properties. Strain distribution results from a 3 layer and a 5-layer model are compared to the natural deformation response visible in outcrop. We show that more fractures are expected in high strain regions and fewer fractures in low strain regions. Strain variations are observed in both model scenarios and occur at material interface. The simple 3-layer model results in a smoothing of strain variations, while the 5-layer model captures strain variations that more closely match the fracture density observed in outcrop. Results from the 5-layer model suggests an interplay between Young's modulus and Poisson's ratio and that high strain regions form in thin (1-m thick) layers with moderate Young modulus (17.2 GPa) and Poisson ratio (0.26) values.

Outcrop observations and modeling results indicate that the potential for subsurface failure and fluid flow would not be restricted to the low fracture strength units but can cut vertically across interfaces of varying mechanical strength. Results from this work indicates that these types of models can be used to identify stratigraphic layers that are more prone to mechanical failure or identify layers that have more natural fractures or are more likely to form induced fractures.

(Kampman et al. 2014) present the initial results of a scientific drilling project to recover core and pressurized fluid samples from a natural CO_2 reservoir, near the town of Green River, Utah. The drilling targeted a stacked sequence of CO_2-charged Jurassic sandstone reservoirs and caprocks, situated adjacent to a CO_2 degassing normal fault. This site has actively leaked CO_2 from deep supercritical CO_2 reservoirs at depth ~2 km within the basin for over 400,000 years. The project objectives were to gather samples to examine reactive fluid flow in the reservoirs, caprocks and faults, during migration of CO_2 through the geological overburden from the deep supercritical CO_2 reservoirs. Downhole fluid sampling and fluid element and isotope geochemistry show that the shallow reservoirs are being actively fed by inflow of CO_2-saturated brines through the faults. Comparisons of shallow and deep fluid geochemistry suggest that: (i) CO_2 and CO_2-charged brines co-migrated from the deep reservoirs, (ii) the CO_2 saturated brines migrating from depth interact with significant volumes of meteoric groundwater in aquifers in the shallower Permian and Jurassic sandstones, diluting the brine composition, and (iii) that a significant fraction of the CO_2 migrating from depth is dissolved in these brine–meteoric water mixtures, with 99% of the CO_2 in fluids sampled from the shallow reservoirs being derived during fluid migration, after the fluids left their source reservoir. The $^{87}Sr/^{86}Sr$ ratio of the brine flowing through the faults is significantly elevated due to the addition of Sr from silicate mineral dissolution during fluid migration. The association of bleached sandstones in the core with CO_2-rich fluids supports interpretations from elsewhere that CO_2-charged brines with CH_4 or H_2S reductants can dissolve hematite present within the sediment. Analysis of fluid geochemistry and sandstone petrology suggests that the CO_2-rich fluids

dissolve carbonate, hematite and gypsum in the reservoirs, as they flow away from the faults.

Element and isotope geochemistry of fluid samples from the drillhole and Crystal Geyser constrain mixing models which show that, within the Navajo Sandstone, the reservoir fluids are undergoing complex mixing of: (i) CO_2-saturated brine inflowing from the fault, (ii) CO_2-undersaturated meteoric groundwater flowing through the reservoir and (iii) reacted CO_2-charged brines flow through fracture zones in the overlying Carmel Formation caprock, into the formations above. Such multi-scale mixing processes may significantly improve the efficiency with which groundwaters dissolve the migrating CO_2.

(Kampman et al. 2016) examined mineral reaction fronts in a CO_2 reservoir-caprock system exposed to CO_2 over a timescale comparable with that needed for geological carbon storage. The propagation of the reaction front is retarded by redox-sensitive mineral dissolution reactions and carbonate precipitation, which reduces its penetration into the caprock to 7 cm in 10^5 years. This distance is an order-of-magnitude smaller than previous predictions. The results attest to the significance of transport-limited reactions to the long-term integrity of sealing behaviour in caprocks exposed to CO_2.

LIST OF PAPERS supported by this research

In Press

Petrie, E. S., Evans, J. P., Bauer, S. J., Modeling the impact of mechanical interfaces to natural fracture propagation and morphology – geomechanical models derived from outcrop analysis, Canadian Society of Petroleum Geologists Bulletin, in press.

Zhang, Y., Edel, S. S., Pepin, J., Person, M., Broadhead, R., Stone, W., Bilek, S. L., Mozley, P. S., Evans, J. P., in revision, Exploring the Potential Linkages Between Oil-Field Brine Reinjection, Crystalline Basement Permeability, and Triggered Seismicity for the Dagger Draw Oil Field, Southeastern New Mexico, USA Using Hydrologic Modeling, Geofluids.

Published papers based on this research

Kampman, N., Busch, A. Bertier, P., Snippe, J., Hangx, S., Pipich, V, Di, Z., Rother, G., Harrington, J. F., Evans, J. P., Maskell, A., , Chapman, H. J., Bickle, M. J., 2016, Observational evidence confirms modeling of the long-term integrity of CO_2-reservoir caprocks, Nature Communications, 7.

Raduha, S., D Butler, D., PS Mozley, P. S., Person, M., Evans, J. P., Heath, J. E., Dewers, T. A. Stauffer, P. H., Gable, C. W., Kelkar, S., 2016, Potential seal bypass and caprock storage produced by deformation-band-to-opening-mode-fracture transition at the reservoir/caprock interface, Geofluids, DOI: 10.1111/gfl.12177.

Chen, X., Schmitt, D. R., Kessler, J. A., Evans, J. P., Kofman, R., 2015, Empirical relations between ultrasonic P-wave velocity, porosity and Uniaxial Compressive Strength, CSEG Recorder, v. 40, p. 24-29.

Petrie, E. S., Evans, J. P., Bauer, S. J., 2014, Failure of caprock seals as determined from mechanical stratigraphy, stress history and tensile failure analysis of exhumed analogs. AAPG Bulletin, v. 98, p. 2365-2389.

Busch, A. Kampman, N., Hangx, S. J., Snippe, J., Bickle, M., Bertier, P., ,Chapman, H., Spiers, C. J., Pijnenburg, Samuelson, R. J., Evans, J. P., Maskell, A., Nicholl, J., Pipich, V., Di, Z., Rother, G., Schaller, M., 2014, The Green River Natural Analogue as A Field Laboratory To Study the Long-term Fate of CO_2 in the subsurface, Energy Procedia, v. 63, p. 2821-2830.

Kampman, N.,Maskell, A., Bickle, M. J., Evans, J. P.,Schaller, M., Purser, G., Zhou, Z., Gattacceca, J., Petrie, E. S.,Rochelle,C. A., Ballentine, C. J., Busch, A. , 2014, Drilling and sampling a natural CO_2 reservoir: Implications for fluid flow and CO_2-fluid–rock reactions during CO_2 migration through the overburden, Chemical Geology 369, 51-82

PERCENTAGE OF GRANT TO EACH PROJECT PARTICIPANT

Elizabeth Petrie: 40%
Dan Curtis: 20%
Eric Rassmussen: 15%
Santiago Florez: 15%
James Evans: 10%

Exploring the Potential Linkages Between Oil-Field Brine Reinjection, Crystalline Basement Permeability, and Triggered Seismicity for the Dagger Draw Oil Field, Southeastern New Mexico, USA Using Hydrologic Modeling

[1]Yipeng Zhang, [1]Stanislav S. Edel, [1]Jeff Pepin, *[1]Mark Person, [2]Ron Broadhead, [1]John P. Ortiz, [1]Susan L. Bilek, [1]Peter Mozley, and [3]James P. Evans

[1] New Mexico Tech
[2] New Mexico Bureau of Geology & Mineral Resources
[3] Utah State University
[*] *Corresponding Author*

Submitted: January 26, 2016, Revised: July 30, 2016

Abstract

We used hydrologic models to explore the potential linkages between oil-field brine reinjection and increases in earthquake frequency (up to M_d 3.26) in southeastern New Mexico and to assess different injection management scenarios aimed at reducing the risk of triggered seismicity. Our analysis focuses on saline water re-injection into the basal Ellenburger Group beneath the Dagger Draw Oil field, Permian Basin. Increased seismic frequency (>M_d 2) began in 2001, five years after peak injection, at an average depth of 11 km within the basement 15 km to the west of the reinjection wells. We considered several scenarios including assigning an effective or bulk permeability value to the crystalline basement, including a conductive fault zone surrounded by tighter crystalline basement rocks, and allowing permeability to decay with depth. We initially adopted a 7 m (0.07 MPa) head increase as the threshold for triggered seismicity. Only two scenarios produced excess heads of 7m five years after peak injection. In the first, a hydraulic diffusivity of 0.1 $m^2 s^{-1}$ was assigned to the crystalline basement. In the second, a hydraulic diffusivity of 0.3 $m^2 s^{-1}$ was assigned to a conductive fault zone. If we had considered a wider range of threshold excess heads to be between 1-60m, then the range of acceptable hydraulic diffusivities would have increased (between 0.1-0.01 $m^2 s^{-1}$ and 1-0.1 $m^2 s^{-1}$ for the bulk and fault zone scenarios, respectively). A permeability-depth decay model would have also satisfied the 5-year time lag criterion. We also tested several injection management scenarios including redistributing injection volumes between various wells and lowering the total volume of injected

fluids. Scenarios that reduced computed excess heads by over 50% within the crystalline basement resulted from reducing the total volume of reinjected fluids by a factor of 2 or more.

Introduction

Zhang et al. (2013) proposed that injection of oil field brines into basal sedimentary rock reservoirs represents a key geologic factor related to triggered seismicity within the underlying crystalline basement. Fluid injection into a permeable, horizontally extensive reservoir allows for the rapid radial propagation of elevated fluid pressures outward from injection wells. In the absence of a basal confining unit, basal reservoir injection maximizes the amount of crystalline basement surface area exposed to elevated fluid pressures. If elevated fluid pressures within a basal reservoir encounter a relatively high permeability fault (e.g. 10^{-14} m^2) or if the bulk permeability of the crystalline basement is moderately high (10^{-15} to 10^{-16} m^2), then fluid pressures can propagate downward over a period of a few years and laterally away from the injection site. If elevated fluid pressures come into contact with a critically stressed fault, only a small pressure increase is needed to trigger seismicity (Barton et al., 1995; Townend and Zoback, 2000).

Large, damaging, triggered earthquakes typically occur at depths of 4-6 km within the crystalline basement and up to 10-15 km away from the injection site (e.g. Keranen et al., 2013, 2014; Walsh and Zoback, 2015). The association between basal reservoir injection and induced seismicity within the underlying crystalline basement has been documented at a number of sites in Oklahoma and Arkansas (Table 1; Fig. 1; Keranen et al. 2013, 2014; Horton, 2012). There are also a number of instances of induced seismicity where injection occurred directly into the crystalline basement, such as in Ohio and Colorado (Fig. 1; Table 1, Hsieh and Bredehoeft, 1981; Kim, 2012).

Prior studies have reported a wide range of fluid pressure increases thought to be associated with triggered seismicity (Table 1). Hsieh and Bredehoeft (1981) found that the pressure threshold associated with triggered seismicity at the Rocky Mountain Arsenal near Denver was 320 m (3.2 MPa) at an average depth of about 5 km within the crystalline basement. Kerenan et al. (2014) concluded that a pore pressure increase of 0.07MPa was consistent with triggered seismicity in Oklahoma. Ge et al. (2009) estimated that filling of the Zipingpu dam with 200 m head of water (2 MPa) resulted in a relatively small head change of 2.5 to 5 m (0.025 – 0.05 MPa) at depths of 10-20 km below the land surface near the Wenchuan earthquake foci. Saar and Manga (2003) concluded that even smaller head changes (about 1 m or 0.01 MPa) were required to explain hydraulically induce earthquake swarms 4.5 km below Mt. Hood. Although oil-field operators are required to report injection pressures at the wellhead, this doesn't provide much insight into pore pressures deep within the crystalline basement where earthquakes occur. Most of the studies described above have had to rely on mathematical modeling to infer critical pressure conditions within the crystalline basement associated with induced seismicity due to the dearth of available pore pressure data.

Crystalline basement rock permeability can be inferred using variety of methods, including hydraulic tests from deep boreholes (Brace, 1984; Stober and Butcher, 2007; Fig. 2), fracture aperture measurements on outcrops (Snow, 1968; Caine and Tomusiak,

2003; Klimczak et al. 2010), and temperature anomalies associated with regional groundwater flow systems within the crystalline basement (e.g. Forster and Smith, 1989; Mailloux et al. 1999; Manning and Caine, 2007; Pepin et al. 2015). Synthesis studies of deep borehole hydraulic tests suggest that crustal permeability is scale dependent (Clauser, 1992) and decays with depth (Stober and Butcher, 2007) with non-negligible (10^{-18} to 10^{-19} m^2) permeability below the brittle-ductile transition (Manning and Ingebritsen, 1999; Ingebritsen and Gleeson, 2015; Fig. 2 curve A). Townend and Zoback (2000) argued that the presence of hydrostatic pressure conditions and numerous observations of temperature anomalies associated with fracture planes in deep boreholes indicates bulk permeability of crystalline basement rocks ranging between 10^{-16} and 10^{-17} m^2 on average. Petrologists, economic geologists and geophysicists have argued for some time that permeability can behave dynamically within the crystalline basement. This transience takes the form of permeability increases due to seismic activity followed by permeability reductions as a result of fluid-rock interactions, such as pressure solution and mineral precipitation (Lowell et al. 1993; Manga et al. 2012). Ingebritsen and Manning (2010) proposed that geologic forcing (e.g. regional tectonic stress) could increase crustal permeability by about 2 orders of magnitude (Fig. 2, curve B). It seems likely that the injection of large volumes of oil field brines into basal reservoirs may provide hydrogeologists with new opportunities to constrain dynamic crystalline basement permeability.

Southeastern New Mexico has experienced increased seismicity between 1999-2012 within the Permian basin adjacent to the Dagger Draw oil field (Edel et al. 2016; Fig. 3-4). Seismicity within the crystalline basement in this region occurs at depths that range from 5 to 19 km, with a mean depth of 11 km (Edel et al. 2016; Fig 1A). The epicenter of the seismicity occurs about 85 km from the low-level nuclear Waste Isolation Pilot Plant near Carlsbad, NM (WIPP, blue circle in Fig. 3a). Beneath the Dagger Draw oil field, saline water is injected into the basal Ellenburger carbonate reservoir, which rests unconformably on the crystalline basement. There are relatively high injection rates (over 1 million barrels per month) in wells within 20 km of the seismic cluster (Fig. 4b). In their analysis of seismicity across the USA, Weingarten et al. (2015) inferred from analysis of regional data sets that there is a significant correlation between induced seismicity and high injection rates (> 300,000 barrels per month). The relationship between seismicity and brine injection is less straightforward in southeastern New Mexico than with some of the above examples listed in Table 1. Typically, one expects to see a close temporal correlation between seismicity and fluid injection (e.g. Hsieh and Bredehoeft, 1981). In the case of the Dagger Draw oil field, peak injection occurred in 1996. Seismicity increased around 2001, 5 years after peak injection (Fig. 4a). Limited regional seismic observations go back to the mid-1970s, with a larger network of 7-9 stations in place by 1998. Relocation of recent seismicity suggests hypocenters in this region are deeper (Fig. 5) than any of the other published instances of triggered seismicity (Table 1). Finally, the hypocenter of the seismicity is not directly beneath the oil field but is 15 km to the west (Figs. 1 and 3). Many of the epicenters line up in a

more or less north-south trend (Fig. 3a, Fig. 5). In some scenarios presented below, we consider the effects of a north-south oriented conductive fault zone west of the Dagger Draw oil field.

Dagger Draw Oil Field Geology, Production and Injection History

The Dagger Draw oil field lies on the edge of the Permian Basin in southeastern New Mexico. Production began in 1969 (Fig. 4a) primarily out of the Canyon (Missourian) and Cisco (Virgilian) Groups that, in the Dagger Draw field, consist of upper Pennsylvanian reefal limestones (Broadhead, 1999). The oil is stratigraphically trapped in this carbonate unit and overlain by low-permeability shales in the Permian Hueco Fm. and underlain by the Barnett and Woodford shales (Fig. 6; Broadhead, 1999). There are currently 138 producing wells in the Dagger Draw field, down from a peak of 414 producing wells in 2001 (GoTech; New Mexico Oil Conservation Division database). About 2-3 times as much brine is produced as oil by volume (Fig. 4a), generally appearing as brackish water with TDS contents between 4,000 and 10,000 mg/l and a maximum salinity in some areas as high as 309,000 mg/l (Balch and Muraleedharan, 2014).

Produced oil-field brine is primarily injected into the basal Ellenburger Group. There is also some injection of oil-field brines into the overlying Montoya, Fusselman and Wristen carbonate units. Within the Dagger Draw oil field, permitted wellhead injection pressures for these formations range between about 1,520 m and 1,670 m for reservoir

depths ranging between 3.3 and 3.6 km (New Mexico Oil Conservation Division, 2016). The Ellenburger thickness in New Mexico ranges from about 1 to 70 m (Holtz and Kerans, 1992). Ellenburger Limestone thickness increases to the southeast in Texas (Fig. 6; Wright, 1979). Porosity varies from 0.01 to 0.2 with an average of about 0.06. Core permeability values range from 2 to 100 mD (10^{-15} to 10^{-13} m^2; Loucks, 2003). The Ellenburger experienced multiple episodes of karstification and dolomitization which likely enhanced its effective formation permeability above core measurements (Cox et al., 1998 ; Broadhead, 1999). In our numerical sensitivity study, we assign permeabilities to the Ellenburger ranging from 10^{-14} to 10^{-12} m^2. If bulk permeability is higher than 1000 mD due to the karst- and solution-enhanced porosity, the results presented (using 10^{-12} m^2) here would be an upper bound on calculated excess pressures.

Initial oil and produced water production was low until the early 1990s when the field was redeveloped. Peak production was in 1996 and the field has seen declining production ever since. The Dagger Draw field initially consisted of two fields, Dagger Draw North (DDN) and Dagger Draw South (DDS; Fig. 3b). The fields were originally developed separately and were thought to have independent geologic boundaries. Low permeable Upper Pennsylvanian carbonates in the uppermost part of the Cisco section and the overlying Hueco Fm. provide the top seal for the Upper Pennsylvanian reservoir at Dagger Draw. The Woodford Shale (Devonian) provides the top seal for the Wristen (Silurian) carbonates. Carbonate reservoirs in the Fusselman (Silurian; underlies the Wristen), the Montoya, and the Ellenburger limestones are self-sealed by impermeable

carbonate strata within those units. The Hueco Fm., the Barnett and Woodford Shales with the intervening Lower Mississippian limestone form the top seal for the Ellenburger, Montoya, Fusselman and Wristen carbonate sequence in the Dagger Draw area.

We focus our analysis on 83 reinjection wells within 20 km of the seismicity in Eddy County, New Mexico. Oil and water production data was taken from New Mexico Oil Conservation Division reports (Annual Report of the New Mexico Oil and Gas Engineering Commission Inc., 1969-2003) as well as the GoTech database (2004-2013). Monthly production data of oil, gas and water were summed for all wells in each Township/Range section and then compared to the monthly earthquake frequency (M_d > 2; Fig. 4a). For our modeling effort, the 83 individual oil field brine reinjection wells were lumped into 15 regions (injection nodes) by township and range (Table 2). That is, the 83 injection wells were represented by consolidating them into 15 injection nodes in our model. For some injection nodes, peak re-injection rates of exceeded 1 million barrels per month (Figure 4b). The approximate center of seismic activity coincides with T20S R23E in western Eddy County NM 15 km west of the Dagger Draw oil field (Fig. 3).

Analysis of Seismic and Oil Field Reinjection Data

Edel et al. (2016) analyzed the hypocenter locations of earthquakes in the vicinity of the Dagger Draw oil field between 1962 and 2013. Prior to 1998, the number of New Mexico Tech (Socorro) Seismic network seismic stations was relatively low. Seven to nine

vertical-component short-period seismic stations, began operating in 1998. Edel et al. (2016) relocated earthquakes from 2008-2011 using data from this network as well as the 3-component broadband EarthScope Flexible Array (SIEDCAR) campaign (Fig. 3a). Relocated seismic events cluster in an area of about 10-km diameter with its center located approximately 15 km from the nearest injection wells of the Dagger Draw oil field. The majority of earthquakes occurred at 10 - 12 km depth (Fig. 5) with depth errors between 1.4 - 6 km. Seismic events prior to 2008 were not relocated. Some of the hypocenters appear to line up along a high-angle fault plane. Edel et al. (2016) noted that there is a lag of at least 5 years between peak injection in 1996 and increases in seismicity frequency 15 km to the west of the Dagger Draw oil field in 2001 (Fig. 4a). Edel (2015) hypothesized that a conductive fault zone with a variable dip between 45-80 may provide a conduit for elevated fluid pressures. Given the long lateral distance (15 km) and large depth (11 km) between the earthquake hypocenters and the Dagger Draw oil field injection wells, it seems plausible that a significant lag occurred between the time of peak injection and the time when seismicity increased.

Purpose of Study

The main goal of this study is to assess what reservoir and crystalline basement permeability scenarios could produce a 5-year time lag of fluid pressure increases at a depth of 11 km in the crystalline basement to the west of the Dagger Draw oil field above 0.07 MPa (7 m of excess head). We do not have measured pressure data within the crystalline basement beneath the Dagger Draw oil field to establish the 7 m head

threshold. However, this head value falls within the range of what has been used by prior studies as a triggered seismicity threshold. A secondary goal of this study is to assess different pressure management scenarios that might reduce pressures within the crystalline basement by redistributing and/or lowering the injection rates at various reinjection wells. In the absence of pressure data within the crystalline basement, hydrologic modeling represents a powerful tool to address these questions. However, hydrologic model results are non-unique and can't be validated (Konikow and Bredehoeft, 1992; Oreskes, et al. 1994). There is also uncertainty in representing permeability of the crystalline basement as a bulk parameter as opposed to a discrete fracture network.

Methods

We developed a three-dimensional hydrogeologic model to simulate injection into the Ellenburger Group at Dagger Draw (Fig. 7) and pressure diffusion into the crystalline basement using the United States Geological Survey's groundwater model, MODFLOW (Harbaugh and McDonald, 1996). Bulk crystalline basement permeability is related to the square of the aperture spacing of inter-connected fracture planes (Snow, 1968; Schwartz and Zhang, 2003). Because of the large spatial length scales represented in this study, it was not computationally possible to represent a distributed fracture network (Bogdanov et al., 2003; Neuman, 2005). MODFLOW solves the following groundwater flow equation:

$$\frac{\partial}{\partial x}\left(K_x\frac{\partial h}{\partial x}\right)+\frac{\partial}{\partial y}\left(K_y\frac{\partial h}{\partial y}\right)+\frac{\partial}{\partial z}\left(K_z\frac{\partial h}{\partial z}\right)=S_s\frac{\partial h}{\partial t}+Q(x,y,z,t) \quad (1)$$

where h is the freshwater hydraulic head [L], is the hydraulic conductivity tensor [L t^{-1}], S_s is specific storage [L^{-1}], Q is fluid injection source term [t^{-1}], and t is time [t].

We imposed a constant head boundary (h = 1100m) along the top of the model domain (Fig. 7). This value represents an average land surface elevation for this part of the Permian Basin. We did this so that the effects of injection could be more conspicuous. Additionally, a specified head boundary condition was set along the north, west, south, and west-northeast side boundaries (h = 1100m). If we had imposed head gradient across the model domain's lateral boundaries reflecting topographic variations in the water table, then it would have been more difficult to visualize head changes due to injection as opposed to head changes cause by lateral flow. A no-flux boundary was set along the base of the model and along the southwest boundary, where a relatively large displacement fault was observed in the surface geologic map of Eddy County, NM. The no-flux boundary allows heads to build up higher than they would be if the fault were absent. Overall, these boundary conditions are somewhat idealized. We set the domain far enough away from the injection wells that, with the exception of the no-flux southwest boundary, the simulated head increases were not significantly affected by the constant head boundaries.

The total vertical thickness of the model is 21.1 km. In plan view, the model domain footprint is 200 x 200 km. A uniform lateral grid discretization was used in this study. Preliminary simulations using locally refined (telescoping) grids failed to converge when large permeability contrasts were represented. When a uniform grid was used, no convergence issues were encountered. We used a total of 95 columns, 100 rows, and 24 layers to represent the basin sedimentary rocks (maximum depth 4.4 km) and the underlying crystalline basement. Using a uniform grid allowed us to represent a greater than 5 order of magnitude contrast in hydraulic conductivity between the Ellenberger reservoir (0.86 m/day) and the Barnett Shale (0.000003 m/day). Each finite difference cell had lateral dimensions of about 2.1 by 2.3 km ($\otimes$x by $\otimes$y, respectively). Vertical cell size varies considerably. We lumped the Barnett and Woodford Shales into a single 100 m-thick confining unit that was discretized using 5 layers ($\otimes$z = 20m). We lumped the Ellenburger Montoya, Fusselman and Wristen carbonate units into a single layer. The layer thickness varied from 1 to 247 m with an average thickness of 85m. All injection took place in this layer. A total of 15 layers were used to represent the crystalline basement. The thickness of each crystalline basement layer varied from about 870 m to 1280 m.

An important concern when using numerical models is whether or not the solution domain is sufficiently discretized to accurately capture the hydrodynamics of a given problem. If increasing grid refinement causes significant changes in computed hydraulic heads, then the discretization should be increased. To assess how grid size affected

simulated heads, we varied the lateral discretization by a factor of 3 (see Appendix for details). We found that increasing the lateral discretization of the reservoir from about 2 km on a side (100 x 100 cells) to about 730 m on a side (300 x 300 cells) resulted in a 20% increase in the maximum computed heads in the injection well centers. Near the no-flow boundary, head changes were largely unchanged for the three model runs (see appendix).

Because some of the earthquake hypocenters lined up, more or less, along a sub-vertical planar surface (Fig. 5), we constructed two hydrologic models that included a relatively permeable (10^{-14} to 10^{-15} m^2) vertical fault plane. These two simulations included a north-south trending vertical fault zone of one cell width and 46 km in length (north-south) within the crystalline basement.

The models were run using a time step of one month for 45 years (540 months) between 1969 and 2013 using production data from the reinjection wells within a 20 km radius of the seismic cluster. Monthly oil field brine production from the 416 production wells were reinjected into the Ellenburger group limestone layer using 15 wells for each model simulation. The maximum and average injection rates for each of the 15 well centers are listed in Table 2.

We systematically varied the permeability of the crystalline basement and reservoir in a sensitivity study to determine what range of permeabilities could plausibly lead to head

changes that could trigger seismicity (Table 3). The specific storage was not varied in the sensitivity study between model runs nor was the permeability of the three uppermost units (Table 4). Cross-sectional and plan-view model results are discussed below for 15 scenarios. We monitored head changes at 11 km depth in the center of the region of seismicity and within the Ellenburger Group (red dots in cross-section at the bottom of Fig. 7).

Results

Effects of Crystalline Basement Permeability Variations (Scenarios 1-4)

We begin our analysis by considering how variations in bulk crystalline basement permeability affect the downward propagation of the fluid pore pressure. We varied the bulk permeability of the crystalline basement between 10^{-15} to 10^{-16} m^2. The permeability values we have used in this study are one order of magnitude higher than what are considered typical conditions by Townend and Zoback (2000) for the crystalline basement.

While our model is three-dimensional, we focus our analysis on the head changes within the crystalline basement along an east-west cross-section A-A' (Fig. 7). In all simulations, pore pressure increases are due to oil-field brine injection within the Ellenburger Group (including the Montoya, Fusselman and Wristen carbonates) over the time period between 1969-2013 (Fig. 8). Production in the overlying Pennsylvanian limestone reservoir unit was neglected. In all of these simulations, the Ellenburger permeability is

set at 10^{-12} m^2 and the overlying confining unit (including the Hueco Fm, Woodford and Barnett Shales) was set at $3x10^{-18}$ m^2.

The depth of the pressure envelope propagation (here estimated using the 7 m head contour) into the crystalline basement is strongly controlled by crystalline basement permeability. For all scenarios, pore pressure propagation continues downward after peak injection in 1996 (Figs. 8a-c) and when seismicity began to increase in 2001 (Figs. 8d-f). The 7 m excess head contour extends to a depth of about 4 km below the base of the Ellenburger in 2001 when the crystalline basement permeability is set to 10^{-16} m^2 (Fig. 8d). When the permeability of the crystalline basement was increased to $3x10^{-16}$ m^2 (Fig. 8e), the 7 m excess head contour extends to 10 km below base of the Ellenburger in 2001. When permeability is increased to 10^{-15} m^2, the 7 m excess head contour extends to 12 km below the base of the Ellenburger, extending beyond the centroid of seismicity at the monitoring point located at 11 km depth (Fig. 8f).

Simulated injection pressure within the crystalline basement at the monitoring point at 11 km depth (i.e. the centroid of seismicity) for these three simulations are presented in Figure 9. Using a bulk basement permeability of 10^{-15} m^2 resulted in excess heads reaching about 7 m five years after peak injection. For this scenario, excess heads continued to build up to 30 m by 2013 (16,450 days). Using a bulk crystalline basement permeability of $3x10^{-16}$ m^2 required 17 years beyond the time of peak injection (1996) for excess heads to build up to 7m at the centroid of seismicity. When the crystalline

basement permeability was set at 10^{-16} m^2, the results showed that excess heads of only 1.5 m above hydrostatic conditions by the end of the simulation in 2013.

Computed excess heads within the reservoir at the monitoring point 5 km to the east of the injection wells within the Ellenburger reservoir decline from about 280 m to 260 m as the crystalline basement permeability increases from 10^{-16} to 10^{-15} m^2 (Fig. 10). This is presumably due to increase leakage of fluids into the crystalline basement. For both cases, there is little discernable lag time between peak injection in 1996 and the timing of maximum pressure within the reservoir (Fig. 10). Maximum reservoir heads (not shown, 600 m) were about 100 times higher than head levels within the crystalline basement at a depth of 11 km (Fig. 9). Overall, peak reservoir fluid pressures decreased due to vertical leakage as crystalline basement permeability increased from 10^{-16} to 10^{-15} m^2 in the simulations (Fig. 10).

Effects of Reservoir Permeability Variations (Scenarios 5-7)

We next considered the effects of varying reservoir permeability (Ellenburger Group) while holding the bulk crystalline basement permeability constant (10^{-15} m^2). As noted above, core permeability measurements for the Ellenburger vary between about 10^{-14} to 10^{-13} m^2. A basin-scale effective permeability would likely be higher than 10^{-13} m^2 given the multiple episodes of karstification and diagenesis that this formation experienced. When high reservoir permeability was assigned in our model for the Ellenburger (10^{-12} m^2), there is significant overlap in pressure envelopes between individual injection

centers as well as a maximum head of about 600 m (Fig. 11a, 11d). As reservoir permeability decreased to 10^{-14} m^2, simulated reservoir heads exceeded 2000 m at the injection well centers. This would have exceeded the permitted injection pressures for many of the wells within the Dagger Draw oil field (1520m to 1670m). As the contrast between reservoir and crystalline basement permeability decreases, lateral pressure propagation within the reservoir decreases and the pressure envelope becomes much more spherical in shape (compare Fig. 12a to Fig. 12c). Reduction in reservoir permeability had surprisingly little effect on the magnitude of the pressures within the crystalline basement as well as the timing of the head increase associate with earthquake triggering (Fig. 13).

Effects of Conductive Faults and Permeability Decay with Depth (Scenarios 8-10)

Treating permeability as a constant to a depth of 20 km seems a bit contrived for Precambrian crystalline rocks. As noted above, we assume that crystalline basement permeability can be represented as a bulk continuum property. Although questioned by some (e.g. Ranjram et al. 2015), numerous studies argue that permeability decreases with depth (Manning and Ingebritsen, 1999; Stober and Bucher, 2007; Ingebritsen and Manning, 2010). In two scenarios, we allowed crystalline-basement permeability to decay with depth using the relationship presented by Manning and Ingebritsen (1995) and Ingebritsen and Manning (2010):

$$k = 10^{!!"!!.!!"\#_!"(!)} \qquad (2a)$$

$$k = 10^{!!"!!.!!"\#_!"(!)} \qquad (2b)$$

where k is permeability of the crystalline basement in m^2 and d is depth in km. Equation 2b is considered more applicable to stable continental crust while 2a is considered to be more representative of the crust in tectonically active regions. The Permian Basin in SE New Mexico is considered to be a tectonically stable region. It is unclear whether or not elevated fluid pressures associated with brine re-injection could have a similar effect on seismicity as elevated tectonic stresses.

We also considered the presence of a vertical conductive fault (between 10^{-14} to 10^{-15} m^2) centered in the region of increased seismicity (Fig. 14a, 14b, 14e, 14f). The fault zone was surrounded by a lower-permeability crystalline basement (10^{-16} m^2). As noted above, it is plausible that the clustering of earthquake epicenters along a north-south region may be indicative of a wide conductive fault zone.

The presence of a permeable fault zone surrounded by a lower-permeability crystalline basement matrix (10^{-16} m^2) facilitated the propagation of elevated pore pressures downward along the fault to the base of the model domain. The pressure anomaly extended outwards perpendicular to the fault zone (Fig. 14a, 14b, 14e, 14f). The depth of propagation of the pressure front in the fault zone is sensitive to fault permeability (compare Fig. 14a to 14b). Using a fault permeability of 10^{-14} m^2 allowed the pressure front to propagate downward to a depth of 11 km relatively quickly. For this scenario, excess heads exceeded the 7 m threshold even before peak injection occurred (Fig. 15). Had we used a critical head threshold of 50 m, this scenario would have produced a 5-

year lag between peak injection and seismicity. Using a fault permeability one order of magnitude lower (10^{-15} m^2) resulted in modest head increase of less than 1 m during the simulation period (Fig. 15). We also ran one additional scenario setting the fault permeability equal to $3x10^{-15}$ m^2. This intermediate fault permeability scenario was able to reproduce both the 5-year lag and the 7 MPa pressure increase.

Next, we explored two scenarios of permeability decreasing with depth. In the first scenario, the permeability decayed from $10^{-12.8}$ to $10^{-17.3}$ m^2 (Fig. 14c, 14g). This scenario is consistent with crustal rocks in tectonically active regions (Ingebritsen and Manning, 2010) and we refer to this as the Ingebritsen-Manning (Ing-Man) scenario. In a second scenario, more consistent with a stable continental crust (Manning and Ingebritsen, 1998), the permeability was varied from $10^{-14.8}$ to $10^{-19.3}$ m^2 (Fig. 14d, 14h). We refer to this as the Manning-Ingebritsen scenario (Man-Ing). The Ingebritsen-Manning scenario (dynamic crust) permitted the propagation of pore pressures in excess of 7 m downward to the centroid of seismicity by 2001 (Fig. 14g). This was not the case for the Manning-Ingebristen (stable crust) scenario (Fig. 14h). However, neither the Manning-Ingebritsen (Man-Ing, Fig. 15) nor the Ingebritsen Manning (Ing-Man, Fig. 15) crystalline basement permeability scenarios predicted head increases of 7 m 5 years after peak injection at the centroid of seismicity (Fig. 15). It is likely that some intermediate permeability-depth decay relationship in between those presented in Figure 14 would result in a head change of 7m, 5 years after peak injection at the centroid of seismicity.

Pressure Management Scenarios (Scenarios 11-13)

Oil-field brine reinjection wells are typically repurposed from exploration boreholes or wells from mature oil fields that are no longer productive. Their proximity to active production wells is one of the key factors in deciding which wells are used for reinjection of oil-field brines. Transportation expenses required for trucking or piping produced fluids from an active production well to the reinjection well is one of the main costs of reinjection. As noted above, the volumetric fluid injection rate is clearly an important factor in triggering seismicity (Keranen et al. 2014; Weingarten et al., 2015; Walsh and Zoback, 2015). Within the carbon capture and subsurface storage community, it has been proposed that basin-scale injection of CO_2 will lead to elevated pore pressures (Person et al., 2010) and this could result in induced seismicity (Zoback and Gorelick, 2013). Management strategies have recently been proposed to reduce high pressures in reservoirs where supercritical CO_2 is being injected in order to prevent hydraulic fracturing and vertical (upward) leakage of saline fluids (Buscheck et al. 2012).

Here we consider the potential benefits of redistribution and reduction of injection rates in order to minimize downward fluid propagation and the buildup of fluid pressures within the underlying crystalline basement. In all of these scenarios, the permeability of the crystalline basement was set at 10^{-15} m^2 and the Ellenburger reservoir permeability was set at 10^{-12} m^2. The "base case" (Base), which is used for comparison purposes, is identical to the earlier scenario presented in Figure 11a and 11d (reproduced here in Fig.

16a, 16d). We ran four simulations considering three different injection and redistribution strategies.

In the first two cases, we redistributed the volume of fluid injected at the 15 reinjection wells. The total volume of fluids injected per time step into the Dagger Draw oil field was the same as in all base case. In the first management scenario considered (Fig. 16b, 16e), all of the 15 injection well centers used the same average injection rate ("Ave") per time step. In this scenario, peak injection still occurs in 1996 but the injection rates are evenly distributed across all the wells at any given time step. Relative to the base case, this resulted in injection rates decreasing in some wells and increasing in others. The computed reservoir head distribution does not change dramatically from the base case ("Obs", Fig. 17) but the maximum head changes quite significantly (i.e. contours above 400m are absent in Figs. 16b, 16e). Within the crystalline basement, heads are only reduced by several meters due to this redistribution in injection rates (Fig. 17). Next we weighted the injection rates such that wells closest to the southwestern boundary fault (i.e. the no-flow boundary) received about half as much oil-field brine as wells furthest away (to the northeast). This was done by creating weights for each well's pumping rates and injection rates vary linearly with distance from the southwest boundary. As with the "Ave" scenario, the total amount of fluids injected remained the same as in the base case. The computed excess head increase at the centroid of seismicity are only two meters less than the "Ave" scenario (Wgt, Fig. 16c, 16f; Wgt line, Fig. 17). This was somewhat surprising. Reducing injection rates by 50% and 90% had

the most dramatic decrease in simulated fluid pressure at the crystalline basement monitoring point (lines 50% and 90%, Fig. 17). These results argue that it is not how you inject but how much you inject that plays the most important role in pressure management. These results indicate that managing rates and volumes of injectate are critical to reducing the potential of induced seismicity.

Discussion

How do our estimates of crystalline basement permeability reported here compare to the other modeling studies that have tried to estimate fluid pressures within the crystalline basement? Figure 2 presents crystalline basement hydraulic diffusivity versus depth comparing our results (grey boxes) to those from Hsieh and Bredehoeft (1981) and Keranen et al. (2014). We also included crystalline basement hydraulic diffusivity estimates from studies that investigated triggered seismicity not related to saline water re-injection including Saar and Manga (2003) and Ge et al. (2009). We used hydraulic diffusivity rather than permeability because pressure diffusion rates are controlled by both permeability and rock/fluid compressibility (and hence, specific storage). The hydraulic diffusivities (K/S_s) reported in this study the bulk crystalline basement and for a conductive fault zone are about 1-2 orders of magnitude lower than those reported by prior studies of triggered seismicity associated with brine re-injection. They are in the same range as those reported by Saar and Manga (2003) and Ge et al. (2009). This seems plausible since the centroid of seismicity is 15 km to the west of the Dagger Draw

oil field and is deeper than the triggered seismicity reported at these other sites (Table 1).

Only two scenarios presented above produced elevated pore pressures above 7m five years after peak injection. None of the scenarios presented resulted in a head increase greater than 65 m five years after peak injection in 2001. If we had relaxed the 7m metric for triggered seismicity and assumed an elevated head increase between 1 to 60 m could trigger seismicity, then several additional permeability scenarios would have satisfied the 5-year lag time criteria. Using this approach, we find a range of permeability scenarios that could satisfy our criteria. These included a permeability range between 10^{-15} to 10^{-16} m^2 assuming a homogeneous crust and 10^{-14} to 10^{-15} m^2 for pressure migration downward along a conductive vertical fault. Allowing permeability to decay with depth between $10^{-12.8}$ to 10^{-17} m^2 (Ing-Man, Fig. 15) would also have produced excess heads of about 15 m at 11 km depth, five years after peak injection.

How accurate are the estimates of maximum excess heads reported here? As noted in the methods section, we used a relatively coarse grid ($\otimes x$ =2.1 km, $\otimes y$=2.3km) in this study. Actual wellhead pressures could be 20% higher than what is reported if a more refined grid was used ($\otimes x$ = $\otimes y$ = 0.7km). It has also been known for some time that numerical models systematically under predict wellhead pressures. We can obtain a better estimate of actual well head pressure by using a Peacman correction (Peacman, 1978):

$$\otimes h_{well} = \otimes h_{cell} + \frac{Q}{2\pi T}\ln\left(\frac{0.2\otimes x}{r}\right) \quad (3)$$

where $\otimes h_{well}$ is the estimated drawdown (positive) at the well, $\otimes h_{cell}$ is the computed drawdown (initial - current head; positive) at the cell, r is the distance from the well to the cell and $\otimes x$ is the cell dimension.

If we consider the worst case scenario and assume that the injection well very close to the finite difference node (here we assume 14 cm; the diameter of typical of salt water disposal wells within the Dagger Draw oil field), and using the conditions described in the above base scenario for the Ellenburger group (10^{-12} m^2, Ss = 10^{-6} m^{-1}), and using a maximum pumping rate of 10^6 barrels/month (52,300 m^3/day), this would result in a maximum well head pressure of 98 m above the computed nodal head. Since the maximum head for the base case scenario is about 600m, our the maximum well head pressures for the base case scenario is about 700m which is still below the permitted well head pressures for the Dagger Draw oil field (1520m to 1670m).

This is not the first study to propose that a lag may exist between injection and seismicity – a similar lag between increases in injection and the onset of seismic activity was observed near Jones and Prague, Oklahoma (Walsh and Zoback, 2015). Ge et al. (2009) reported that there was a 2.7 year lag between the filling of the Zipingpu

Reservoir and the Wenchuan earthquake (M_w = 7.9) which occurred at an estimated depth of between 10-20 km. If the Dagger Draw seismicity is in fact induced by the injection of the oilfield wastewater, then it represents the deepest example of triggered earthquakes associated with brine reinjection into basal sedimentary reservoirs to date.

Trying to reduce pore pressure buildup by optimizing reinjection rates, either by injecting at the same volume of fluid at each well or decreasing the injection rates in wells closest to a no-flow boundary, was found to have a second-order effect on simulated fluid pressure increases at the crystalline basement monitoring point. More dramatic pressure maintenance scenarios involving significant reduction (by 50%) of the volume of injected fluids would need to be considered. Reduction in the volumes of reinjected fluids through desalination of oil-field brines represents an attractive management option in the water-scarce Southwestern USA (Balch and Muraleedharan, 2014). Balch and Muraleedharan (2014) pilot desalination study estimated that the cost of disposal of produced oilfield brines dropped from as high as $2.5/barrel to $0.31/barrel.

Conclusions

Hydrologic modeling was used to in this study to test the hypothesis that increased rates of seismicity at 11 km depth within the crystalline basement 15 km west of the Dagger Draw oil field is the result of saline water injection into the basal Ellenburger reservoir. We considered several scenarios including assigning an effective or bulk permeability

value to the crystalline basement, including a conductive fault zone surrounded by tighter crystalline basement rocks, and allowing permeability to decay with depth. We found that the observed lag-time between peak injection in 1996 and the onset of increase seismicity in 2001 can be explained by the time required for the pressure front to migrate through the crystalline basement. We assumed a 7 m head increase as a threshold for induced seismicity. The 5-year lag time helps constrain the permeability of the crystalline basement. If the crystalline basement was assigned a bulk permeability higher than 10^{-15} m^2, then delay between peak injection and seismicity would have been shorter than 5 years. Choosing a bulk permeability less than 10^{-16} m^2 would not permit pressures to build sufficiently to induce seismicity. If a permeable fault-zone is present, it's permeability needs to be about $3x10^{-15}$ m^2. We also tested several different pressure management scenarios varying the injection rates in wells as well as reducing the total volume of fluid injected. Pressure management scenarios that reduced computed excess heads by over 50% within the crystalline basement resulted from reducing the total volume of reinjected fluids by a factor of 2 or more. Redistributing the volume of injected fluid between individual wells did not have a significant impact on fluid pressures within the crystalline basement.

Acknowledgements

This work was supported, in part, by a US Geological Survey Seismic Hazards Program (NEHRP) grant to Jim Evans, Peter Mozley, and Mark Person. Support from the NSF Epscor grant entitled, "Energize New Mexico" to Mark Person, and a Geological Society

of America Laubach Award to Peter Mozley are also acknowledged. The review

comments of Paul Hsieh and an anonymous reviewer are gratefully acknowledged.
Support was also provided by a DOE grant to Evans.

References

Annual Report of the New Mexico Oil and Gas Engineering Commission Inc., 1969-2003, Volume V I-A, southeastern New Mexico.

Balch, R. S., & Muraleedharan, S. (2014, April). Cost-Efficient Well-Head Purification of Produced Water using a Humidification-Dehumidification Process. In *SPE Western North American and Rocky Mountain Joint Meeting*. Society of Petroleum Engineers.

Barnhart W D, Benz H M, Hayes G P, Rubinstein J L, Bergman E, 2014, Seismological and geodetic constraints on the 2011 Mw5. 3 Trinidad, Colorado earthquake and induced deformation in the Raton Basin. *Journal of Geophysical Research: Solid Earth*, *119*(10), 7923-7933.

Barton, C.A., Zoback, M.D. and Moos, D., 1995. Fluid flow along potentially active faults in crystalline rock. *Geology*, *23*(8), pp.683-686.

Bogdanov, I.I., Mourzenko, V.V., Thovert, J.F. and Adler, P.M., 2003. Effective permeability of fractured porous media in steady state flow. *Water Resources Research*, *39*(1).

Brace, W. F., 1965, Some new measurements of linear compressibility of rocks, Journal of Geophysical Research, v. 70, No. 2, pp. 391-398.

Brace W F, 1984, Permeability of crystalline rocks: New in situ measurements. *Journal of Geophysical Research: Solid Earth (1978–2012)*,*89*(B6), 4327-4330.

Broadhead, R. F., 1999, Underdeveloped oil fields – Upper Pennsylvanian and Lower Wolfcampian carbonate reservoirs of southeast New Mexico, Carbonates and Evaporites, v. 14(1), pp. 84-105.

Burbey, T. J., Warner, S.M. Blewitt, G. Bell JW, Hill E. 2006 "Three-dimensional deformation and strain induced by municipal pumping, part 1: Analysis of field data." *Journal of Hydrology* 319, no. 1 (2006): 123-142.

Buscheck, T.A., Sun, Y., Chen, M., Hao, Y., Wolery, T.J., Bourcier, W.L., Court, B., Celia, M.A., Friedmann, S.J. and Aines, R.D., 2012. Active CO 2 reservoir management for carbon storage: Analysis of operational strategies to relieve pressure buildup and improve injectivity. *International Journal of Greenhouse Gas Control*, *6*, pp.230-245.

Caine, J.S. and Tomusiak, S.R., 2003. Brittle structures and their role in controlling porosity and permeability in a complex Precambrian crystalline-rock aquifer system in the Colorado Rocky Mountain Front Range. *Geological Society of America Bulletin*, *115*(11), pp.1410-1424.

Clauser, C. (1992). Permeability of crystalline rocks. Eos, Transactions American Geophysical Union, 73(21), 233-238.

Cooper, H. H., & Jacob, C. E. (1946). A generalized graphical method for evaluating formation constants and summarizing well-field history. *Eos, Transactions American Geophysical Union*, *27*(4), 526-534.

Cox, D. M., Brinton, L., and Tinker, S. W., 1998, Depositional facies and porosity development of an upper Pennsylvanian algal mound reservoir, south Dagger Draw, Eddy County, New Mexico, Cored reservoir examples from Upper Pennsylvanian and Lower Permian carbonate margins, slopes and basinal sandstones, West Texas Geological Society, v. 98-103, variously paginated.

Dewandel, B., Maréchal, J.C., Bour, O., Ladouche, B., Ahmed, S., Chandra, S. and Pauwels, H., 2012. Upscaling and regionalizing hydraulic conductivity and effective porosity at watershed scale in deeply weathered crystalline aquifers. Journal of Hydrology, 416, pp.83-97.

Edel, S., 2015, Characterizing suspected induced seismicity in SE New Mexico in the vicinity of the Waste Isolation Pilot Plant, NM Tech MSc Thesis, 91 p.

Edel, S., Bilek, S, and Broadhead, R. 2016, Earthquake Relocation in SE New Mexico, USA: Possible Induced Seismicity in the Area of the Waste Isolation Pilot Plant (WIPP) Site, Bulletin of the Seismological Society of America (in revision).

Forster C, Smith L (1989) The influence of groundwater flow on thermal regimes in mountainous terrain: A model study. *Journal of Geophysical Research*, **94**, 9439–9451.

Ge, S., M. Liu, N. Lu, J. Godt, G. Luo. 2009 Did the Zipingpu Reservoir Trigger the 2008 Wenchuan Earthquake? Geophysical Research Letters 36.20 doi:10.1029/2009GL040349.

gotech.nmt.edu

Harbaugh, Arlen W., and Michael G. McDonald. *User's documentation for MODFLOW-96, an update to the US Geological Survey modular finite-difference ground-water flow model*. No. 96-485. US Geological Survey; Branch of Information Services [distributor],, 1996.

Holtz, M. H., and Kerans, C., 1992, Characterization and categorization of west Texas Ellenburger reservoirs, in M. P. Candelaria and C. L. Reed, eds., Paleokarst, karst-related diagenesis, and reservoir development: Examples from Ordovician-Devonian age strata of west Texas and the mid-continent: Permian Basin Section SEPM, Field Trip Cuidebook, v. 92-33, pp. 45-54.

Horton, S., 2012, Disposal of hydrofracking waste fluid by injection into subsurface aquifers triggers earthquake swarm in central Arkansas with potential for damaging earthquake, Seismological Research Letters, v. 83(2), pp. 250-260.

Hsieh, P. A., and Bredehoeft, J. D., 1981, A reservoir analysis of the Denver earthquakes: A case of induced seismicity, Journal of Geophysical Research, v. 86(B2), 903 pp.

Ingebritsen, S. E., and Gleeson, T., 2015, Crustal Permeability: Introduction to the special issue, Geofluids, v15, pp. 1-10.

Ingebritsen, S. E., and Manning, C. E., 2010, Permeability of the continental crust: Dynamic variations inferred from seismicity and metamorphism. Geofluids, v. 10, pp. 193-205.

Kaven, J.O., Hickman, S.H., McGarr, A.F. and Ellsworth, W.L., 2015. Surface Monitoring of Microseismicity at the Decatur, Illinois, CO2 Sequestration Demonstration Site. *Seismological Research Letters*.

Kim, W., 2012, December. Induced Seismicity Associated with Waste Fluid Injection into Deep Wells in Youngstown, Ohio. In *AGU Fall Meeting Abstracts* (Vol. 1, p. 2496).

Keranen, K. M., Savage, H. M., Abers, G. A., and Cochran, E. S., 2013, Potentially induced earthquakes in Oklahoma, USA: Links between wastewater injection and the 2011 M_w 5.7 earthquake sequence, Geology, v. 41(6), pp. 699-702.

Keranen, K. M., Weingarten, M., Abers, G. A., Bekins, B. A., and Ge, S., 2014, Induced earthquakes. Sharp increase in central Oklahoma seismicity since 2008 induced by massive wastewater injection, Science, v. 345(6195), pp. 448-451.

Klimczak, C., Schultz, R. A., Parashar, R., & Reeves, D. M. (2010). Cubic law with aperture-length correlation: implications for network scale fluid flow. *Hydrogeology Journal*, *18*(4), 851-862.

Konikow, L.F. and Bredehoeft, J.D., 1992. Ground-water models cannot be validated. *Advances in water resources*, *15*(1), pp.75-83.

Loucks, R. G. "Review of the Lower Ordovician Ellenburger Group of the Permian Basin." *West Texas: Bureau of Economic Geology* (2003).

Lowell R, Van Cappellen P, Germanovich LN (1993) Silica precipitation in fractures and the evolution of permeability in hydrothermal upflow zones. Science, 260, 192–194.

Lumley, D. (2010). 4D seismic monitoring of CO_2 sequestration. *The Leading Edge*, *29*(2), 150-155.

Mailloux, B.J., Person, M., Kelley, S., Dunbar, N., Cather, S., Strayer, L. and Hudleston, P. (1999). Tectonic controls on the hydrogeology of the Rio Grande Rift, New Mexico. Water Resources Research 35. doi: 10.1029/1999WR900110. issn: 0043-1397.

Manga M, Beresnev I, Brodsky EE, Elsworth D, Ingebritsen SE, Mays DC, Wang CY (2012) Changes in permeability caused by transient stresses: Field observations, experiments, and mechanisms, *Reviews of Geophysics*, **50(2)**, 10.1029/2011RG000382

Manning, A. H., and Caine, J.S. (2007), Groundwater noble gas, age, and temperature signatures in an Alpine watershed: Valuable tools in conceptual model development, Water Resour. Res., 43, W04404, doi:10.1029/2006WR005349.

Manning, C. E., and Ingebritsen, S. E., 1999, Permeability of the continental crust: constraints from heat flow models and metamorphic systems. Reviews in Geophysics, v. 37, p. 127-150.

Neuman, S.P., 2005. Trends, prospects and challenges in quantifying flow and transport through fractured rocks. *Hydrogeology Journal*, *13*(1), pp.124-147.

New Mexico Oil Conservation Division, 2016, http://ocdimage.emnrd.state.nm.us/imaging/AEOrderCriteria.aspx

Oreskes, N., Shrader-Frechette, K. and Belitz, K., 1994. Verification, validation, and confirmation of numerical models in the earth sciences. *Science*, *263*(5147), pp.641-646.

Peacman, 1978, Interpretation of Well-Block Pressures in Numerical Reservoir Simulation. SPE Journal, v. 18(3), p. 183-19.

Pepin, J., Person, M., Phillips, F., Kelley, S., Timmons, S., Owens, L., Witcher, J., and Gable, C., 2015, Deep fluid circulation within crystalline basement rocks and the role of hydrologic windows in the formation of the Truth or Consequences, New Mexico low-temperature geothermal system, Geofluids, v15, pp. 139-160.

Person, M. Banerjee, A., Rupp, J., Medina, C. Lichtner, P., Gable, C., Pawar, R. Celia, M., McIntosh, J., and V. Bense, 2010, Assessment of Basin-Scale Hydrologic Impacts of CO_2 Sequestration, Illinois Basin, International Greenhouse Gas Journal, doi:10.1016/j.ijggc.2010.04.004.

Ranjram, M., Gleeson, T., & Luijendijk, E. (2015). Is the permeability of crystalline rock in the shallow crust related to depth, lithology or tectonic setting?. *Geofluids*, *15*(1-2), 106-119.

Saar, M. O., and Manga, M. 2003 Seismicity Induced by Seasonal Groundwater Recharge at Mt. Hood, Oregon. Earth and Planetary Science Letters 214, p. 605-18.

Schwartz, F.W. and Zhang, H., 2003. Fundamentals of Groundwater John Wiley & Sons. New York, 583.

Snow, D. T. (1968). Rock fracture spacings, openings, and porosities.Journal of Soil Mechanics & Foundations Div.

Stober, I. and Bucher, K., 2007, Hydraulic properties of the crystalline basement, Hydrogeology Journal, 15: 213-224.

Townend, J. and Zoback, M.D., 2000. How faulting keeps the crust strong. *Geology*, *28*(5), pp.399-402.

Vasco, D. W., Ferretti, A., & Novali, F. (2008). Reservoir monitoring and characterization using satellite geodetic data: Interferometric synthetic aperture radar observations from the Krechba field, Algeria. *Geophysics*,*73*(6), WA113-WA122.

Verdon, J. P., Kendall, J. M., Stork, A. L., Chadwick, R. A., White, D. J., & Bissell, R. C. (2013). Comparison of geomechanical deformation induced by megatonne-scale CO2 storage at Sleipner, Weyburn, and In Salah. *Proceedings of the National Academy of Sciences*, *110*(30), E2762-E2771.

Walsh, F. R., & Zoback, M. D. (2015). Oklahoma's recent earthquakes and saltwater disposal. *Science advances*, *1*(5), e1500195.

Weingarten, M., Ge, S., Godt, J. W., Bekins, B. A., Rubinstein, J. L., 2015, High-rate injection is associated with the increase in U.S. mid-continent seismicity, Science, v. 348, no. 6241, pp. 1336-1340.

Wright, W.F., 1979, Petroleum geology of the Permian Basin: West Texas Geological Society, Publication 79-71, 98 p.

Zhang, Y., Person, M., Rupp, J., Ellett. K., Celia, M. A., Gable, C. W., Bowen, B., Evans, J., Bandilla, K., Mozley, P., Dewers, T., Elliot, T., 2013, Hydrogeologic Controls on Induced Seismicity in Crystalline Basement Rocks Due to Fluid Injection into Basal Reservoirs, Ground Water, v. 51, pp. 525-538.

Zoback, M.D. and Gorelick, S.M., 2012. Earthquake triggering and large-scale geologic storage of carbon dioxide. *Proceedings of the National Academy of Sciences*, *109*(26), pp.10164-10168.

Zoback, M.D. and Gorelick, S.M., 2015. To prevent earthquake triggering, pressure changes due to CO_2 injection need to be limited. *Proceedings of the National Academy of Sciences*, *112*(33), pp.E4510-E4510.

Appendix

Effects of Model Discretization on Simulated Head Increases and Estimates of Well Head Pressures

The Dagger Draw model domain presented in this manuscript had large lateral length scales (about 200 km by 200 km). Given the number of vertical layers required to represent pressure diffusion in the crystalline basement (15, average $\otimes z \sim 1105$ m), this required us to use a relatively coarse lateral discretization (95 x 100; $\otimes x \sim 2100$m; $\otimes y \sim 2300$m). Preliminary model runs that used grid refinement (i.e. a telescoping mesh) near the pumping wells failed to converge when a large (10^5) permeability contrast was used.

Here, we present a sensitivity study to assess how simulated head increases and patterns within the Ellenberger due to fluid injection are influenced by grid size. We used the same model domain geometry, number of injection wells, and lateral boundary conditions for this exercise as was used in the paper. We fixed the reservoir thickness at a constant value of 85 m. The reservoir hydraulic conductivity (K) was set at 0.86 m/day (10^{-12} m^2). We also used a constant injection rate for each well (2000 m^3/day). A specific storage (S_s) coefficient of 10^{-6} m^{-1} was used. A time step size of 0.3416 days was used in the simulations presented. These parameters are typical of many of the simulations presented in the paper.

Simulated hydraulic heads for three different discretization levels are presented in Figure A1. The coarsest discretization is similar to what we used in our paper. For

the finest level of discretization, the maximum computed heads are about 20% of higher when compared to the coarsest grid. After 1 month, the maximum simulated head within the Ellenberger reservoir oil field increased from 19.3 m to 23.7 m (18%) between the coarse (100x100) and most refined (300x300) discretization (Table 1; Fig. A1a-A1c). After 1 year, the maximum head increased from 60.6 m to 64.7 m (6%; Table A1; Fig. A1d-A1f). There was little change in simulated heads adjacent to the no flow boundary between the coarsest and finest discretization runs (18.7 m to 17.89 m, Table A1; see dark square in Figure A1 for location of the monitoring point). The patterns of head increases are nearly identical.

Computational limitations prevented us from also exploring the effects of changes in vertical discretization on simulated heads within the crystalline basement. However, the average vertical discretization within the crystalline basement (MODFLOW layers 10-24) was 1105 m. This roughly corresponds to the 200 x 200 lateral discretization scenario. We conclude that the discretization used in our model likely under predicts the maximum heads by at least 20% near the injection wells but has little effect on simulated heads at distances greater than 10 km.

Table A1. *Summary of Model Discretization Sensitivity Study*

Number of Nodes in x-, y-direction	Average lateral (⊗x, ⊗y) Cell Size (m)	Maximum Simulated Head (m) after 1 month	Maximum Simulated Head (m) after 1 year	Head Increase (m) at No Flow Boundary After 1 year
100	2204	19.3	60.6	18.7
200	1102	21.8	62.7	18
300	735	23.7	64.7	17.98

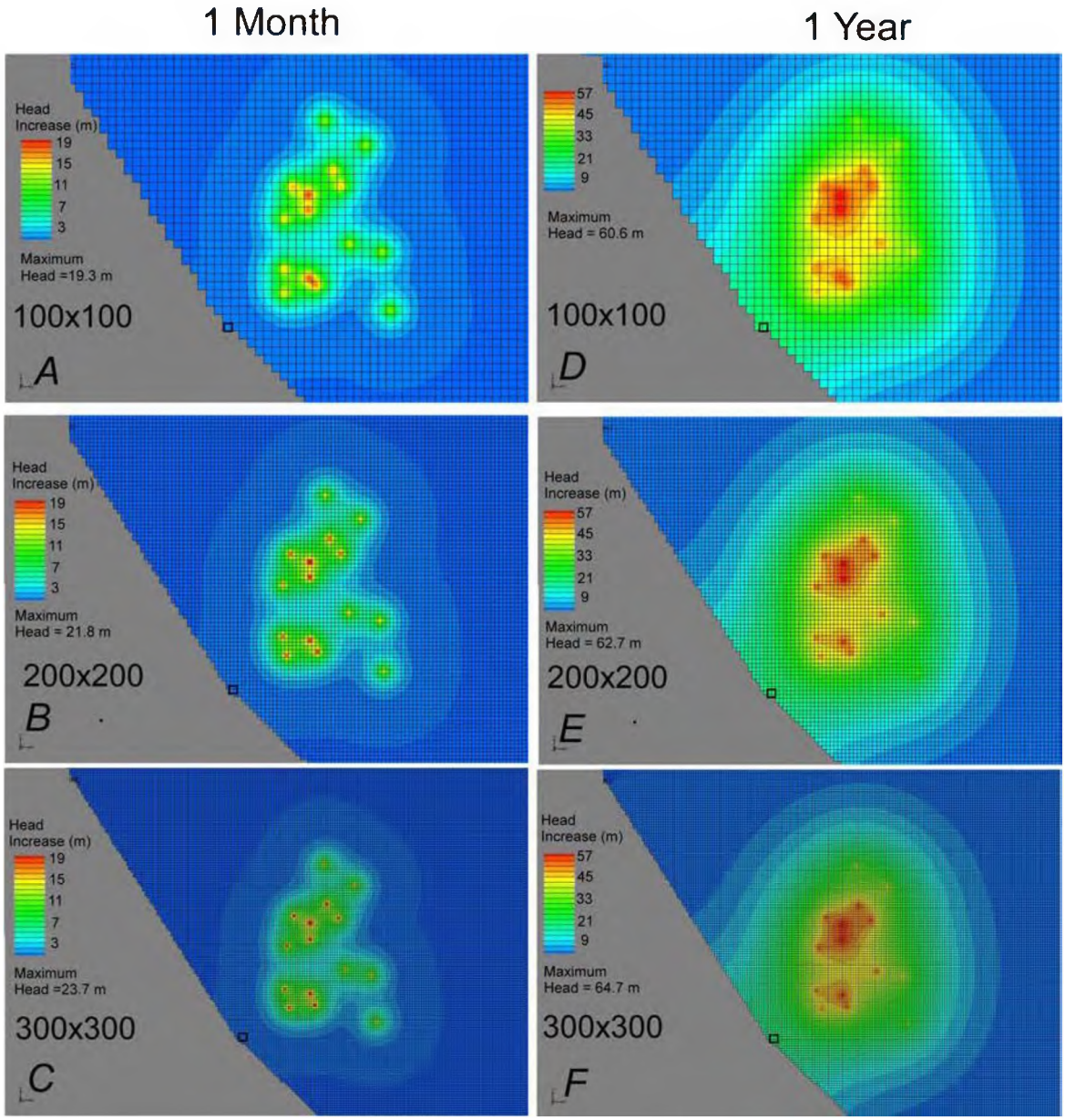

Figure A1. *Simulated head increases in Ellenburger reservoir after 1 month (A-C) and 1 year (D-F) using three different grid resolutions (100 x 100, 200 x 200, 300 x 300). A constant injection rate of 2000 m^3 day^{-1} was assigned to each well. The permeability and specific storage coefficient assigned to the Ellenuburger reservoir was 10^{-12} m^2 and 10^{-6} m^{-1}, respectively. Hydraulic boundary conditions are the same as what was used in this study elsewhere. Maximum heads and heads near the fault zone (see square) are reported in Table S1.*

Table 1. *Injection, seismicity, and fluid pressure data from case studies documenting Instances of induced seismicity across the USA.*

Location	Basal Reservoir Name	Max. Earthquake Magnitude / Average Hypocenter Depth (km)	[+]Maximum Cumulative Injection Rate (Millions Barrels /month)	Well Head Fluid Pressure Increase (MPa)	Maximum Lateral Distance Between Injection Wells and Seismicity (km)
[1]Youngstown, OH	Crystalline Basement	3.9 / 3.7	0.15*	7	1
[2,5]Jones OK	Arbuckle Limestone	3 / 4.5	18	1	35
[3]Guy AK	Ozark	4.7 / 5	1.8	11.8	15
[4,5]Prague, OK	Arbuckle Limestone	5.7 / 5	0.6	3.7	15
Dagger Draw, NM	Ellenberger Limestone	3.2/11	3	-	15
Rocky Mountain Arsenal	Crystalline Basement	5.5/5	0.19	7.2	5

[1]Kim (2013), single injection well production reported, North Star-1; [2]Keranen et al. (2014); [3]Horton (2012); [4]Keranen et al. (2013); [5]Walsh and Zoback (2015)

[+]Cumulative injection refers here to the summation of injection rates of all wells within a given area of study (spatial summation). That said, we note that the Youngstown, Ohio study of Kim (2013) only presented injection data for 1 well.

Table 2. *Locations, re-injection rates, and lateral distance to the center of seismicity for each of the 15 injection well centers. The township (T) and range (R) of each injection center is indicated by the ID.*

Section ID	Easting (m)	Northing (m)	Maximum (Barrels/ month)	Average (Barrels/ month)	Distance (km)
T22S R26E	567254	3581357	2.0E+05	4.57E+04	44
T22S R24E	548426	3586558	1.0E+07	3.17E+06	25
T2S 2R23E	540024	3585734	5.0E+05	1.32E+05	20
T21R26	566023	3596084	8.0E+04	1.88E+04	38
T21R25	557571	3597820	2.0E+06	4.05E+05	29
T21R24	546987	3590619	1.0E+07	2.81E+06	22
T20R25	546535	3607245	3.0E+06	7.85E+05	18
T20R24	539417	3605254	3.0E+06	6.30E+05	11
T19R26	555433	3613893	1.0E+06	2.62E+05	29
T19R25	546645	3612400	1.0E+06	2.51E+05	20
T19R24	541546	3614440	3.0E+05	6.43E+04	17
T18R26	560699	3624065	2.0E+05	3.91E+04	38
T18R25	552183	3618446	2.0E+05	3.46E+04	28
T17R25	551112	3630933	3.0E+04	6.32E+03	36
T21R23	538540	3591748	7.0E+05	9.64E+04	15

Table 3. *Permeability (in m^2) using in different hydrologic model runs (scenarios) for select units.*

Scenario	Ellenburger Limestone	Crystalline Basement	Fault Zone	Figures
1	10^{-12}	10^{-16}	-	8a,8d, 9, 10
2	10^{-12}	$3x10^{-16}$	-	8b,8e, 9, 10
3	10^{-12}	10^{-15}	-	8c, 8f, 9, 10, 11a, 11d, 12a, 12d, 13, 16a, 16d, 17
4	10^{-13}	10^{-15}	-	11b, 11e, 12b, 12e,13
5	10^{-14}	10^{-15}	-	11c, 11f, 12c, 12f, 13
6	10^{-12}	10^{-14}	10^{-12}	14a, 14e, 15
7	10^{-12}	10^{-15}	10^{-12}	14b, 14f, 15
10	10^{-12}	$10^{-12.8}$- 10^{-17}	-	14c, 14g, 15
11	10^{-12}	$10^{-14.8}$- 10^{-19}	-	14d, 14h, 15
12-15	10^{-12}	10^{-15}	-	16, 17

Table 4. *Hydrogeologic properties for hydrostratigraphic units not varied between model runs.*

Formation Name	k (m^2)	S_s(m^{-1})
Upper Permian (Layer 1)	$3x10^{-15}$	10^{-6}
Upper Pennsylvanian (Layer 2)	10^{-12}	10^{-6}
Barnet Shale (Layers 3-8)	$3x10^{-18}$	10^{-5}
Ellenburger Reservoir (Layer 9)		10^{-6}
Crystalline Basement (Layers 10-24)		10^{-7}

Figure 1. *Generalized geologic cross sections showing locations of oil-field brine reinjection wells and associated seismicity within the crystalline basement in New Mexico (A, Edel et al., 2016), Arkansas (B; Horton, 2012); Ohio (C; Kim, 2013) ; and Oklahoma (D, Kerenan et al., 2013).*

Figure 2. *Hydraulic diffusivities derived from model reconstructions of triggered seismisity studies and inferred from geophysical, petrological, and geophysical data (black & blue lines). The red Permeability-depth curve is from Manning and Ingebritsen (1999). The blue permeability decay curve is from Ingebritsen and Manning (2010). The permeability axis assumes a specific storage coefficient of* 10^{-6} m^{-1}*. The grey boxes are hydraulic diffusivities reported in this study for the Dagger Draw oil field in southeastern New Mexico.*

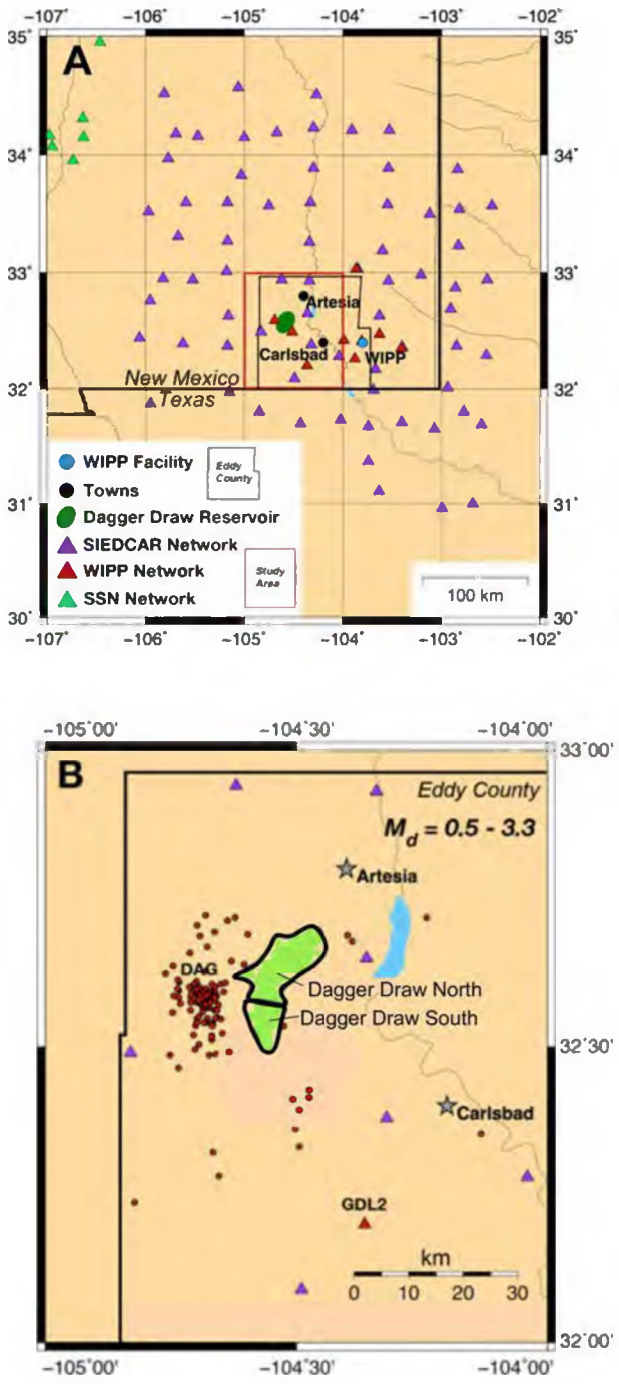

Figure 3. *(A) Study area map showing WIPP seismic (red triangles), SIEDCAR (purple triangles), Socorro Seismic network (SSN, green triangles) location of the WIPP site and Dagger Draw (dark green blob) oil field in Eddy County, New Mexico. The location of the WIPP site is indicated by the blue circle. (B)* Relocated epicenters (small red circles) for 203 earthquakes between 2008/09-2010/07 *relative to the location of the Dagger Draw oil field. Oil field locations (green shaded areas) are courtesy of the New Mexico Bureau of Geology, reservoir outline from Speer (1993).*

Figure 4. *(A) Annual production of oil and saline brines (water) from the Dagger Draw Oil Field, Permian Basin and seismic events greater than M2. (B) Average and maximum injection rates for the 15 injection well centers versus distance from the centers to the centroid of seismicity (after Edel et al., 2016).*

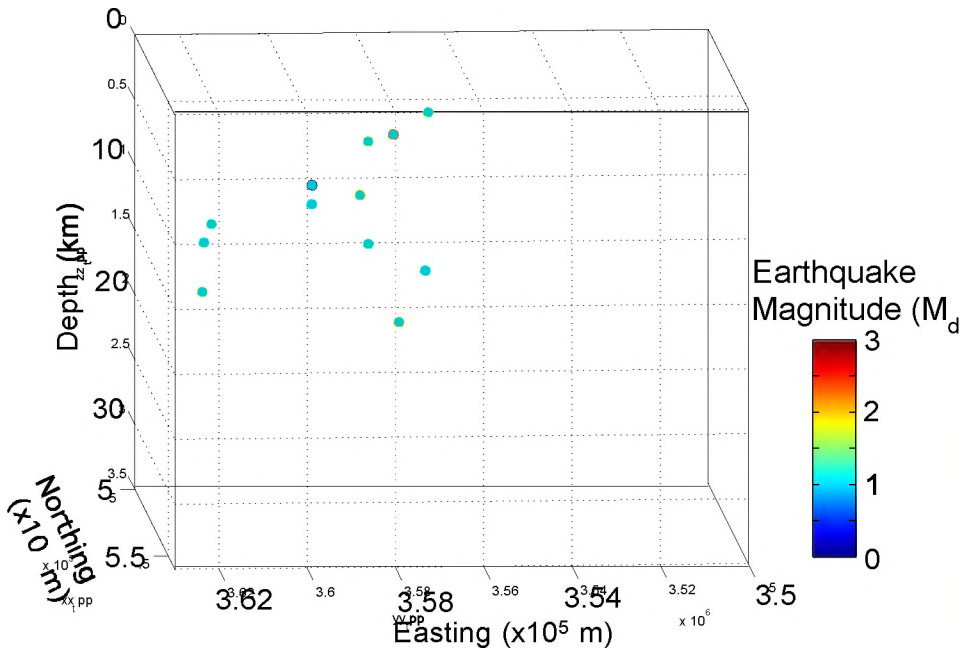

Figure 5. *Three-dimensional view (looking north) showing relocated hypocenter depths for seismicity* from 2008/09–2010/07 *adjacent to the Dagger Draw Oil Field, Permian Basin, New Mexico. Sphere size indicates magnitude (up to M_d 3.2). Depth errors range between 1.4 - 6 km. Hypocenter data from Edel et al. (2016). Black surface indicates position of fault plane used in hydrogeologic model.*

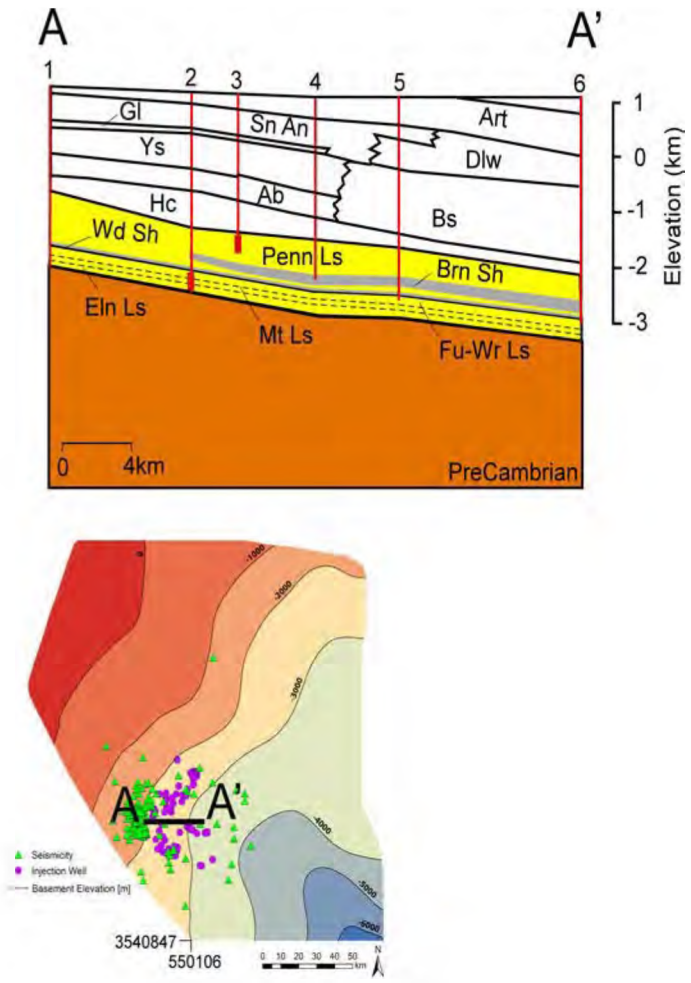

Figure 6. *Contour map of crystalline basement elevation (in m, sea level datum) surrounding the Dagger Draw oil field in southeastern, NM. The locations of the 83 oil-field brine reinjection wells (purple circles) and seismicity (green triangles) is shown on the contour map. A geologic cross-section across the Dagger Draw oil filed is also shown. Oil production occurs primarily within Pennsylvanian carbonates (Penn Ls, yellow). Oil-field-brine reinjection occurs in the basal Ellenberger Group (El), Montoya Limestone (Mt), and Fusselman and Wristen limestone units (Fu-Ws, yellow). Additional geologic units include: Brn Sh, Barnett Shale (gray); Wd Sh, Woodford Shale (gray); Hc Hueco Formation; Ab Abo formation; Ys, Yeso Formation; Gl, Glorietta Sandstone; Sn An, San Adres formation; Art, Artesia Group. Red numbered lines show well control; 1- Southern Union Production Corp. No. 1 Elliot, 24-18S-23E; 2- Yates Petroleum No. 3 Roy AET WD, 7-19S-25E; 3- Yates Drig. No. 1 Rodke AOY 21-19S-25E; 4- Northern Natural Gas, No. 1 Moutray, 6-20S-26E; 5- S. P. Yates No. 4, Pecos River Deep Unit, 11-20S-26E; 6 Oxy USA No. 1 Govt NBFD 11-20S-26E. Plan view map shows approximate location of cross section, production wells (red squares) and seismicity (green triangles). Injection interval illustrated schematically using red rectangle at the bottom of two wells.*

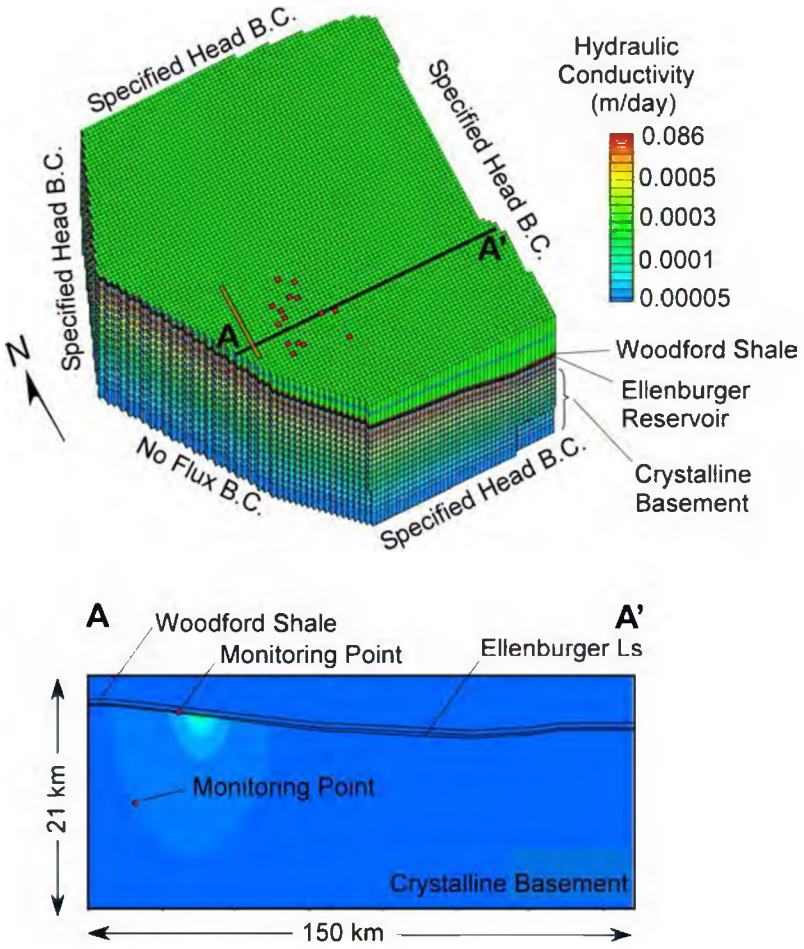

Figure 7. *Three dimensional view of Modflow finite difference grid and East-West cross section A-A' showing locations of two monitoring points used in sensitivity study. The red squares the lateral position of the reinjection wells within the Ellenburger Limestone (layer 9) projected up onto the top layer. The thin orange line denotes the lateral position of a relatively high permeability fault zone within the crystalline basement projected up onto the top layer (layers 10-25).*

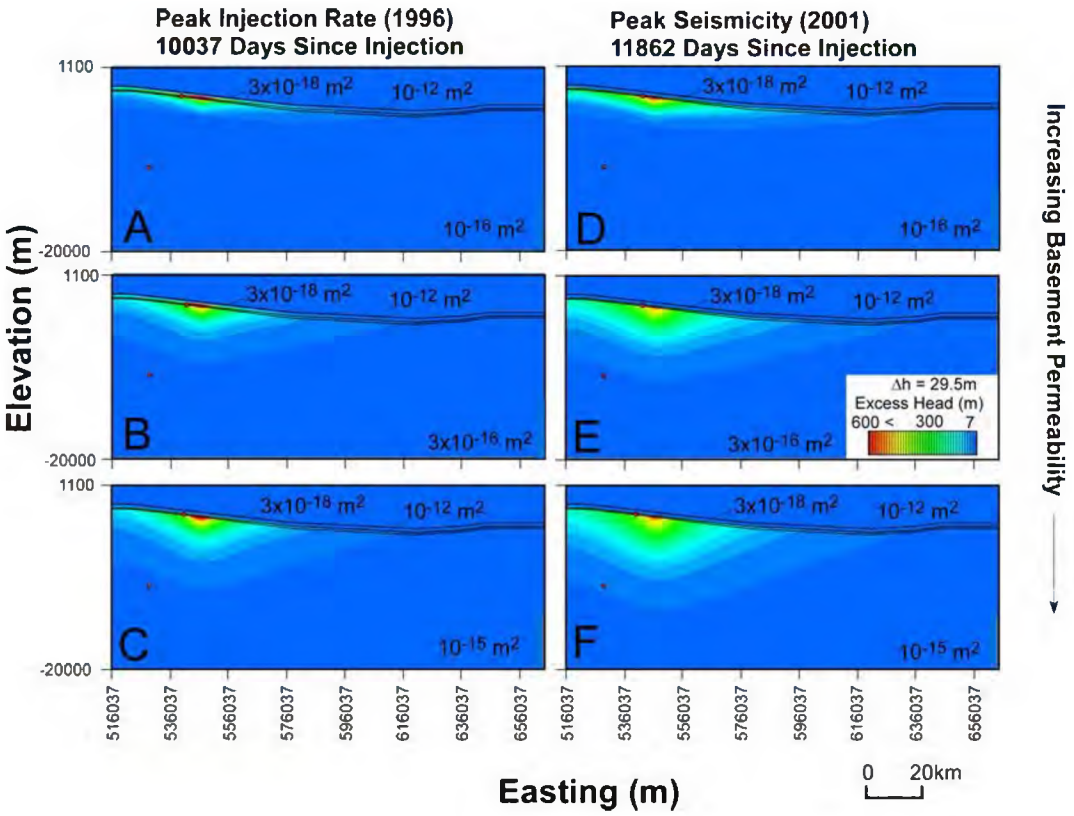

Figure 8. *Sensitivity study showing effect of changes in crystalline basement permeability on simulated excess heads during peak injection (1996.5, left column) and the onset of seismicity (2001, right column). The reservoir permeability in all of these simulations was set at 10^{-12} m^2 (1000 mD). Vertical exaggeration is 3. The first head contour is 7 m. Subsequent contour intervals are 29.5 m (i.e. 7 m, 36.5 m, 66 m, 95.5 m, 125 m, …, etc.). Within the region of injection, the top of the Ellenburger reservoir has a depth range between about 1900 m to 2700m below land surface.*

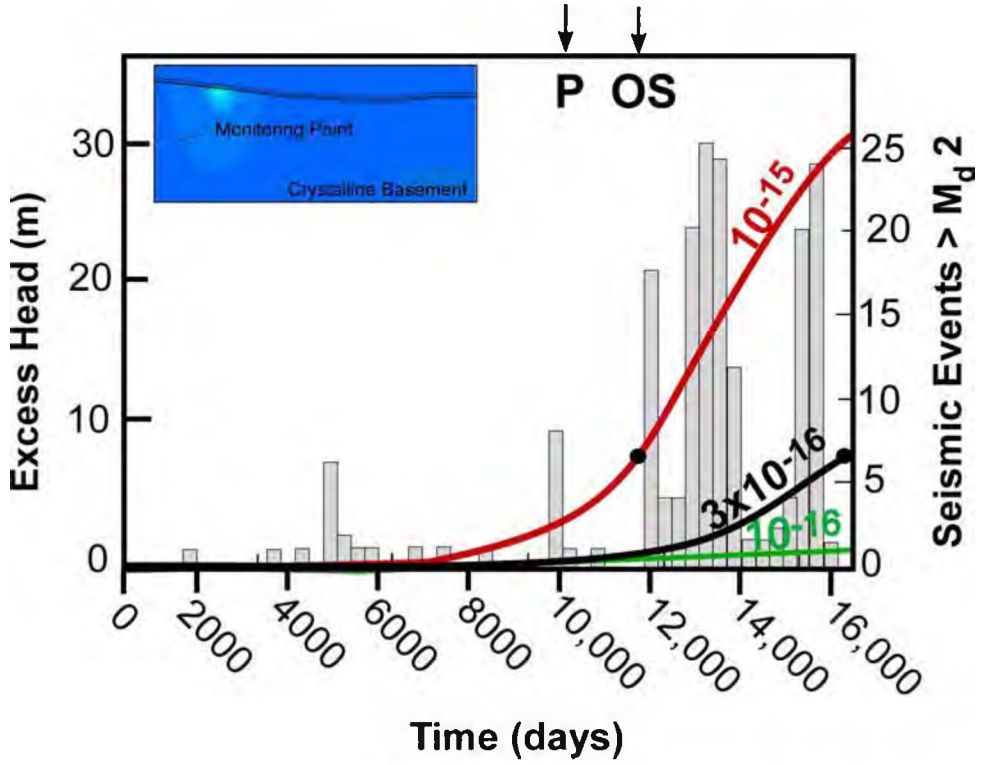

Figure 9. *Changes in excess head through time for three different crystalline basement permeability scenarios (10^{-15} m^2, $3x10^{-16}$ and 10^{-16} m^2) monitored at the center of seismicity within the crystalline basement (11 km depth) point shown in inset. Lines show simulated excess heads for the different basement permeability scenarios from Figure 8. The bar graph presents the number of earthquakes each year from 1960 to greater than M_d >2. The origin of the time axis is January 1, 1969. The origin of the time axis is January 1, 1969. Peak injection (P) occurred after 10037 days (1996.5). The onset of increased seismic frequency (OS) began in 2001.*

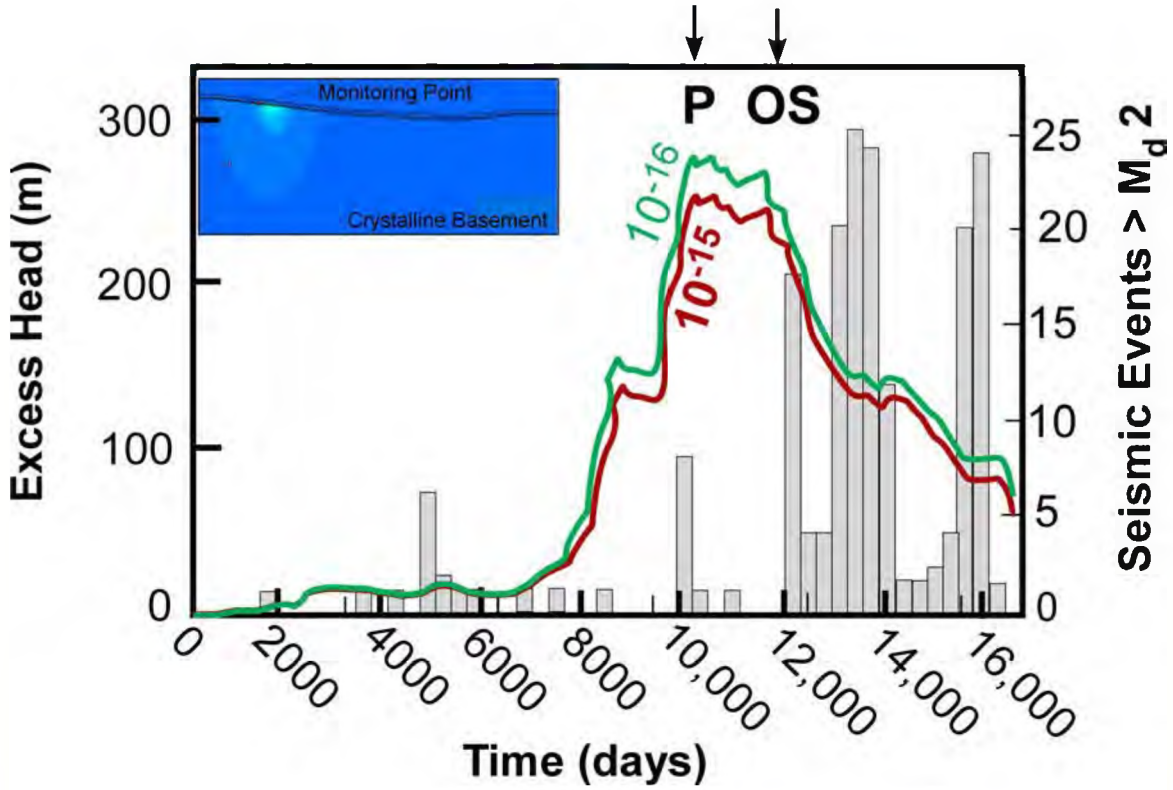

Figure 10. *Changes in excess head through time for two different crystalline basement permeability scenarios (10^{-15} m^2 and 10^{-16} m^2) within the Ellenburger reservoir monitoring point shown in the inset. In both simulations, the reservoir permeability was set at 10^{-12} m^2. Lines show simulated excess heads for different basement permeability. The bar graph presents the number of earthquakes each year from 1960 to greater than M_d >2. The origin of the time axis is January 1, 1969. Peak injection (P) occurred after 10037 days (1996.5). The onset of increased seismic frequency (OS) began in 2001.*

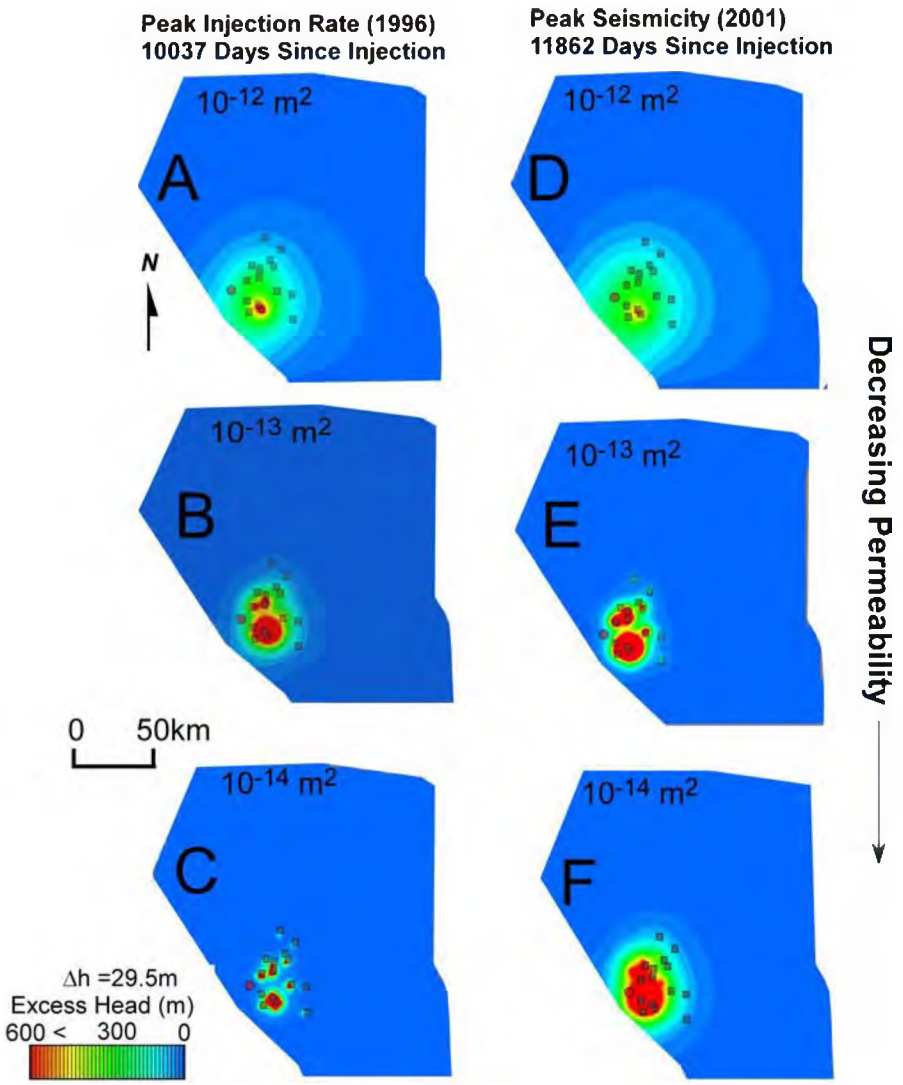

Figure 11. *Plan view map showing effects of changes in reservoir permeability on simulated excess heads during peak injection (1996.5, left column) and peak seismicity (2001, right column). The crystalline basement permeability in all of these simulations was set at 10^{-15} m^2 (1 mD). The yellow squares denote the injection well locations. The red circle denotes the center of seismicity. Subsequent contour intervals are 29.5 m (i.e. 7 m, 36.5 m, 66 m, 95.5 m, 125 m, …).*

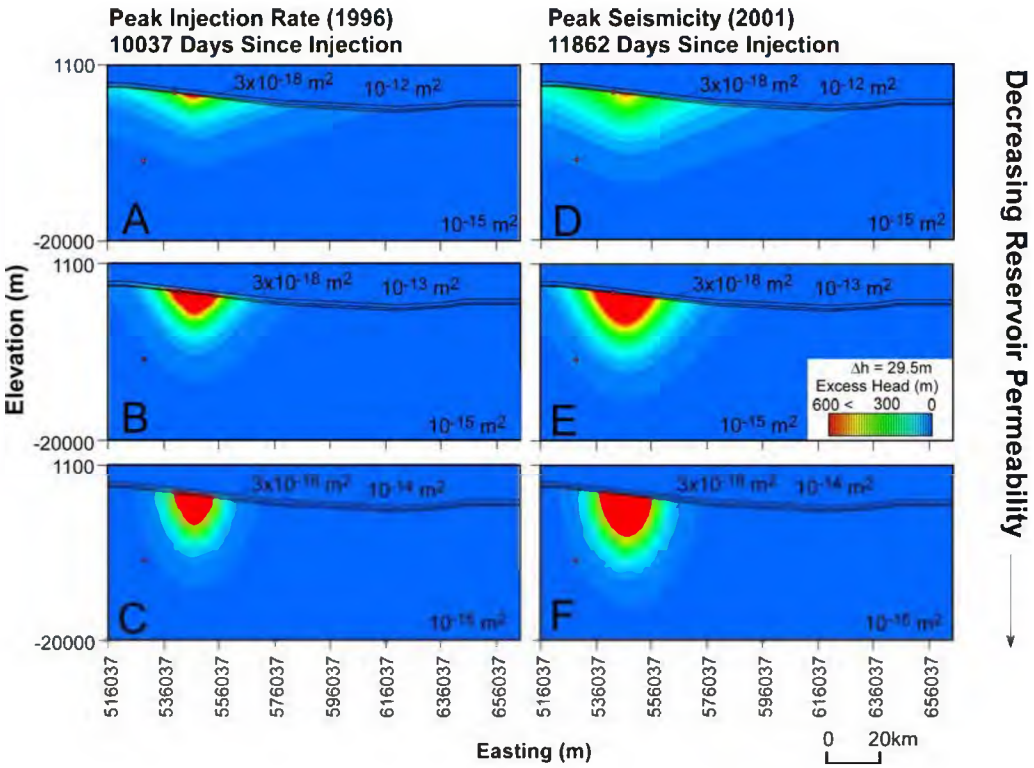

Figure 12. *Sensitivity study showing effect of changes in reservoir basement permeability on computed excess heads during peak injection (1996.5, left column) and peak seismicity (2001, right column). The reservoir permeability in all of these simulations was set at 10^{-12} m^2 (1000 mD). Vertical exaggeration is 3. Subsequent contour intervals are 29.5 m (i.e. 7 m, 36.5 m, 66 m, 95.5 m, 125 m, …). Within the region of injection, the top of the Ellenburger reservoir has a depth range between about 1900 m to 2700m below land surface.*

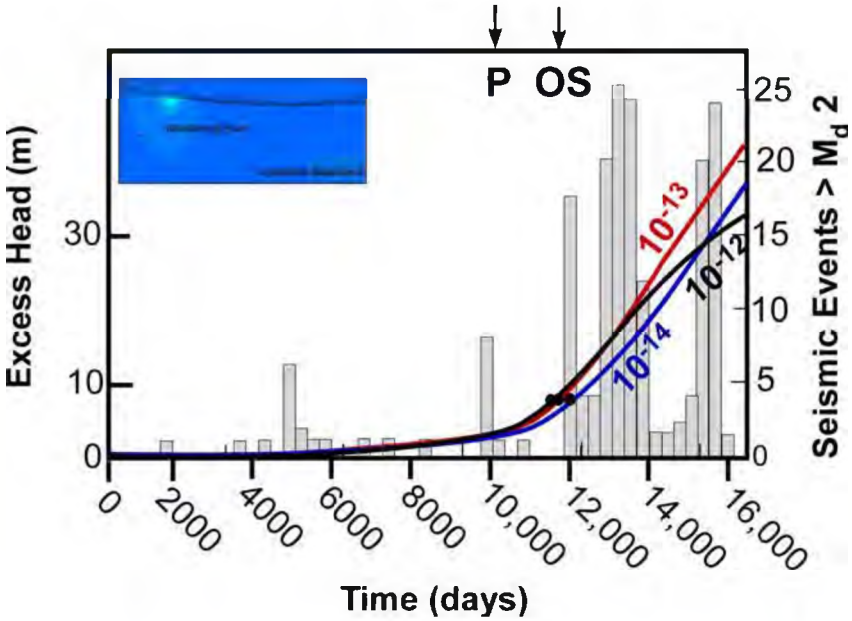

Figure 13. *Effects of changes in reservoir permeability on changes in excess head through time at crystalline basement monitoring point shown in inset. Lines show simulated excess heads for different basement permeability. The bar graph presents the number of earthquakes each year from 1960 to greater than M_d >2. The origin of the time axis is January 1, 1969. Peak injection (P) occurred after 10037 days (1996.5). The onset of increased seismic frequency (OS) began in 2001.*

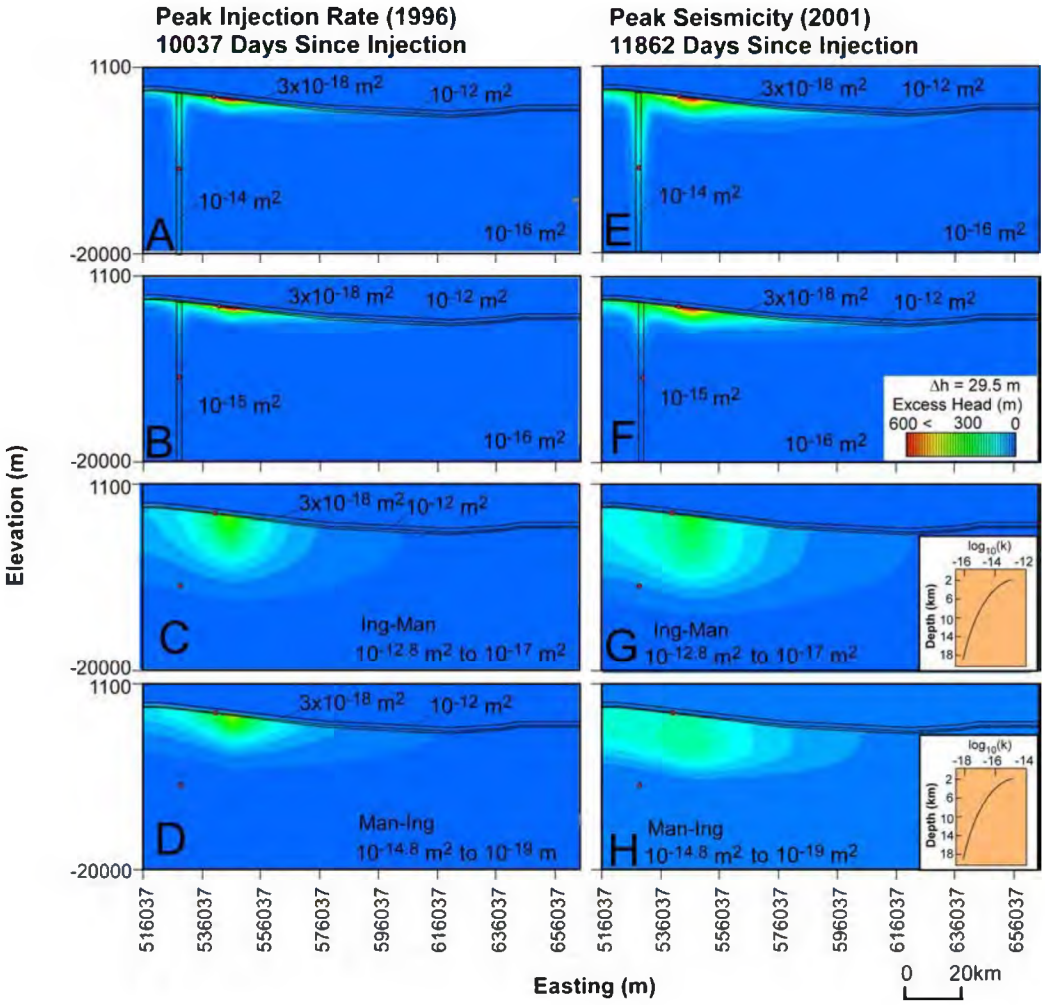

Figure 14. *Sensitivity study showing effect of changes in crystalline basement permeability on computed excess heads during peak injection (left column) and peak seismicity (right column). The reservoir permeability in all of these simulations was set at 10^{-12} m^2 (1000 mD). The following scenarios are considered here: high permeability crystalline basement fault Figures A & D; A weathered zone at the top of the and a high permeability crystalline basement fault beneath the weathered zone, Figures B & E; and Ingebritsen and Manning (2010) permeability decay with depth imposed within the crystalline basement. Vertical exaggeration is 3. Subsequent contour intervals are 29.5 m (i.e. 7 m, 36.5 m, 66 m, 95.5 m, 125 m, …).*

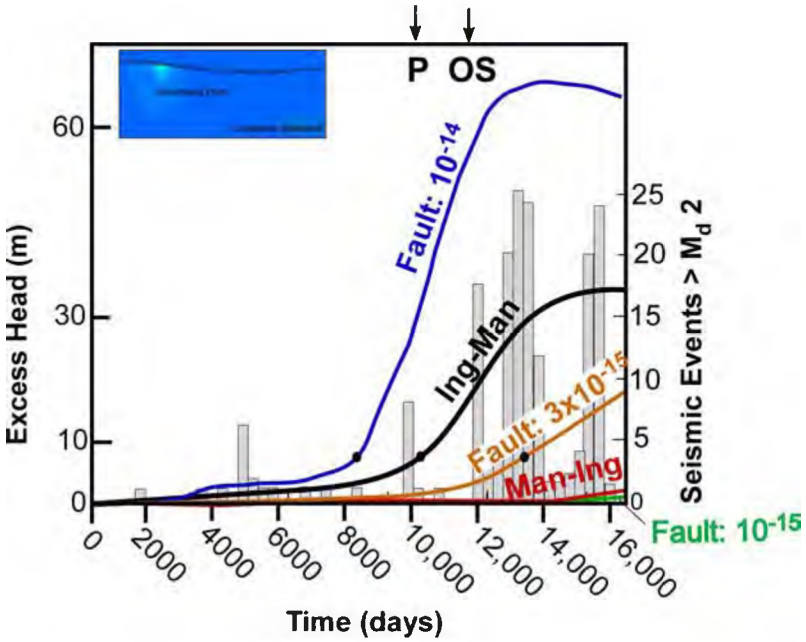

Figure 15. *Changes in excess head through time at crystalline basement monitoring point shown in inset. Lines show simulated excess heads for different basement permeability scenarios including the presence of a high permeability (10^{-12} m^2) fault zone, permeability decay with depth using the relationship presented by Ingebritsen and Manning (2010) and the presence of a relatively low permeability (10^{-16} m^2) weathered zone at the top of the crystalline basement cutting across a fault zone. The bar graph presents the number of earthquakes each year from 1960 to greater than M_d >2. The origin of the time axis is January 1, 1969. Peak injection (P) occurred after 10037 days (1996.5). The onset of increased seismic frequency (OS) began in 2001.*

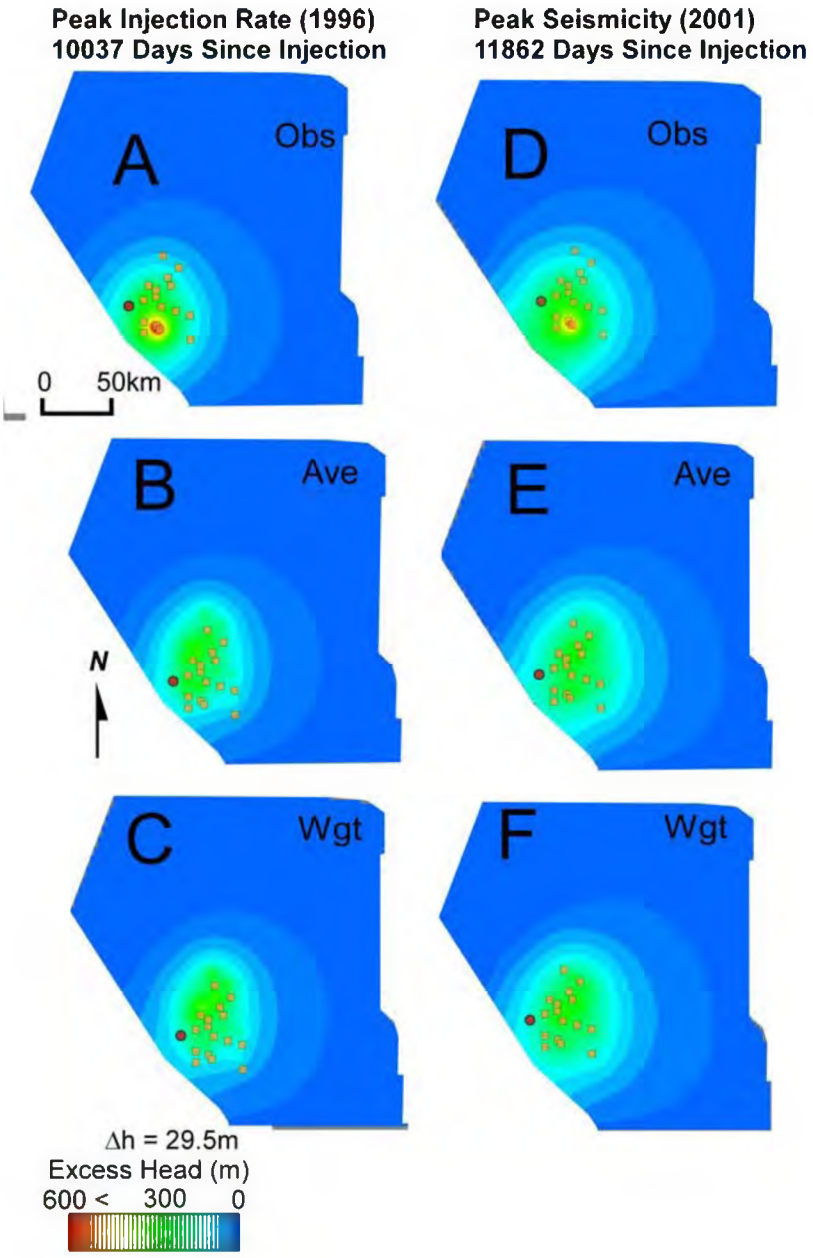

Figure 16. *Plan view map showing effects of changes in reservoir injection rates strategies on computed excess heads during peak injection (left column) and peak seismicity (right column). The crystalline basement permeability in all of these simulations was set at 10^{-15} m^2 (1 mD) and the reservoir permeability was 10^{-12} m^2 (1000 mD). The yellow squares denote the injection well locations. The red circle denotes the center of seismicity. The injection scenarios considered include the observed (Obs), average (Abs), and weighted by distance from no flow (southwest) assumed to represent a fault zone (Wgt). Subsequent contour intervals are 29.5 m (i.e. 7 m, 36.5 m, 66 m, 95.5 m, 125 m, … etc.). The top of the Ellenburger reservoir has a depth range between about 2430 m to 5250m below land surface.*

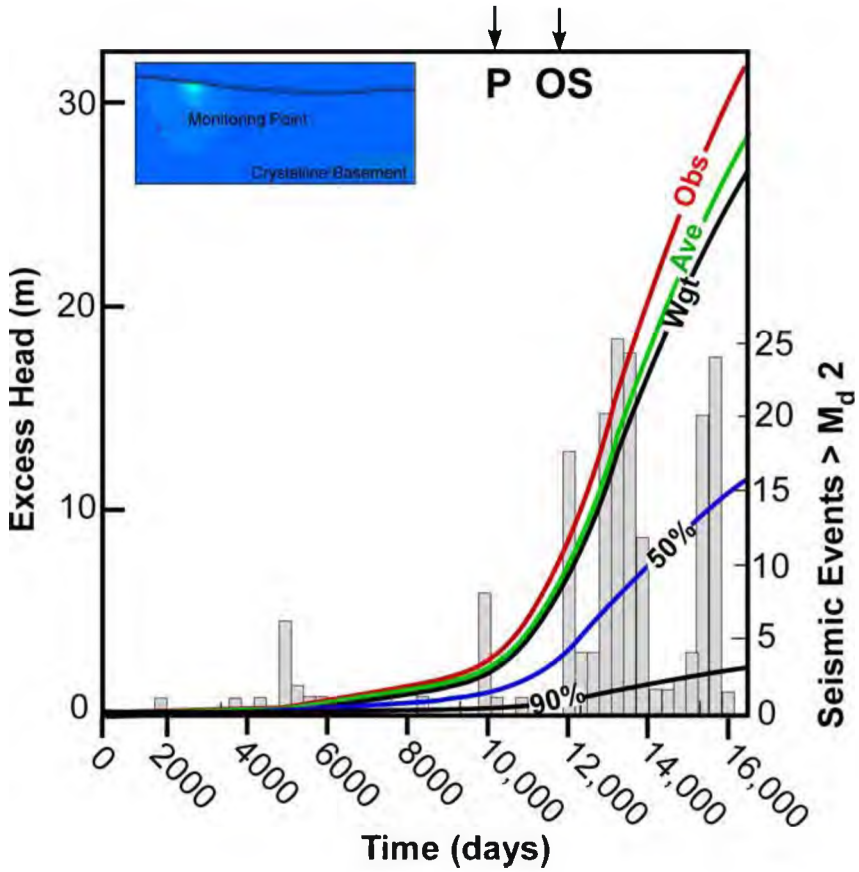

Figure 17. *Computed changes in excess head through time in response to different injection strategies evaluated at crystalline basement monitoring point shown in inset. Lines show simulated excess heads for different injection scenarios including the*
observed injection rates (Obs), the average injection rates (Ave), weighted injection rates (Wgt) with higher weights given to wells located furthest from the (southwest) no-flow boundary, a fifty percent reduction in the observed injection rates (50%), a ninety percent reduction in the observed injection rates (90%). In all model runs, the permeability of the crystalline basement was permeability was 10^{-15} m^2 and the Ellenberger reservoir was 10^{-12} m^2. The bar graph presents the number of earthquakes each year from 1960 to greater than M_d >2. The origin of the time axis is January 1, 1969. Peak injection (P) occurred after 10037 days (1996.5). The onset of increased seismic frequency (OS) began in 2001.

Modeling strain across mechanical sedimentary lithologic interfaces - geomechanical models derived from outcrop analysis

Elizabeth S. Petrie*

epetrie@western.edu

Department of Natural and Environmental Sciences – Geology, Western State Colorado University, 600 North Adams St., Gunnison, CO 81231

James P. Evans

james.evans@usu.edu

Geology Department Utah State University, 4505 Old Main Hill, Logan UT 84322-4505

*Corresponding author

ABSTRACT

In the brittle crust the distribution of natural rock fractures and their failure modes are a function of rock strength and its interactions between overburden pressure, pore-fluid pressure, and tectonic loading. The characterization of variability in rock strength and the associated changes in subsurface strain distribution is especially important for modeling the response of low-permeability rocks to changes in effective stress. This paper documents the effect variations in elastic mechanical properties have on the nature and distribution of fractures in the subsurface. Outcrop and geophysical wireline log evaluation of the Jurassic Carmel Formation and Navajo Sandstone was used to identify mechano-stratigraphic units and model subsurface strain distribution within sedimentary successions and across sedimentary interfaces.

Two finite element models were constructed and populated with elastic moduli derived from geophysical wireline data in order to understand where natural fractures form in rocks with varying layer thickness and elastic properties. Strain distribution results from a 3 layer and a 5-layer model are compared to the natural deformation response visible in outcrop. Model results show that more fractures are expected in high strain regions and fewer fractures in low strain regions. Strain variations are observed in both model scenarios and occur at material interface. The simple 3-layer model results in a smoothing of strain variations, while the 5-layer model captures strain variations that more closely match the fracture density observed in outcrop. Results from the 5-layer model suggests an interplay between Young's modulus and Poisson's ratio and that high strain regions form in thin (1-m thick) layers with moderate Young modulus (17.2 GPa) and Poisson ratio (0.26) values.

Outcrop observations and modeling results indicate that the potential for subsurface failure and fluid flow would not be restricted to the low fracture strength units but can cut vertically across interfaces of varying mechanical strength. Results from this work indicates that these types of models can be used to identify stratigraphic layers that are more prone to mechanical failure or identify layers that have more natural fractures or are more likely to form induced fractures.

INTRODUCTION

Interest in the mechanical behavior of fine-grained siltstone and mudstone successions stems from various geo-engineering applications, where these lithologies typically act as "impermeable" capillary seals in conventional petroleum systems or as top seals of subsurface waste repositories (Herzog, 2001; Warpinski et al., 2009); additionally organic-carbon-rich mudstone and siltstone are an increasingly important source rock reservoirs (EIA, 2013). Understanding the mechanical response of fine-grained heterolithic stratigraphic successions to changing stress conditions at fine spatial scales is essential for efficient development of unconventional resources and ensuring the security of subsurface fluid storage systems. Important unconventional reservoirs such as the Monteny, Horn River, Haynesville, Baaken, Barnett, and Marcellus Formations consist of thinly intercalated calcareous and siliciclastic siltstone, shale, and very fine grained sandstones (Ainsworth, 1994; Edwards et al., 1994; Hammes et al., 2011; Pyle et al., 2016; Slatt and Rodriguez, 2012). The lithologic variability exhibited in such formations plays an important role in fracture propagation, mode, and distribution of fractures in the subsurface. Vertical lithologic variability may have significant impact on resource extraction or prevention of seal bypass. Studying the occurrence of, and

50 changes in, outcrop fracture patterns and scaling these up for field-scale (km-scale)
51 modeling is difficult due to the lack of direct correlation between outcrop observations
52 and subsurface data.

53 This paper provides an analysis of field observations of fracture distribution
54 and morphology and tests the use of derived elastic properties from geophysical logs to
55 predict subsurface mechanical response to stress. In this case, the stress experienced
56 by a rock body, as an applied load, and its strain response, manifest in outcrop as
57 deformation features such as fractures, and derived from the finite element model as a
58 strain values. Finite element modeling is used to test changes in mechanical properties
59 at the metre scale and compare the results to observed outcrop fracture distribution.

60 Fractures, which include joints, veins, or small-displacement faults, occur within
61 fine-grained lithologies and can act as loci for fluid flow over various timescales
62 (Lacazette and Engelder, 1992). Open-mode fractures can propagate under low strain
63 conditions (Olson et al., 2009; Warpinski et al., 2009) and act as important permeable
64 pathways for subsurface fluid flow (Aydin, 2000; Laubach, 2003; Raduha et al., 2016;
65 Sibson, 1996; Warpinski et al., 1991). In stacked stratigraphic successions of variable
66 lithologies, fractures can terminate, bifurcate or become refracted with failure modes
67 (Mode I or II) changing between layers of differing mechanical properties (Ferrill et al.,
68 2012; Ferrill and Morris, 2003; Larsen et al., 2010; Morris et al., 1996; Sibson, 1994,
69 1996, 2003). Accurate predictive geologic models of fracture prone zones or zones of
70 preexisting fractures can be derived from geophysical data but needs calibration with
71 data from outcrop and/or core. The possibility of formation of new or the reactivation of
72 existing fractures in fine-grained lithologies requires development of accurate

73 geomechanical models that utilize appropriate mechanical properties and real-world
74 stratigraphy.

75 **STUDY AREA AND GEOLOGIC SETTING**

76 The top of the Jurassic Navajo Sandstone and the overlying Carmel Formation in
77 central Utah are examined as a natural analog for how fractures are distributed in
78 heterolithic successions. The outcrop locality occurs in a road-cut adjacent to I-70 (38°
79 51'0.60"N, 110°54'14.48"W), on the western limb of the San Rafael Swell, Utah and
80 shows evidence for past fluid migration and fracture propagation at the sub-metre scale
81 across mechanically distinct sedimentary boundaries (Figure 1 and 2).

82 The Jurassic Carmel Formation is a fine-grained mixed siliciclastic-carbonate
83 sedimentary succession that at the study locality represents deposition in the near-shore
84 marine to sabkha environment (Figure 2) (Blakey, 1994; Caputo, 2003; Hintze and
85 Kowallis, 2009). The well-exposed Carmel Formation is an excellent field analog for the
86 study of a heterolithic, low-permeability sedimentary succession, and is the caprock seal
87 to the underlying Navajo Sandstone (Figure 2). The Navajo Sandstone is a high
88 permeability aquifer and hydrocarbon reservoir deposited as part of an extensive
89 Jurassic erg system (Blakey, 1994).

90 The San Rafael Swell is an asymmetric, east-vergent, doubly plunging anticline
91 with a NNE-trending hinge-line (Bump and Davis, 2003; Davis and Bump, 2009; Gilluly,
92 1929). The San Rafael Swell developed from ~93 Ma to 58 Ma (Fouch et al., 1983;
93 Guiseppe and Heller, 1998; Lawton, 1985; Molenaar and Cobban, 1991; Shipton and

94 Cowie, 2001), due to east-west directed compression during the Sevier and Laramide
95 orogenic events.

96 Within the San Rafael Swell normal and normal-oblique faults strike WNW across
97 most of the San Rafael Swell and ENE in the southern portion. Normal faults strike NNE
98 around the outcrop location along the western limb of the San Rafael Swell (Figure 1)
99 (Bump and Davis, 2003; Doelling, 2002; Kelley and Clinton, 1960; Krantz, 1988; Shipton
100 and Cowie, 2001; Witkind, 1988). This change in extension direction in the northwestern
101 portion of the San Rafael Swell is likely associated with a change in stress field from that
102 of the Colorado Plateau, which is dominant across most of the structure to the Basin and
103 Range on its northwest flank (Heidbach et al., 2008; S. Janecke, 2013, personal
104 communication). Modern maximum principal stress orientation along the western limb of
105 the San Rafael Swell are NNE (~008° Az) (Heidbach et al., 2008).

106 This paper presents results from finite element analysis of geomechanical
107 models that are based on field observation of mechanical stratigraphy and dynamic
108 elastic moduli derived from geophysical borehole data over the reservoir seal interface
109 and an interbedded seal with variable lithologies. These models evaluate the strain
110 distribution within the modeled locked mechanical interfaces under a given load and do
111 not attempt to represent tectonic loads associated with formation of the San Rafael
112 Swell.

113 ## METHODS

114 The response of mixed carbonate-clastic successions is examined by populating
115 numerical-mechanical models with data derived from surface exposures and nearby

boreholes. The Carmel Formation was chosen for evaluation because of its thin intercalated nature of alternating limestone, mudstone, siltstone and shale as well as evidence for subsurface mechanical failure and fluid flow (Figure 3). Additionally, publically available geophysical bore hole data across the Navajo Sandstone and Carmel Formation allowed us to derived elastic moduli using geophysical wireline log data from offset boreholes (Petrie et al., 2012).

Results from geomechanical models are based on outcrop and geophysical wireline analysis over the basal 9 m of the Carmel Formation (caprock seal) and upper 3 m of the underlying Navajo Sandstone (reservoir) (Figure 4) (Petrie et al., 2012). The models and outcrop data presented here evaluate interfaces that are below resolution limits of most seismic reflection data (<10m) but are resolvable with borehole geophysics (61 cm). These models consider the impact of variation of two parametres on rock behaviors: changes in elastic properties and unit thicknesses within a stacked succession. Variations in local stress orientations and/or tensile stresses at the fracture tip have been considered by previous workers (Gudmundsson, 2009; Larsen et al., 2010).

The dynamic elastic moduli, Young's modulus and Poisson's ratio, calculated from geophysical wireline logs are used to quantify the elastic mechanical properties of the lower Carmel Formation and upper Navajo Sandstone. These dynamic elastic moduli are combined with the outcrop based mechano-stratigraphic interpretations to evaluate the potential for deformation (manifested as fractures) to exist in the subsurface (Petrie, et al., 2012). A history matching technique is used to compare finite element model (FEM) results to observed and measured field data (Schlumberger Oil Field

Glossary, 2013), in this paper the modeled strain distribution is compared to the deformation features observed in outcrop to understand the model fit and its potential predictive abilities.

OUTCROP METHODS

Fracture inventory data were collected at the outcrop location using scanlines, 2x2 m window surveys, and photogrammetry. These data include fracture orientation, distribution, termination, length and mineralization (La Pointe and Priest, 1983), in addition to field-derived compressive strength and permeability data. An N-type Schmidt hammer was used to collect estimates of unconfined compressive strength over the stratigraphic section; detailed methodology for these measurements are given in Selby (1993) and Petrie et al., (2012). Outcrop permeability data was collected using a TinyPerm II field permeameter (NER, 2012). Both the outcrop derived permeability and compressive strength measurements were obtained on clean surfaces away from cracks or outcrop edges to limit the effects of adjacent free surfaces. The outcrop data were used to identify mechano-stratigraphic divisions but likely overestimate permeability (Fossen et al., 2011), and underestimate compressive strength (Selby, 1993).

By combining these outcrop datasets, areas within the heterolithic seal were identified where changes in lithology(s) results in significant changes in deformation behavior. Each mechano-stratigraphic unit shows a similarity in fracture distribution, permeability, unconfined compressive rock strength and stratigraphic stacking pattern (Figure 4).

MODELING METHODS

161 The finite element modeling (FEM) method was used to examine how changes in
162 mechanical properties at the reservoir-seal interface and across sedimentologic
163 boundaries within the seal effect strain distribution. The free student version of
164 AbaqusFEA® (DassaultSystemes, 2011), a finite element analysis (FEA) software
165 program, was used to create geomechanical models for an elastic, deformable, layered-
166 solids. In this version of AbaqusFEA® the model domain is limited to analysis of 1000
167 nodes and following engineering convention the resultant numerical shortening strain
168 values are negative and extensional strain values are positive. AbaqusFEA® solves the
169 constitutive equations for elastic solids at nodes subjected to applied loads and the
170 boundary conditions. The resultant deformed block can be used to obtain strain values
171 at observation points anywhere within the block.

172 Models presented here examine a relatively small volume (12 m x 5 m x 5 m)
173 and involve stratigraphic changes over small distances (0.25 - 1m). Data for these
174 models were combined with the previously defined mechano-stratigraphic observations
175 (Petrie et al., 2012) and the calculated dynamic elastic moduli derived from offset
176 exploration and production boreholes to populate the geomechanical models with rock
177 properties and layer thickness. The models capture the lithologic heterogeneity within
178 the basal 9 m of the Carmel Formation and include the upper 3 m of the underlying
179 Navajo Sandstone reservoir (Petrie et al., 2012).

180 Physical properties required for each model include; Young's modulus, Poisson's
181 ratio, magnitude of horizontal and vertical stress (loads), and layer thickness.

182 *Elastic Moduli*

183 The calculation of the dynamic elastic parameters, Poisson's ratio, and Young's
184 modulus requires compressional velocity (V_p) and shear velocity (V_s). Velocity data can
185 be obtained directly from dipole sonic logs and previous workers have establish
186 empirical relationships between V_p, V_s, and lithology using global data sets of laboratory
187 measurements, seismic data, and wireline log data (Pickett, 1963; Castanga et al.,
188 1985).

189 Using data from two control wells in the Drunkards Wash field, Utah D7 (API: 43-
190 015-30338) and Utah D8 (API: 43-007-30431), which contain dipole sonic data, we
191 derive V_p and V_s directly from log data (Figure 5). Data from these wells are used to
192 evaluate the validity of deriving V_s from V_p data alone (Pickett, 1963; Castanga et al.,
193 1985) and were then used to calculate V_s from the available V_p logs in all other
194 boreholes (Figure 5). Evaluation of the Navajo Sandstone and Carmel Formation in
195 these two Drunkards Wash boreholes show three clear V_p-to-V_s relationships that can be
196 grouped by their GR value ranges, with GR serving as proxy for lithology. The V_p-to-V_s
197 relationships within these two control wells over specific GR values are comparable to
198 those established by previous workers for specific lithologies and mineralogies (Pickett,
199 1963; Castanga et al., 1985, Ellis and Singer, 2007), (for details on methodology see
200 Petrie et al., 2012). In the models presented here we use dynamic elastic moduli
201 derived from 43-015-30232 (Figure 5), the closest along strike offset borehole, ~12 km,
202 from the outcrop location.

203 Given the relationships observed in the control wells and the consistency of this
204 relationship with those previously published (Pickett, 1963; Castanga et al. 1985, Ellis
205 and Singer, 2007), we derive an estimate of shear velocity from V_p and in turn calculate

dynamic values for Poisson's ratio, equation 1, and Young's modulus, equation 2, for the interval of interest using compressional velocity wireline log data alone. McCann and Entwisle (1992) provide equations for solving Poisson's ratio (dynamic) ν_d:

$$\nu_d = \frac{1}{2}\left[\frac{\langle\frac{Vp}{Vs}\rangle^2 - 2}{\langle\frac{Vp}{Vs}\rangle^2 - 1}\right] \quad (1)$$

and Young's modulus (dynamic) E_d:

$$E_{d=}2 \times (V_s^2)(1 - \nu_d) \quad (2)$$

The linear relationships used in the calculations of shear velocity results in Poisson's ratio displaying an average value over each GR interval, equation 1 (Figure 6).

Stress Magnitude

The magnitude of applied stress in the multi-layered models was estimated by considering uniaxial strain conditions and calculating the magnitude of vertical (S_v) and horizontal (S_h) stress experienced in the subsurface at maximum burial depth. Maximum burial depth was determine by creating a burial history curve using OSXBackStrip (Cardozo, 2010) and is based on the compiled stratigraphic section for the San Rafael Swell (Hinzte and Kowalis, 2009). The burial history curve is uncorrected for compaction. Maximum stress is estimated for an Andersonian tectonic stress orientation in a normal fault regime ($S_v=\sigma_1$); where

$$S_v = \rho g z \quad (3)$$

$$S_H = S_h = \sigma_2 = \sigma_3 = \left(\frac{\nu}{1-\nu}\right)\left(S_v - P_p\right) \quad (4)$$

225 ρ is rock density (ρ=2.6 g/cm^3), g is the gravitational acceleration (g=9.823 m/s^2), ν is
226 Possion's ratio , where we use a nominal value of ν=0.25 for the calculation of far field
227 horizontal stresses, and P_p is hydrostatic pore fluid pressure (Anderson, 1951; Eaton,
228 1969; Engelder, 1993). The magnitude of S_v is based on the lithostatic load (equation 3)
229 and maximum burial depth estimated as 4.4 km. A uniaxial strain model is used to solve
230 for the horizontal stresses S_h and S_H; where S_h and S_H are equal and represent the
231 principal stresses σ_2 and σ_3.

232 *Model Parameters*

233 Two model scenarios were built; each based on stratigraphic thickness variations
234 that are too small to be detected by high resolution reflection seismic data, but in outcrop
235 show variability in fracture distribution and whose geophysical wireline data show clear
236 variations in derived elastic moduli (Figure 6). Each model is 12 m x 5 m x 5 m in total
237 size. Individual model layer thicknesses are based on the mechanical stratigraphy
238 defined by outcrop and/or elastic moduli. Each layer was built using the thickness value
239 and assigned material properties listed in Table 1, each layer is treated as solid cell
240 within the model. The layers where then assembled with locked interactions between
241 layers, the assembly was meshed and horizontal and vertical loads applied.

242 *Boundary conditions*

243 The boundary conditions and applied loads for each model scenario are identical.
244 Each scenario has a fixed base (0 strain) and is under vertical and horizontal loads
245 defined by the estimated S_v (σ_1) and S_h (σ_2 and σ_3) values (Equations 3 & 4). The
246 vertical load estimate S_v is 113 MPa and S_h is estimated to be 66.5 MPa (Equation 4 &

247 Figure 6). The FEA was conducted in a single step applying the vertical and horizontal
248 stresses as uniform pressure to all sides except the fixed base. Since we assume S_H =
249 S_h, and to make the problem tractable, we consider a plane strain problem, in order to
250 solve exactly for stresses and strains in the model. Thus we allow no deformation
251 occurring in the x plane (Figure 7), where a fixed base prevents deformation. The fixed
252 base boundary condition means constraint on all displacements and rotation at nodes
253 (U1=U2=U3=UR1=UR2=UR3=0); where U are translation UR are rotation axes.

254

255 *Model layers*

256 Model I is a three-layer model based on field observations of mechanical
257 stratigraphy alone and Model II is based on a combination of the outcrop-defined
258 mechanical stratigraphy and observed variability in calculated elastic moduli from
259 geophysical logs (Figure 6). The variations in physical properties (layer thickness, E,
260 and ν) between the model scenarios are listed in Table 1.

261 Model I has layer thicknesses based on outcrop mechano-stratigraphic divisions.
262 Elastic moduli for model I were averaged from the wireline logs, that is the upper 3 m of
263 the Navajo Sandstone reservoir, and two divisions within the Carmel Formation of 4 m
264 and 5 m each (Figure 6A & Table 1). In Model I ν is fixed and E varies based on
265 average E values over the layer thickness.

266 Model II also used the average elastic moduli in the upper 3 m of the Navajo
267 Sandstone. Layer distribution and associated elastic moduli within the seal are based
268 on changes in gamma ray lithology over wireline log thickness greater than 61 cm that

269 are also associated with shifts in Young's modulus (≥10 GPa) and Poisson's ratio
270 (Figure 6B & Table 1). Using these criteria two layers were added the middle of Model II
271 these are associated with lithologic changes observable in GR logs within mechano-
272 stratigraphic unit 2 & 3. Model II explicitly breaks out the fine-grained intervals in the Co-
273 Op Creek and lower Crystal Creek Members. In model II, ν varies from 0.21 to 0.30 (~
274 25 % variation over typical values for sedimentary rocks) and E varies from 17.2 to 33.7
275 GPa, which is up that 50% variation for typical values in sedimentary rocks.

276 In each FEM scenario the grid blocks are defined by the layer thickness, and
277 strain values are computed at each node point where node points are defined by the
278 intersection points of each grid block. Strain values from the models are displayed as
279 the maximum principal strain (horizontal) taken at the vertical observation points near
280 the center of each deformed model (Figure 8 & 9). Because the lower boundary is a
281 fixed plane of zero strain, the model domain was configured to examine strains in the
282 caprocks, boundary effects occur within the basal unit.

283 The strain response of model layers 2 through 5 were evaluated with regard to
284 the elastic properties to understand the interplay between elastic moduli and resultant
285 deformation by employing a history matching technique, borrowed from reservoir
286 engineering, (Schlumberger Oil Field Glossary, 2013). This compares FEM strain
287 distribution results to the observed outcrop fracture distribution to understand the
288 importance of heterogeneity and the detail required to capture strain distributions that
289 are representative of the observed fracture distribution. In this case the FEM results are
290 used to evaluate the detail required to predict the presence of fracture or potential for

291 inducing fractures. In outcrop, layers with higher fracture densities are thought to have
292 experienced more strain thus allowing for comparison to the model results.

293 ## RESULTS

294 ### Field Observations

295 At the study locality the Carmel Formation dips gently (09 ± 02°W), and all 4
296 members are exposed in a partial section (Figures 1 and 2)(Petrie et al., 2012). The
297 basal portion of the Carmel Formation consists thin- to medium-bedded, quartz-bearing
298 pelloidal micrite, thin- to medium-bedded bioclastic wackestone, calcareous mudstone
299 and shale of the Co-op Creek and lower Crystal Creek Members. These fine-grained
300 low-permeability units ($1.5x10^{-15}$ to 5.2×10^{-14} m^2) unconformably overly the Navajo
301 Sandstone reservoir and are considered in this study to be the primary seal (Figures 2
302 and 4). Lithologic interfaces mark the boundary between mechanical units and fractures
303 are observed to refract, bifurcate, propagate across, or arrest at these boundaries
304 (Figure 3).

305 The uppermost portion of the Crystal Creek Member consists of medium to thick-
306 bedded gypsiferous sandstone, mudstone and anhydrite beds; the Crystal Creek
307 Member is overlain by siltstone and mudstone of the Paria River Member. At this
308 outcrop only the lowermost portion of the Winsor Member is exposed, which is an
309 interbedded micritic limestone, calcareous mudstone and siltstone. Prior analysis (Petrie
310 et al., 2012) characterized the entire 37-m thick section (Figure 2) and has shown that
311 veins cross-cut lithologic boundaries and extend up to 10 m vertically from the reservoir
312 seal into the overlying Carmel Formation (Petrie et al., 2012). This outcrop data

313 delineated 5 mechano-stratigraphic units based on similarities in fracture spacing, bed
314 thickness, Schmidt hammer-derived unconfined compressive strength, and air
315 permeability measurements (Figure 4) (Petrie et al., 2012).

316 Field-derived unconfined compressive rock strength and permeability estimates
317 vary stratigraphically within the Carmel Formation (Petrie et al., 2012). Average
318 compressive rock strength is lowest in the Navajo Sandstone and increases up-section
319 with the highest average unconfined compressive rock strength and lowest average
320 permeability occurring in the thinly bedded heterolithic portion of the lower Carmel
321 Formation (Figure 4). The lithologic heterogeneity of this portion of the Carmel
322 Formation imparts varied mechanical properties over scales of 10 cm to 1 m (Figure 4).
323 Fractures are preserved as calcite veins in the limestone lithologies or as shear fractures
324 in the mudstone and shale lithologies and are characterized by limonite fracture margins
325 and calcite or gypsum veins in the fracture center (Figure 3) (Petrie, et al., 2012).

326 The finite element models presented here examine the lower 9m of the seal and
327 upper 3 m of the reservoir encompasses mechano-stratigraphic units 1, 2, and 3 (Figure
328 3). The lowermost mechanical unit, unit 1, (Figure 3), is the Navajo Sandstone reservoir,
329 a high permeability ($1.03e^{-11}$ m^2), thick-bedded (8 to 10 m), low fracture density (1.9
330 fractures per m) quartz arenite. Fractures within the Navajo Sandstone include open
331 joints and fault deformation bands. Unit 2 is composed of interbeds of thin-bedded
332 quartz-rich limestone, siltstone, mudstone, and shale; this unit coarsens and becomes
333 more fossiliferous upsection. Unit 2 has a much lower permeability than the underlying
334 reservoir interval with an average permeability of $3.55e^{-13}$ m^2 and a higher normalized
335 median fracture density of 4.7 fractures per m. Unit 3 is finer-grained; has a lower

336 average permeability than the other two mechanical units, ($9.87e^{-14}$ m^2), is more thinly
337 bedded and has a higher fracture density, (6.0 fractures per metre) than the underlying
338 unit 2 (Figure 3).

339 Veins, step-over fractures, refracted normal faults and bifurcated fractures are
340 common in mechano-stratigraphic units 2 and 3, and low angle to bedding fractures are
341 observed within the shale layers (Figure 3A-C). Dilational jogs are common across the
342 lithologic interface with calcite veins occurring in limestone facies and transitioning to
343 shear fractures within the over and underlying mudstone or shale facies (Figure 3D).
344 Calcite veins, limonite and gypsum veins are symmetric indicating that open mode and
345 shear fractures were the loci of fluid flow. In thin-section mechanical twins are observed
346 within the calcite veins and their presence indicates that fracture opening and
347 mineralization occurred at some depth prior to further deformation and formation of
348 twinning lamella. Similar near vertical calcite veins occur throughout the Carmel
349 Formation at this and other localities in the San Rafael (Barton, 2011; Raduha et al.,
350 2016).

351 Fractures at this outcrop exhibit two dominant strike orientations - NNW and NNE
352 (Figure 8). The majority of fractures within the Carmel Formation, including veins, and
353 fault deformation bands in the Navajo Sandstone strike NNW. Within the Carmel
354 Formation, the carbonate mudstone, mudstone, and siltstone horizons of the Carmel
355 Formation exhibit a greater dispersion in strike orientations than the limestone and
356 sandstone lithologies (Figure 8B).

357 **Model Results**
358

359 The boundary conditions applied to the 3D-block models require that as in nature
360 they remain blocks, and as such predict changes in strain distribution and localization at
361 and across interfaces because of the varied mechanical properties of the rock. Both
362 model configurations predict localized strain transitions with strain variations across the
363 reservoir seal interface and in Model scenario II at unit boundaries within the seal
364 (Figures 9 & 10). Edge effects at the block boundaries are noted and may be the result
365 of model size or applied boundary conditions, for this reason strain values were taken
366 near the center of each deformed model to avoid edge effects.

367 Model I depicts a 3-layer sequence with values of E_d and ν_d derived from wireline
368 logs averaged over the unit thickness defined by outcrop mechanical stratigraphy alone
369 (Figures 6 & 9). The lowest strain magnitude occurs within the reservoir, and increases
370 toward the boundary between the reservoir and overlying seal. Within the seal strain
371 values are similar and decreases slightly upward (Figure 9). The scale at which the
372 mechanical unit thickness and elastic moduli values were averaged results in
373 homogenization of strain values within the seal. This strain homogenization is not
374 supported when compared to fracture densities observed outcrop (Figure 9). However,
375 the higher strain values within the caprock seal relative to that of the underlying reservoir
376 suggest that the seal would be prone to mechanical failure, fracture formation and
377 propagation across the reservoir-seal interface and creation of fracture permeability
378 allowing fluid to flow vertically across intra-seal interfaces.

379 In contrast, Model II depicts 5 layers, in which mechanical properties are based
380 on finer scale shifts in dynamic elastic moduli values and lithologic variations observed in
381 the wireline logs (Figure 6). Addition of two low E_d and moderate ν_d values increases the

382 heterogeneity within this model and characterizes the shale-rich layers of the lower
383 Carmel Formation and in the model are isolated by stiffer, more incompressible layers
384 (higher E_d and ν_d) (Figure 6).

385 The vertical strain profile from Model II shows a decrease in strain magnitude
386 across the reservoir-seal interface and an increase in strain magnitude across the shale
387 layers (units 2 and 4) within the caprock seal. These results highlight the importance of
388 using accurate estimates of Poisson's ratio and Young's modulus in a stacked
389 stratigraphic succession. In general, rocks with larger values Young's modulus may be
390 prone to fracture because they are stiffer, however as Model II shows variation in values
391 of Poisson's ratio also plays an important role in strain distribution.

392 Units 2 and 4 have ν values higher than that of the underlying reservoir but lower
393 than adjacent beds within the seal, and low E relative to the reservoir and surrounding
394 seal. The heterogeneity in mechanical properties and the interaction between changing
395 values of Poisson's ratio and Young's modulus results in: 1) a decrease in strain values
396 at the reservoir-seal interface at unit 1 / unit 2 interface, 2) an increase in strain between
397 unit 2 and unit 3 which corresponds to an increase in observed fracture density in
398 outcrop, and 3) a marked increase in strain values within unit 4 (Figure 10). The strain
399 distribution results suggest that fractures would not necessarily tip out within the shale
400 layers but might propagate across boundaries potentially as shear fractures, as
401 observed in outcrop (Figure 2). Unit 5 has the largest values for E and ν and the highest
402 strain values within the entire seal interval, and this is reflected in outcrop as high
403 fracture density within this mechano-stratigraphic unit (Figures 4). Unit 5 shows an
404 overall decrease in strain up-section, and this decrease in strain at the top of unit 5 may

405 be a modeling artifact associated to its position within the model or due to layer
406 thickness (Bai and Pollard, 2000; Gross, 1993).

407 In Model II abrupt changes in strain values are observed across all mechanical
408 unit interfaces. Using the nature of strain distribution in these models as a proxy for
409 fracture distribution, regions of increasing strain values across interfaces indicate layers
410 that are likely fractured or will fracture due to increased pore fluid pressure (reduced
411 effective stress), or differential stress. Model II results capture more variability in strain
412 distribution as well as larger shifts in strain magnitude at and across interface
413 boundaries than Model I. The additional layers in this model provide an overall better
414 match to the observed fracture distributions in outcrop and preserve its heterogeneity.

415 The variability in mechanical properties in the models presented here result in
416 strain distributions that suggest: 1) strain magnitudes change at interface boundaries, 2)
417 thin shale layers do not prevent fracturing or inhibit propagation of fractures across
418 interface boundaries (Larsen et al., 2010; Rijken and Cooke, 2001), 3) fractures can be
419 widespread within a heterolithic package, and 4) the interplay between elastic moduli
420 and unit thickness will affect modeled strain distribution. In order to capture the natural
421 heterogeneity in fracture distributions realistic values of elastic moduli must be applied to
422 model scenarios.

423 **Discussion**

424 The field observations of the coincident orientation of veins and deformation
425 bands and fractures within the Carmel formation suggests a similar history of formation
426 and timing of deformation. The veins observed in the Camel Formation and the fault

deformation bands in the Navajo Sandstone likely represent paleo-stress directions related to the Laramide uplift and associated deformation along the western edge of the San Rafael Swell (Anderson and Barnhard, 1986; Davis and Bump, 2009). Joints in the Carmel Formation and Navajo Sandstone are oriented NNE this fracture set is interpreted as reflecting the present day maximum horizontal principal stress orientation (Figure 8) (Heidbach et al., 2008).

The calcareous siltstone, mudstone, and shale lithologies of the Carmel Formation exhibit a greater dispersion in strike orientation of fractures (Figure 8B). This dispersion and its association with lithology suggest that each lithology responds differently to stress. In a stratigraphic succession with lithologic changes variable fracture distributions are likely and will affect fracture patterns and in turn fluid flow pathways at depth (Ferrill et al., 2012; Sibson, 1996). This may be due to the development of tensile stress ahead of the fracture tip, rotation of localized stress orientation at lithologic boundaries, and/or variation in elastic properties across interfaces (Larsen et al., 2010).

Field observations suggest that stratigraphic heterogeneity has influenced the variability in fracture pattern, rock strength and permeability throughout this exposure of the Carmel Formation (Petrie et al., 2012). Higher fracture densities, permeability, and compressive rock strength are observed in the thinly bedded heterolithic facies of mechano-stratigraphic units 2 and 3 of the Carmel Formation (Figure 3), these continuous fractures are observed as fault deformation bands in the reservoir and as veins or shear fractures in the overlying sealing stratigraphy (Figure 3).

449 Modeling results indicate that the potential for subsurface failure and fluid flow
450 would not be restricted to the low fracture strength units (incompressible and stiff, large ν
451 and large E values). Comparison of the model results highlights the importance and
452 effect of small-scale (<1 m) stacked variations of elastic moduli and the importance
453 capturing E_d and ν_d variations to model results. Understanding or predicting where
454 natural fractures occur or induced fractures are most likely to propagate requires
455 incorporation of data that is representative of stratigraphy at the sub-seismic scale. At
456 low effective confining pressures, mechanical failure may occur by slip across faults or
457 by development of open-mode or hybrid shear fracture networks, and these types of
458 failure are important in forming fluid-flow pathways in low-permeability rocks (Sibson,
459 1996) (Figure 11). Observations made in outcrop, in this and other studies, shows that
460 changing mechanical properties between sedimentary layers effects vertical connectivity
461 of fractures due to refraction and changes in failure mode as well as termination,
462 deflection, bifurcation and occurrence of bed parallel slip (Ferrill and Morris, 2003;
463 Larsen et al., 2010; Petrie et al., 2012; Raduha et al., 2016). Although the model results
464 presented are not used to predict failure mode they do highlight the importance of strain
465 distributions within and across layers of changing mechanical properties and the results
466 suggest that layered models can be used to identify zones of high strain and high natural
467 fracture densities as well as zones in which mechanical failure and fracture propagation
468 may occur more readily.

469 **CONCLUSIONS**
470
471 We develop a method to use field-based observations and wireline log data to
472 determine the elastic properties of thin-bedded rocks, and show how deformation in

these rocks can be modeled with finite element methods to understand rock fracture in thin-bedded rocks. The results presented here can be used to understand the effect variations in elastic properties have on strain distributions at and across stratigraphic interfaces. This evaluation bridges the correlation gap between outcrop and subsurface environments by evaluating the meso-scale (cm to m) variability observed in outcrop, incorporating these observations into a mechano-stratigraphic framework and then to a geomechanical model populated with borehole-derived dynamic elastic moduli. Integration of field (analog) and subsurface datasets for appropriate modeling of the geomechanical response of heterolithic, fine-grained, low-permeability rocks is key in producing accurate model results. The strain distributions in the models indicate that fractures would propagate across mechanical boundaries; this result is supported by field observations. Variations in strain magnitudes across locked mechanical interfaces occur in both model scenarios, suggesting that an elastic mismatch between layers can result in significant changes to strain distribution in the subsurface. Both models suggest that strain values vary within the different horizons, imply that the interaction between the elastic moduli across horizons plays an important role in the distribution of strain in the subsurface.

The more detailed model scenario, conditioned on outcrop and subsurface constraints for the fundamental elastic moduli, is a more accurate predictor of subsurface strain distribution and expected deformation. Comparing the outcrop fracture distribution to the model strain results show that variability in strain distribution can be used to predict the natural deformation response manifested as more fractures in high strain regions. Although neither model is able to replicate some of the thin bed (< 0.5 m), high fracture density units, the use of both mechanical stratigraphy and wireline-derived

497 dynamic elastic moduli allowed for better overall prediction of strain distribution in the
498 subsurface. Elastic mismatch across interfaces leads to strain differential and the model
499 results highlight the importance of rock properties and the interactions between layers to
500 understanding subsurface fracture distribution.

501

ACKNOWLEDGEMENTS

This research was supported by grants from the GDL Foundation Fellowship to Petrie and DOE grant # DE-FC26-0xNT4 FE0001786, software and software support came from SMT Kingdom Software – University Grant and Sirovision Software – University Grant and Dassault Systèmes for providing a free student version of Abaqus CAE. We thank Joseph Bishop for insights in the use of Abaqus and FEA procedures. The authors thank fellow researchers within the USU Department of Geology structure group for their feedback and discussions and Alvar Braathan for use of the TinyPermII. We thank the Editor in Chief and the Associate Editor of the Bulletin of Canadian Petroleum Geology and manuscript reviewers Mark Cooper and Byron Veilleux for their time and thoughtful comments that improved this paper.

REFERENCES

Ainsworth, R. B., 1994, Marginal Marine Sedimentology and High Resolution Sequence Analysis; Bearpaw-Horseshoe Canyon Transition, Drumheller Alberta: CSPG Bulletin, v. 42, p. 26-54.

Anderson, E. M., 1951, The dynamics of faulting and dyke formation with application to Britain: Edinburgh, Oliver and Boyd, p. 191.

Anderson, R. E., and T. P. Barnhard, 1986, Genetic relationship between faults and folds and determination of Laramide and neotectonic paleostress, Western Colorado plateau-trasition zone, Central Utah Tectonics, v. 5, p. 335-357.

Aydin, A., 2000, Fractures, faults, and hydrocarbon entrapment, migration and flow: Marine and Petroleum Geology, v. 17, p. 797-814.

Bai, T., and D. D. Pollard, 2000, Fracture spacing in layered rocks: a new explanation based on the stress transition: Journal of Structural Geology, v. 22, p. 43-57.

Barton, D. C., 2011, Determining CO2 storage potential: Characterization of seal integrity and reservoir failure in exposed analogs: Geology thesis, Utah State University, Logan, UT, 177 p.

Blakey, R. C., 1994, Paleogeographic and tectonic controls on some Lower and Middle Jurassic erg deposits, Colorado Plateau, in M. V. Caputo, J. A. Peterson, and K. J. Franczyk, eds., Mesozoic systems of the Rocky Mountain region, USA, p. 273-298.

534 Bump, A. P., and G. H. Davis, 2003, Late Cretaceous–early Tertiary Laramide
535 deformation of the northern Colorado Plateau, Utah and Colorado: Journal of
536 Structural Geology, v. 25, p. 421-440.
537 Caputo, M. V., 2003, Geology of the Paria Canyon - Vermilion Cliffs Wilderness, Utah
538 and Arizona, in D. A. Sprinkel, T. Chidsey, and A. P. B., eds., Geology of Utah's
539 Parks and Monuments Utah Geological Association Pbulicaiton, v. 28: Salt Lake
540 City, Utah Geological Association adn Bryce Canyon Natural History Association,
541 p. 531-561.
542 Cardozo, N., 2010, OSXBackstrip.
543 DassaultSystemes, 2011, Abaqus FEA.
544 Davis, G. H., and A. P. Bump, 2009, Structural geologic evolution of the Colorado
545 Plateau, in S. M. Kay, V. A. Ramos, and W. R. Dickinson, eds., Backbone of the
546 Americas: Shallow subduction, plateau uplift, and ridge and terrane collision,
547 Geological Society of America Memoir 204, p. 99-124.
548 Doelling, H. H., 2002, Interim Geologic Map of the San Rafael Desert 30'x60'
549 Quadrangle, Emery and Grand Counties, Utah: Utah Geological Survey Open-
550 File Report 104.
551 Eaton, B. A., 1969, Fracture gradient prediction and its application to oilfield operations:
552 journal of Petroleum Technology, v. 21, p. 1353-1360.
553 Edwards, D. E., J. E. Barclay, D. W. Gibson, G. E. Kvill, and E. Halton, 1994, Triassic
554 Strata of the Western Canada Sedimentary Basin, in G. D. Mossop, and I.
555 Shetsen, eds., Geologic Atlas of the Western Canada Sedimentary Basin,
556 Canadian Society for Petroleum Geologist and Alberta Research Council, p. 259-
557 275.
558 EIA, 2013, Technically Recoverable Shale Oil and Shale Gas Resources: An
559 Assessment of 137 Shale Formations in 41 Countries Outside of the United
560 States, in U. S. E. I. Administration, ed., Washington, D.C., U. S. Department of
561 Energy.
562 Engelder, T., 1993, Stress Regimes in the Lithosphere: Princeton, Princeton University
563 Press.
564 Ferrill, D. A., R. N. McGinnis, A. P. Morris, and K. J. Smart, 2012, Hybrid failure: Field
565 evidence and influence on fault refraction: Journal of Structural Geology, v. 42, p.
566 140-150.
567 Ferrill, D. A., and A. P. Morris, 2003, Dilational normal faults: Journal of Structural
568 Geology, v. 25, p. 183-196.
569 Fouch, T. D., T. F. Lawton, D. J. Nichols, W. B. Cashion, and W. A. Cobban, 1983,
570 Patterns and timing of synorogenic sedimentation in Upper Cretaceous rocks of
571 central and northeast Utah, in M. W. Reynolds, and E. D. Dolly, eds., Mesozoic
572 paleogeography of the west-central United States, Rocky Mountain
573 Paleogeolgraphy Symposium 2, p. 305-336.
574 Gilluly, J., 1929, Geology and oil and gas prospects of part of the San Rafael Swell,
575 Utah: U.S. Geological Survey Bulletin 806-C.
576 Gross, M. R., 1993, The origin and spacing of cross joints: Examples from Monerey
577 Formation, Santa Barbara coastline, California: Journal of Structural Geology, v.
578 15, p. 737-751.
579 Gudmundsson, A., 2009, Toughness and failure of volcanic edifices: Tectonophysics, v.
580 471, p. 27-35.

581 Guiseppe, A. C., and P. L. Heller, 1998, Long-term river response to regional doming in
582 the Price River Formation, central Utah: Geology, v. 26, p. 239-242.
583 Hammes, U., H. S. Hamlin, and T. E. Ewing, 2011, Geologic analysis of the Upper
584 Jurassic Haynesville Shale in east Texas and west Louisiana: AAPG Bulletin, v.
585 95, p. 1643-1666.
586 Heidbach, O., M. Tingay, A. Barth, J. Reinecker, D. Kurfeb, and B. Muller, 2008, The
587 World Stress Map database release 2008.
588 Herzog, H. J., 2001, What Future for Carbon Capture and Sequestration?:
589 Environmental Science & Technology, v. 35, p. 148A-153A.
590 Hintze, L. F., and B. J. Kowallis, 2009, Geologic History of Utah: Brigham Young
591 University Geology Studies Special Publication 9, v. 9: Provo, Brigham Young
592 University Press.
593 Hintze, L. F., G. C. Willis, D. Y. M. Laes, D. A. Sprinkel, and K. D. Brown, 2000, Digital
594 Geologic Map of Utah: Utah Geological Survey Digital State Map.
595 Kelley, V. C., and N. J. Clinton, 1960, Fracture Systems and Tectonic Elements of the
596 Colorado Plateau: University of New Mexico Publications in Geology v. 6:
597 Albuquerque, University of New Mexico Press, 104 p.
598 Krantz, R. W., 1988, Multiple fault sets and three-dimensional strain: theory and
599 application: Journal of Structural Geology, v. 10, p. 225-237.
600 Lacazette, A., and T. Engelder, 1992, Fluid-driven cyclic propagation of a join in the
601 Ithaca Siltstone, Appalachain Basin, New York, in B. Evans, and T. Wong, eds.,
602 Fault Mechanics and Transport Properties of Rocks - A Festschrift in Honor of W.
603 F. Brace, v. 51, Elsevier.
604 Larsen, B., A. Gudmundsson, I. Grunnaleite, G. Saelen, M. R. Talbot, and S. J. Buckle,
605 2010, Effects of sedimentary interfaces on fracture pattern, linkage, and cluster
606 formation in peritidal carbonate rocks.: Marine and Petroleum Geology, v. 27, p.
607 1531-1550.
608 Laubach, S., 2003, Practical approaches to identifying sealed and open fractures:
609 American Association of Petroleum Geologist Bulletin, v. 87, p. 561-579.
610 Lawton, T. F., 1985, Style and timing of frontal structures, thrust belt, central Utah:
611 American Association of Petroleum Geologist Bulletin, v. 69, p. 1145-1159.
612 Molenaar, C. M., and W. A. Cobban, 1991, Middle Cretaceous stratigraphy on the south
613 and east sides of the Uinta Basin, northeastern Utah and northwestern Colorado:
614 United States Geological Survey Bulletin, v. 1787-P, p. 34.
615 Morris, A., D. A. Ferrill, and D. B. Henderson, 1996, Slip-tendency analysis and fault
616 reactivation: Geology, v. 24, p. 275-278.
617 New England Research (NER), 2012, TinyPerm II, portable permeameter
618 http://ner.com/pdf/tinyperm.pdf. (accessed June 2011).
619 Olson, J. E., S. E. Laubach, and R. H. Lander, 2009, Natural fracture characerization in
620 tight gas sandstones: Integrating mechanics and diagenesis: American
621 Association of Petroleum Geologist Bulletin, v. 93, p. 1535-1549.
622 Petrie, E. S., D. C. Barton, and J. P. Evans, 2013, Tectonic history and distribution of
623 faults and fractures in the San Rafael Swell, Utah: Impacts on subsurface fluid
624 flow., in T. Morris, and R. Ressetar, eds., San Rafael Swell and Henry Mountains
625 Basin, v. 24: Salt Lake City, Utah Geological Association.

626 Petrie, E. S., T. N. Jeppson, and J. P. Evans, 2012, Predicting rock strength variability
627 across stratigraphic interfaces in caprock lithologies at depth: Correlation
628 between outcrop and subsurface: Environmental Geosciences, v. 19, p. 125-142.
629 Pyle, L. J., Gal, L. P., and Chow, N., 2016, Reference section for the Horn River Group
630 and definition of the Bell Creek member, Hare Indian Formation, in central
631 Northwest Territories, Bulletin of Canadian Petroleum Geology, v. 64, p. 67-98.
632 Raduha, S., D. Butler, P. Mozley, M. Person, J. Evans, J. Heath, T. Dewers, P. Stauffer,
633 C. Gable, and S. Kelkar, 2016, Potential seal bypass and caprock storage
634 produced by deformation-band-to-opening-mode-fracture transition at the
635 reservoir/caprock interface: Geofluids.
636 Rijken, P., and M. L. Cooke, 2001, Role of shale thickness on vertical connectivity of
637 fractures: application of crack-bridging theory to the Austin Chalk, Texas:
638 Tectonophysics, v. 337, p. 117-133.
639 Shipton, Z. K., and P. A. Cowie, 2001, Damage zone and slip-surface evolution over μm
640 to km scales in high-porosity Navajo sandstone, Utah: Journal of Structural
641 Geology, v. 23, p. 1825-1844.
642 Sibson, R. H., 1994, Crustal stress, faulting and fluid flow: Geological Society, London,
643 Special Publications, v. 78, p. 69-84.
644 Sibson, R. H., 1996, Structural permeability of fluid-driven fault-fracture meshes: Journal
645 of Structural Geology, v. 18, p. 1031-1042.
646 Sibson, R. H., 2003, Brittle-fault controls on maxium sustainable overpressure in
647 different tectonic regimes: AAPG Bulletin, v. 87, p. 901-908.
648 Slatt, R. M., and N. D. Rodriguez, 2012, Comparative sequence stratigraphy and organic
649 geochemistry of gas shales: Commonality or coincidence?: Journal of Natural
650 Gas Science and Engineering, v. 8, p. 68-84.
651 Warpinski, N. R., M. J. Mayerhofer, M. C. Vincent, C. L. Cipolla, and E. P. Lolon, 2009,
652 Stimulating Unconventional Reservoirs: Maximizing Network Growth While
653 Optimizing Fracture Conductivity: Journal of Canadian Petroleum Technology, v.
654 48, p. 39-51.
655 Warpinski, N. R., L. W. Teufel, and D. C. Graf, 1991, Effect of stress and pressure on
656 gas flow through natural fractures: Proceedings, 1991 SPE Annual Technical
657 Conference and Exhibtiion, v. 6-9, p. 105-118.
658 Witkind, I. J., 1988, Geologic Map of the Huntington 30' X 60' Quadrangle, Carbon,
659 Emery, Grand, and Uinta Counties, Utah:: U.S. Geological Survey map i-1764.

660

661 Figure and Table Captions

662 Figure 1. Generalized geologic map of the San Rafael Swell showing the location of
663 major faults and the approximate axial surface of the San Rafael Swell. The detailed
664 surface geology of the study area is shown on the left. Maps are modified from (Barton,
665 2011; Hintze and Kowallis, 2009; Hintze et al., 2000; Petrie et al., 2013)

666 Figure 2. Measured stratigraphic section at the outcrop location with outcrop photograph
667 showing the stratigraphy modeled in this paper.
668

669 Figure 3. Outcrop photographs, vertical cross-section view, showing outcrop examples
670 of fracture morphology and interaction. Sketch maps based on fracture occurrence and
671 types are provided on the right. Photos are from the following stratigraphic locations: A
672 – 9 m, B- 8.5 m, C- 6.25 m, D – 5 m, and E – 3.25 m. In outcrop deformation bands are
673 observed in the Navajo Sandstone. Shear fractures and veins are observed in Carmel
674 Formation.
675
676 Figure 4. Stratigraphic column and data used to define mechano-stratigraphic units from
677 the Navajo Sandstone and Carmel Formation. Data shown are in the stratigraphy
678 modeled in this paper and the mechano-stratigraphic divisions were previously
679 determined from Petrie et al., 2012. Each mechano-stratigraphic units shares
680 similarities in bed thickness, fracture distribution, air permeability, and unconfined
681 compressive strength based on Schmidt Hammer rebound values.
682
683 Figure 5. Map of the sources of the borehole data used to derive elastic moduli. Data
684 from 43-015-30232 was used in the models presented here. Map modified from
685 (Doelling, 2002a; Hintze et al., 2000; Petrie et al., 2012)
686
687 Figure 6. Model layering schematic depicting the observations in outcrop and wireline
688 logs used to populate the model domain with mechanical properties and unit thickness.
689 A) Model I is a 3-layer model based on mechano-stratigraphic units identified by outcrop
690 analysis. B) Model II is based on observed shifts in lithology from Gamma Ray logs, and
691 variations elastic properties.
692
693 Figure 7. Model configuration showing applied boundary and pressure conditions for the
694 FEM scenarios. A) Model I - three-layer model and B) Model II – five-layer model. Both
695 models have a distribution of material properties based on layer thickness, a fixed base,
696 a vertical stress equal to Sv, and horizontal stress equal to Sh on all vertical margins.
697 No deformation occurs in the x-axis direction and a fixed base prevents all displacement
698 and rotation on the basal nodes.
699
700 Figure 8. A) Rose diagrams of strike orientation data showing the two fracture sets and
701 common orientations observed between the Navajo Sandstone and Carmel Formation.
702 B) Stereographic projection of poles to planes of fractures within the limestone and shale
703 facies of the Carmel Formation.
704
705 Figure 9. Numerical modeling results for plane strain Model I. Vertical strain profile
706 values derived from observation points taken near the center of the model, shown by red
707 line on block diagram. Fracture density from outcrop scanline data shown at far right.
708
709 Figure 10. Numerical modeling results for plane strain Model II. Vertical strain profile
710 values derived from observation points taken near the center of the model, shown by red
711 line on block diagram. Fracture density from outcrop scanline data shown at far right.
712
713 Figure 11. Modified Mohr-Coulomb-Griffith relationships showing interaction between
714 rock properties and stress. A. In outcrop, shear, extensional shear and extensional
715 fractures have been observed. B. Failure mode will depend on the state of stress or

716 rock material properties (i.e. shape of the failure envelope). Purely extensional fractures
717 are limited to a small range of orientations relative to the least principal stress, and the
718 rest of the region, extensional-shear fractures are predicted. □1 and □3 are the
719 maximum and least principal stresses; □e-s is dip of extensional shear fracture and □s
720 is dip of shear fractures. (Modified from Sibson, 2006).
721
722 Table 1. Model parametres.
723

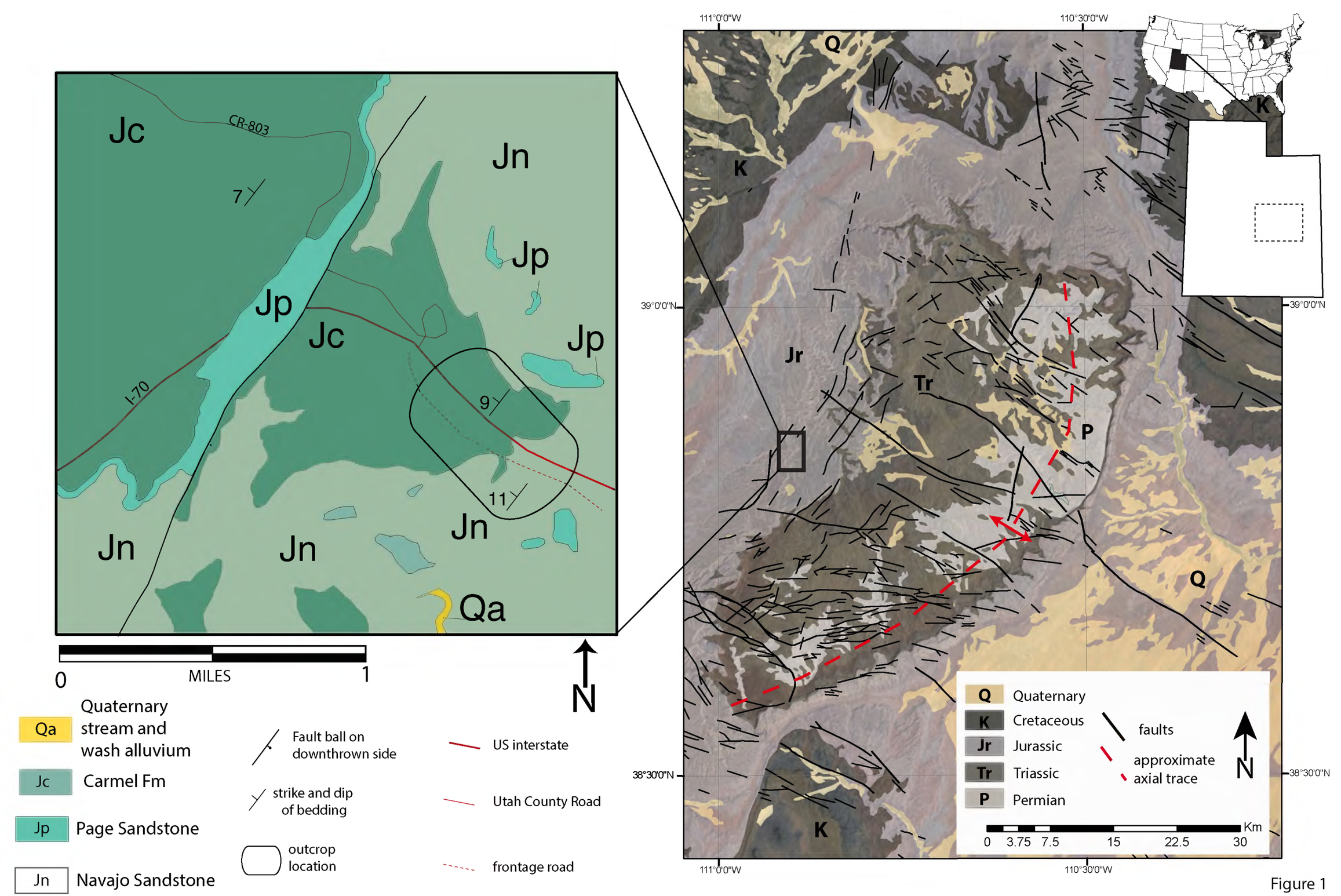
Jc
CR-803
7
Jn
Jp
Jp
Jc
Jp
I-70
9
11
Jn
Jn
Jn
Qa
0
MILES
1
N
Qa Quaternary stream and wash alluvium
Jc Carmel Fm
Jp Page Sandstone
Jn Navajo Sandstone
Fault ball on downthrown side
strike and dip of bedding
outcrop location
US interstate
Utah County Road
frontage road
111°0'0"W
110°30'0"W
39°0'0"N
38°30'0"N
Q
K
Jr
Tr
P
K
Q
K
Q Quaternary
K Cretaceous
Jr Jurassic
Tr Triassic
P Permian
faults
approximate axial trace
N
0 3.75 7.5 15 22.5 30
Km

Figure 1

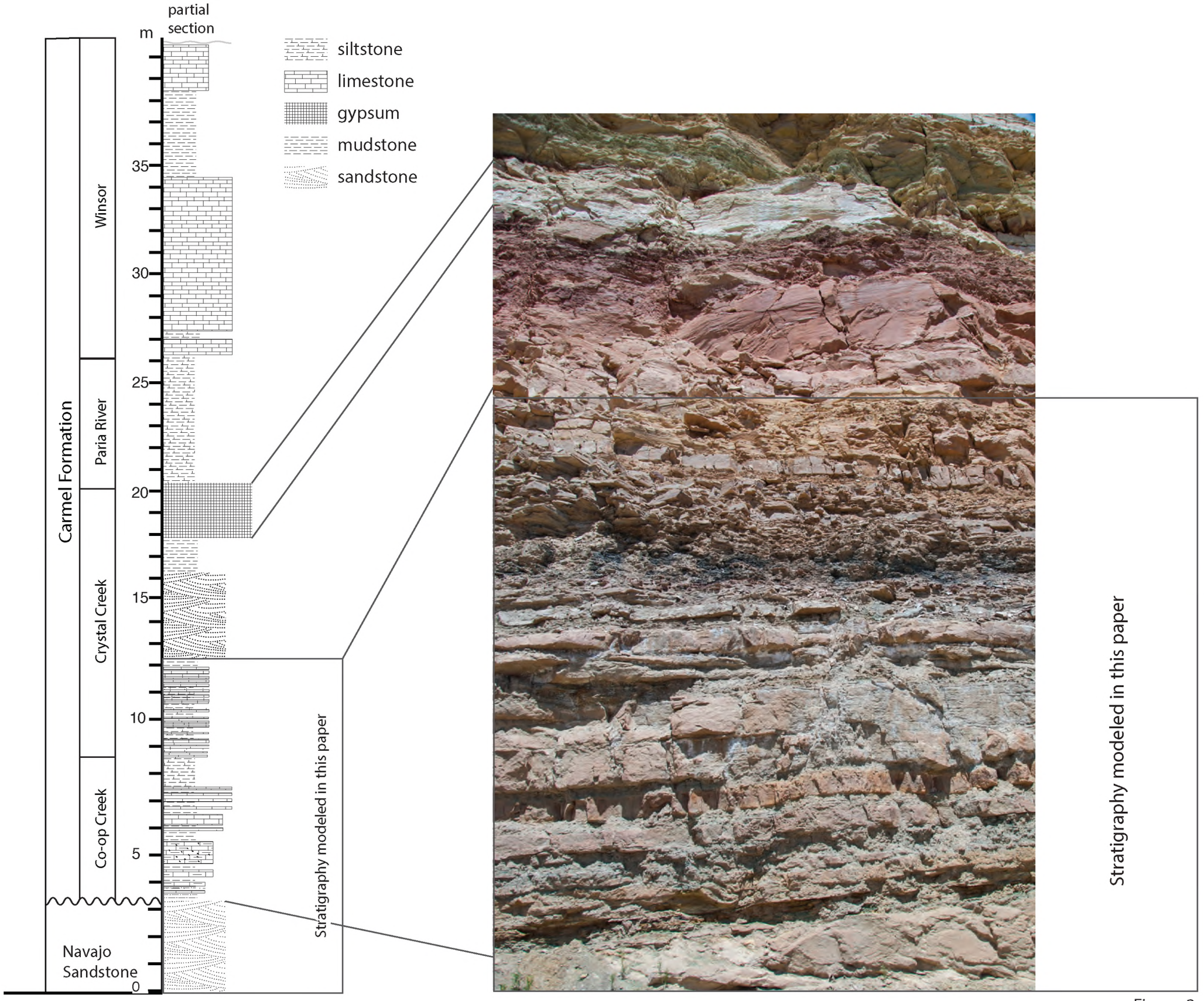
partial section
m
siltstone
limestone
gypsum
mudstone
sandstone
Carmel Formation
Winsor
Paria River
Crystal Creek
Co-op Creek
Navajo Sandstone
35
30
25
20
15
10
5
0
Stratigraphy modeled in this paper
Stratigraphy modeled in this paper

Figure 2

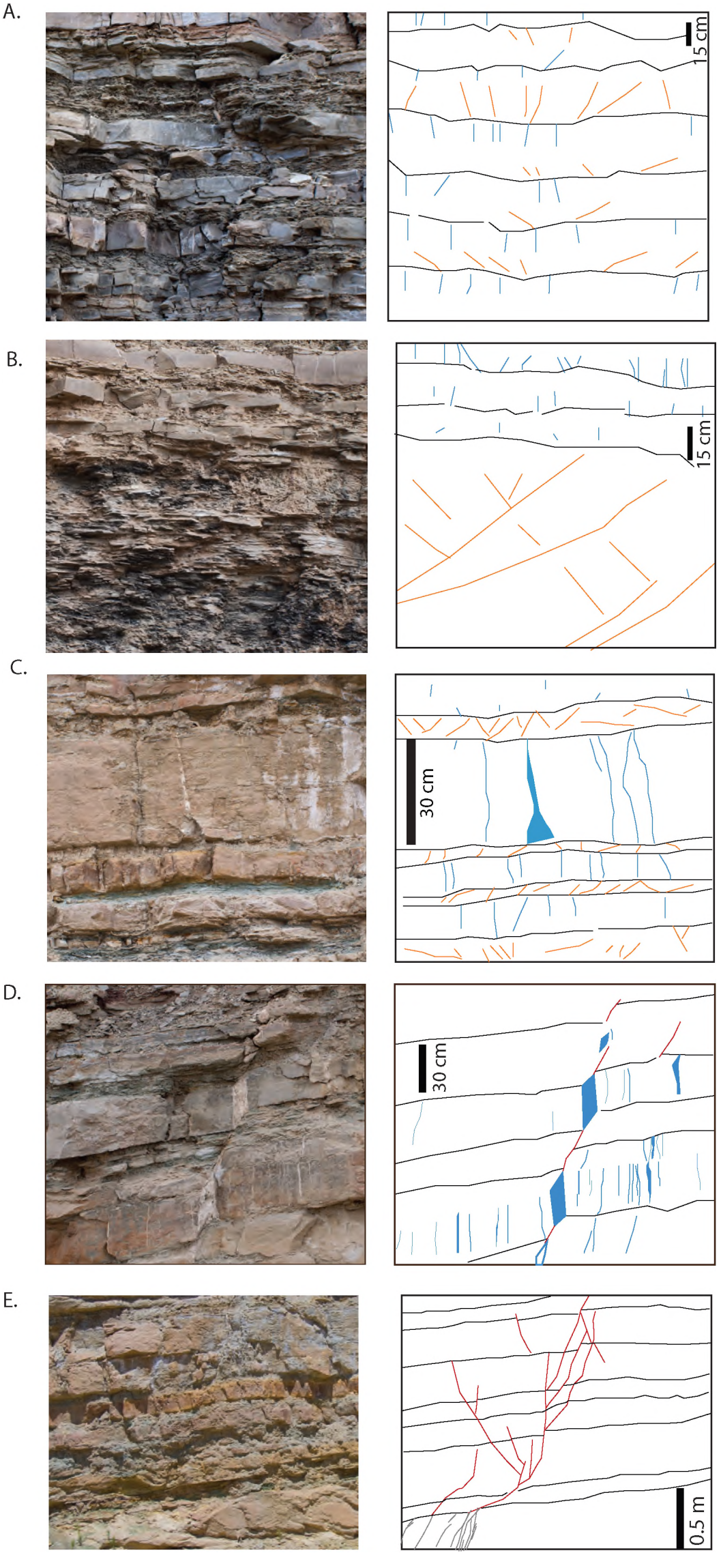
A.
15 cm
B.
15 cm
C.
30 cm
D.
30 cm
E.
0.5 m
shear fractures
deformation bands
calcite veins
fractures in shale limonite margins with calcite veins
bedding

Figure 3

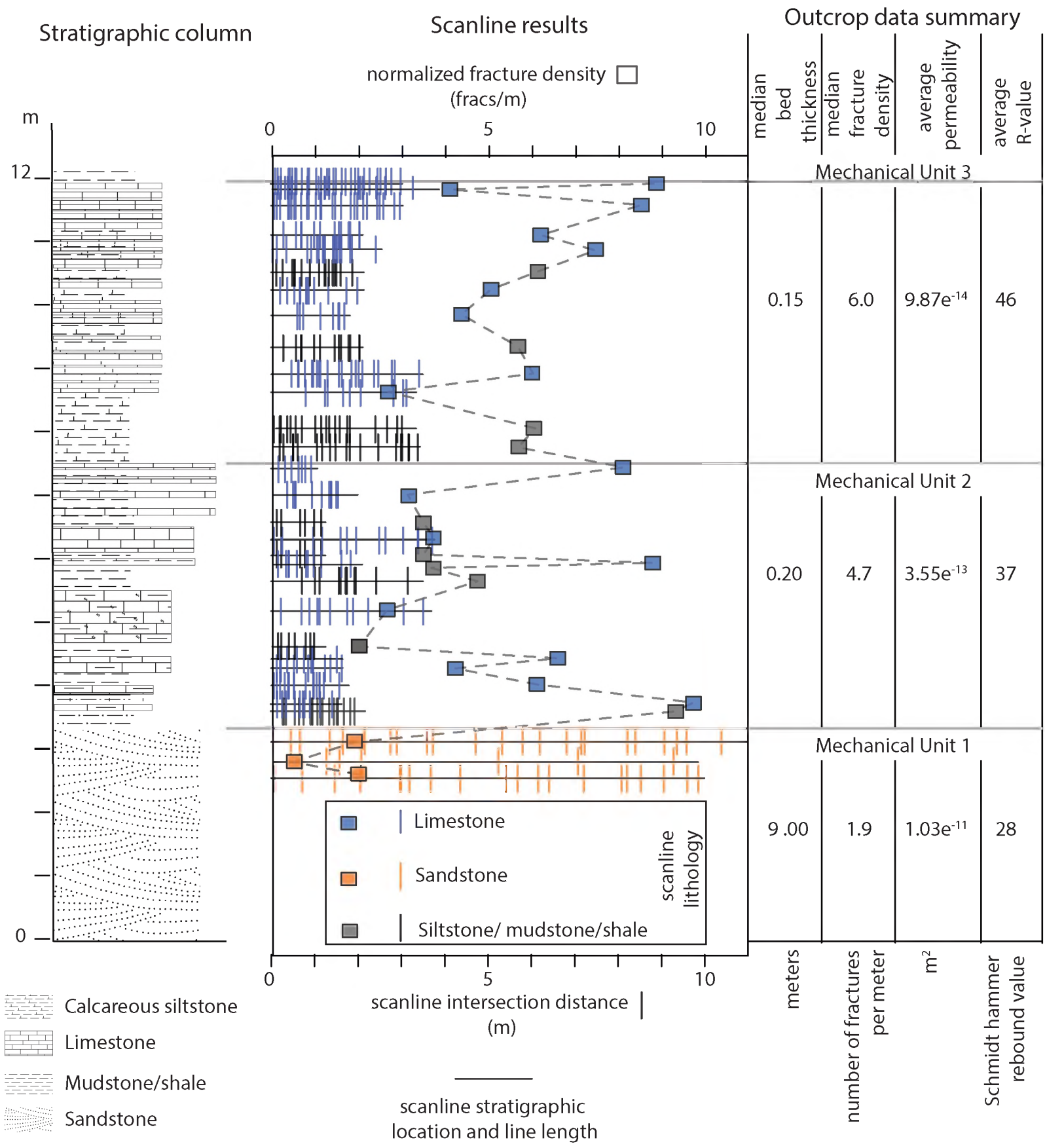
Stratigraphic column
Scanline results
Outcrop data summary
normalized fracture density
(fracs/m)
m
12
0
0
5
10
median bed thickness
median fracture density
average permeability
average R-value
Mechanical Unit 3
Mechanical Unit 2
Mechanical Unit 1
0.15
6.0
9.87e-14
46
0.20
4.7
3.55e-13
37
9 .00
1.9
1.03e-11
28
Limestone
Sandstone
Siltstone/ mudstone/shale
scanline lithology
scanline intersection distance
(m)
meters
number of fractures per meter
m2
Schmidt hammer rebound value
Calcareous siltstone
Limestone
Mudstone/shale
Sandstone
scanline stratigraphic location and line length

Figure 4

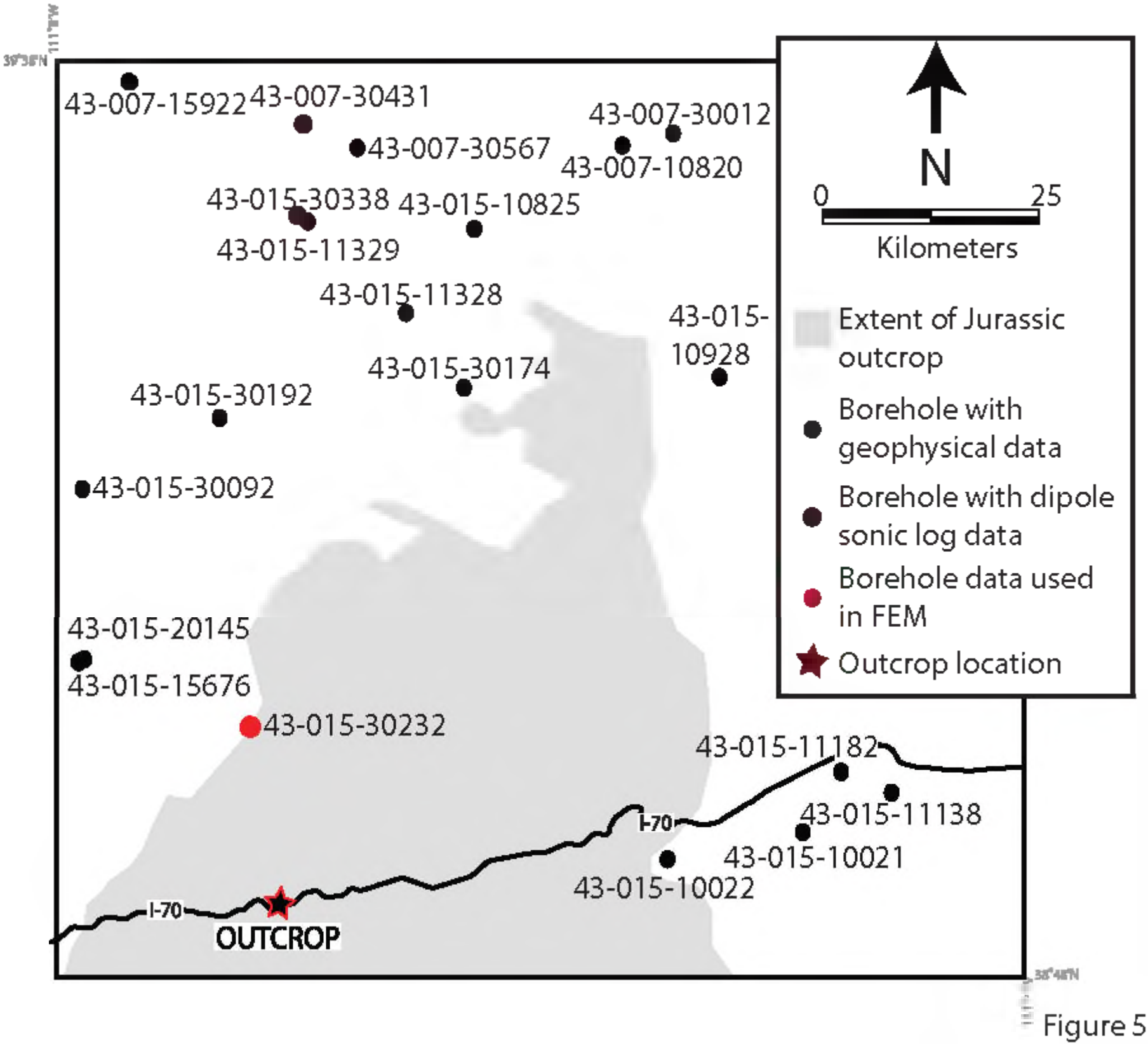
43-007-15922
43-007-30431
43-007-30567
43-007-30012
43-007-10820
43-015-30338
43-015-10825
43-015-11329
43-015-11328
43-015-10928
43-015-30174
43-015-30192
43-015-30092
43-015-20145
43-015-15676
43-015-30232
43-015-11182
43-015-11138
43-015-10021
43-015-10022
I-70
I-70
OUTCROP
N
0
25
Kilometers
Extent of Jurassic outcrop
Borehole with geophysical data
Borehole with dipole sonic log data
Borehole data used in FEM
Outcrop location

Figure 5

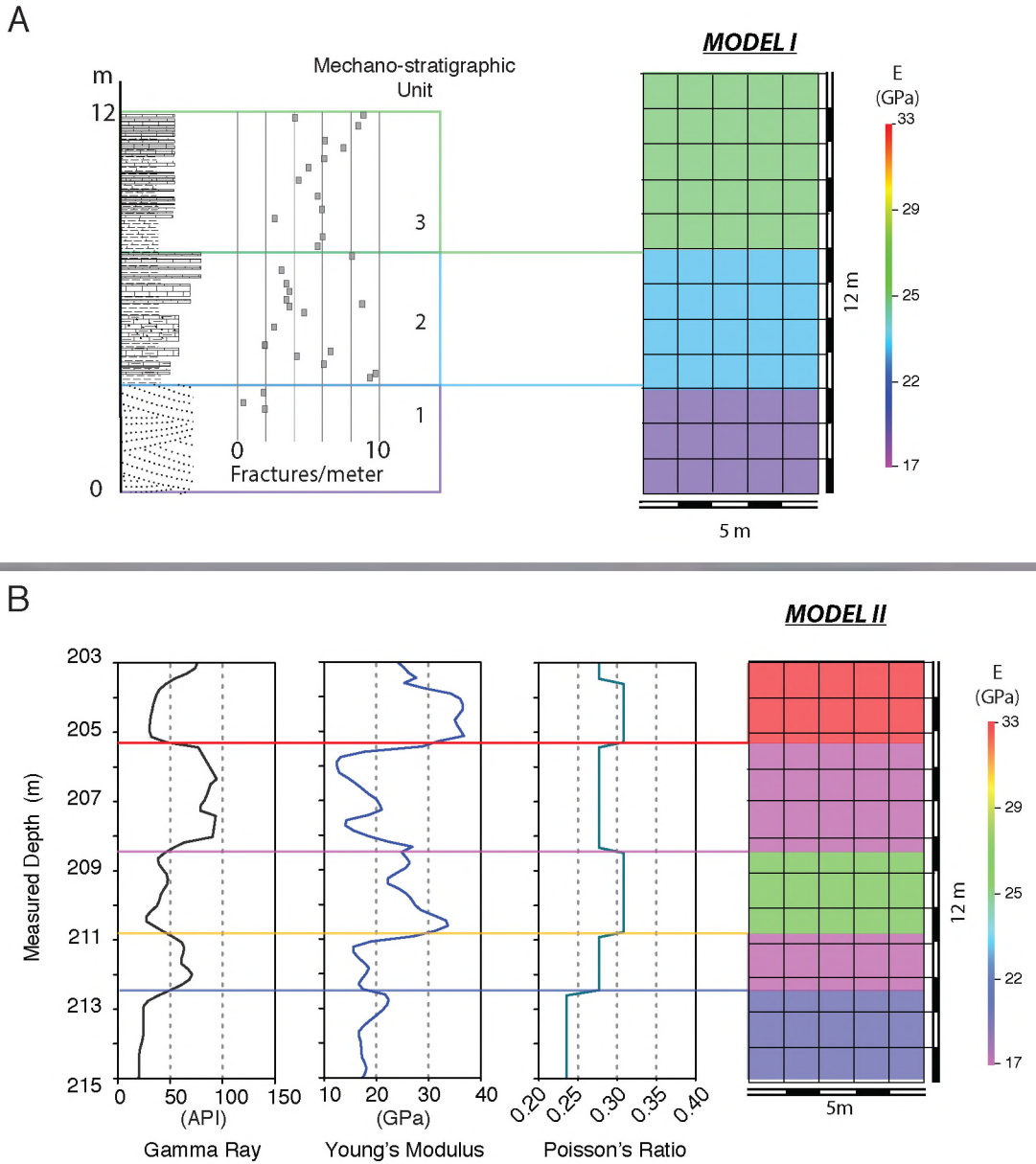
A
MODEL I
m
12
0
Mechano-stratigraphic Unit
3
2
1
0
10
Fractures/meter
E (GPa)
33
29
25
22
17
12 m
5 m
B
MODEL II
Measured Depth (m)
203
205
207
209
211
213
215
0
50
100
150
(API)
Gamma Ray
10
20
30
40
(GPa)
Young's Modulus
0.20
0.25
0.30
0.35
0.40
Poisson's Ratio
E (GPa)
33
29
25
22
17
12 m
5m

Figure 6

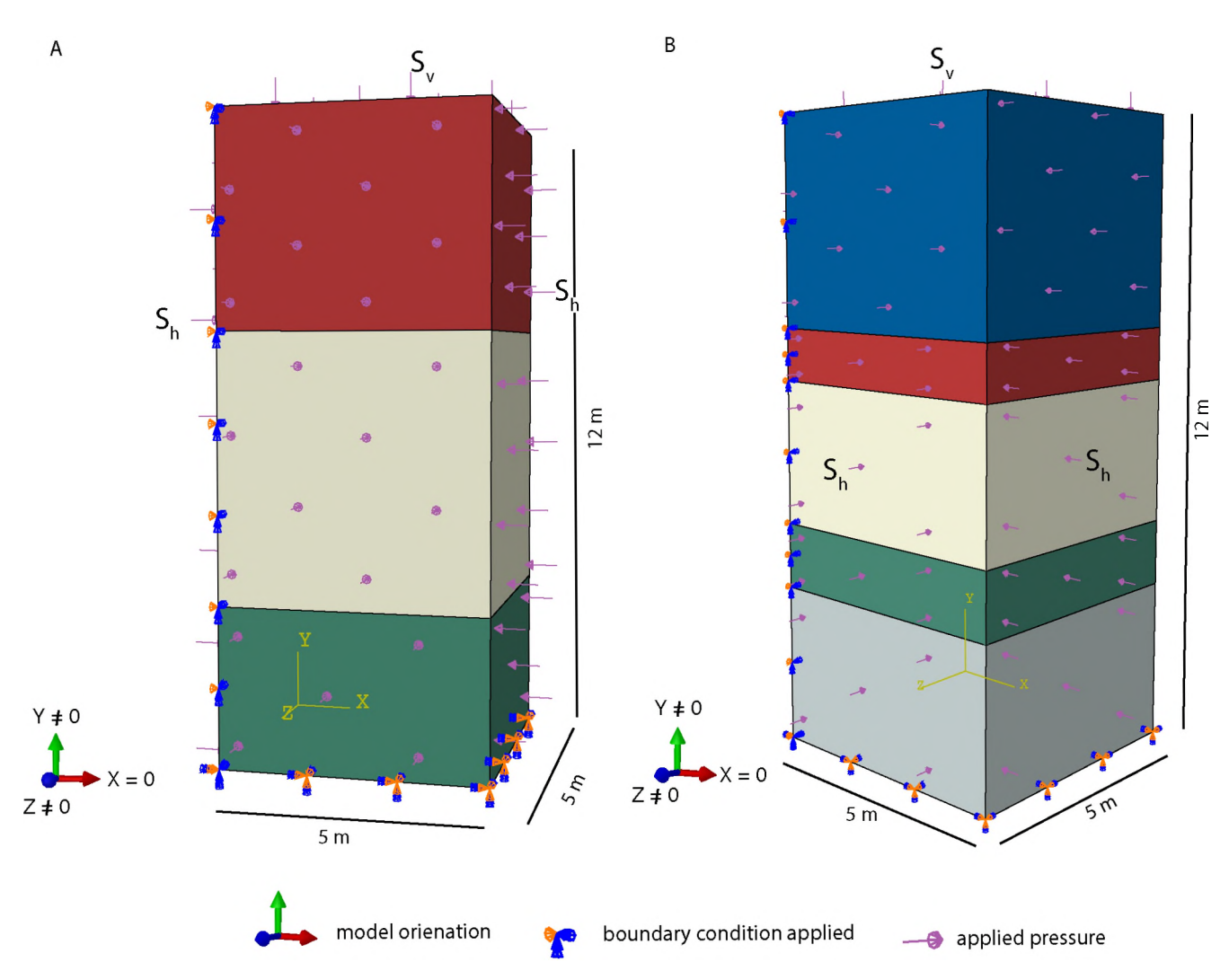
A
S_v
S_h
S_h
12 m
5 m
5 m
Y
X
Z
Y ≠ 0
X = 0
Z ≠ 0
B
S_v
S_h
S_h
12 m
5 m
5 m
Y
X
Z
Y ≠ 0
X = 0
Z ≠ 0
model orienation
boundary condition applied
applied pressure

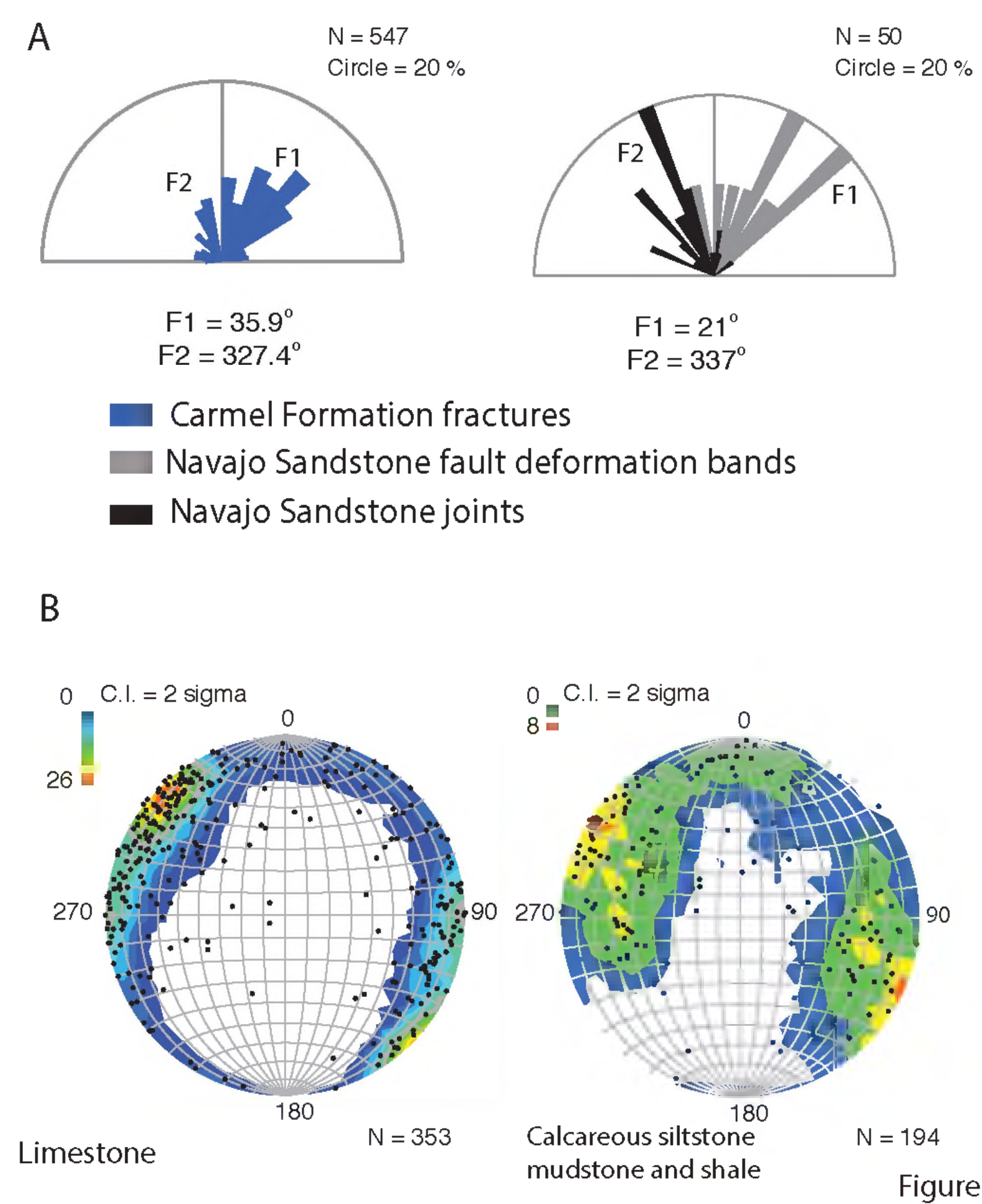
A
N = 547
Circle = 20 %
F1
F2
F1 = 35.9°
F2 = 327.4°
N = 50
Circle = 20 %
F2
F1
F1 = 21°
F2 = 337°
Carmel Formation fractures
Navajo Sandstone fault deformation bands
Navajo Sandstone joints
B
0
C.I. = 2 sigma
26
0
270
90
180
N = 353
Limestone
0
C.I. = 2 sigma
8
0
270
90
180
Calcareous siltstone
mudstone and shale
N = 194

Figure 8

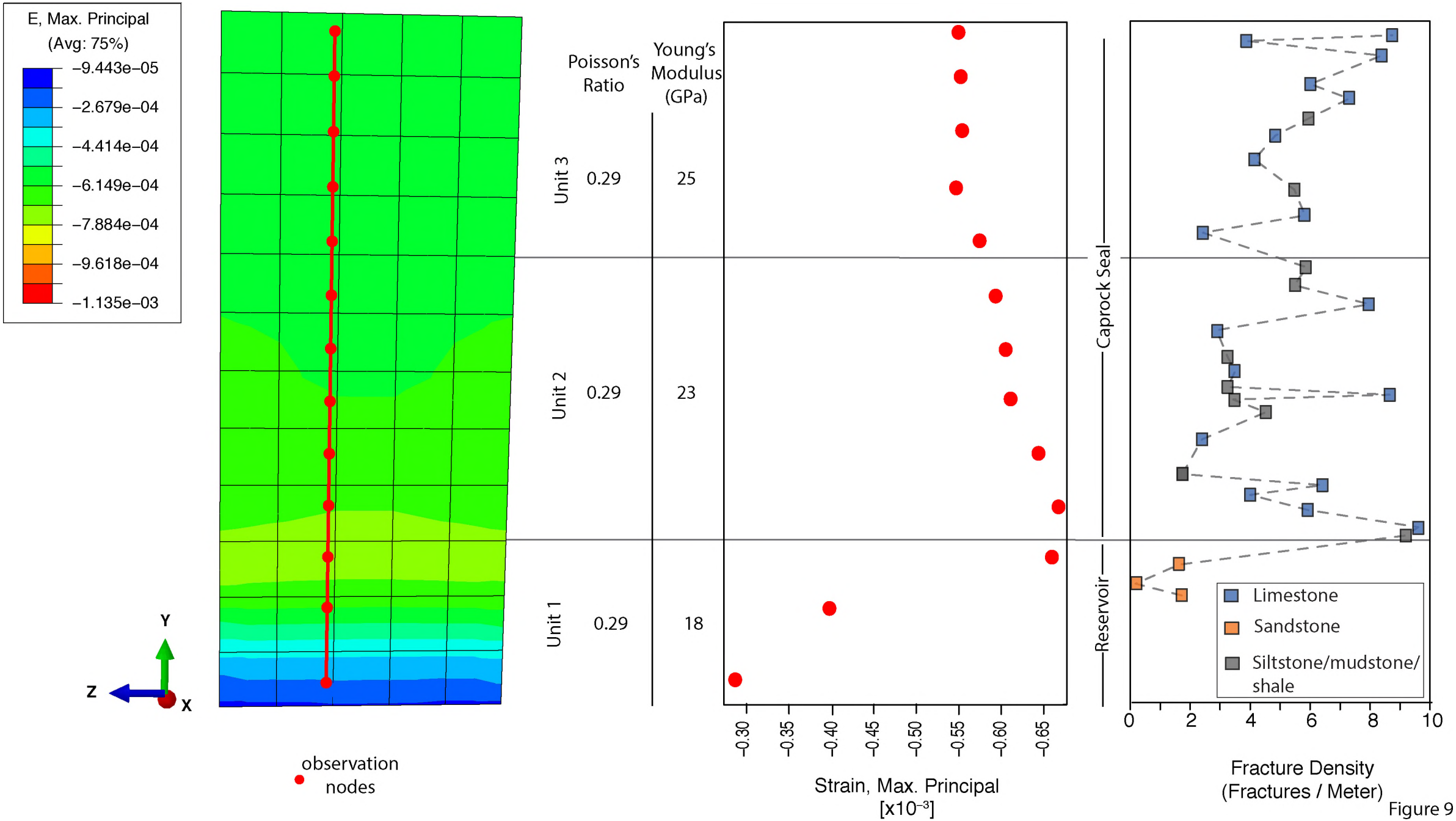
E, Max. Principal
(Avg: 75%)
−9.443e−05
−2.679e−04
−4.414e−04
−6.149e−04
−7.884e−04
−9.618e−04
−1.135e−03
Y
Z
X
observation nodes
Poisson's Ratio
Young's Modulus (GPa)
Unit 3
0.29
25
Unit 2
0.29
23
Unit 1
0.29
18
−0.30
−0.35
−0.40
−0.45
−0.50
−0.55
−0.60
−0.65
Strain, Max. Principal [x10⁻³]
Caprock Seal
Reservoir
Limestone
Sandstone
Siltstone/mudstone/ shale
0
2
4
6
8
10
Fracture Density (Fractures / Meter)

Figure 9

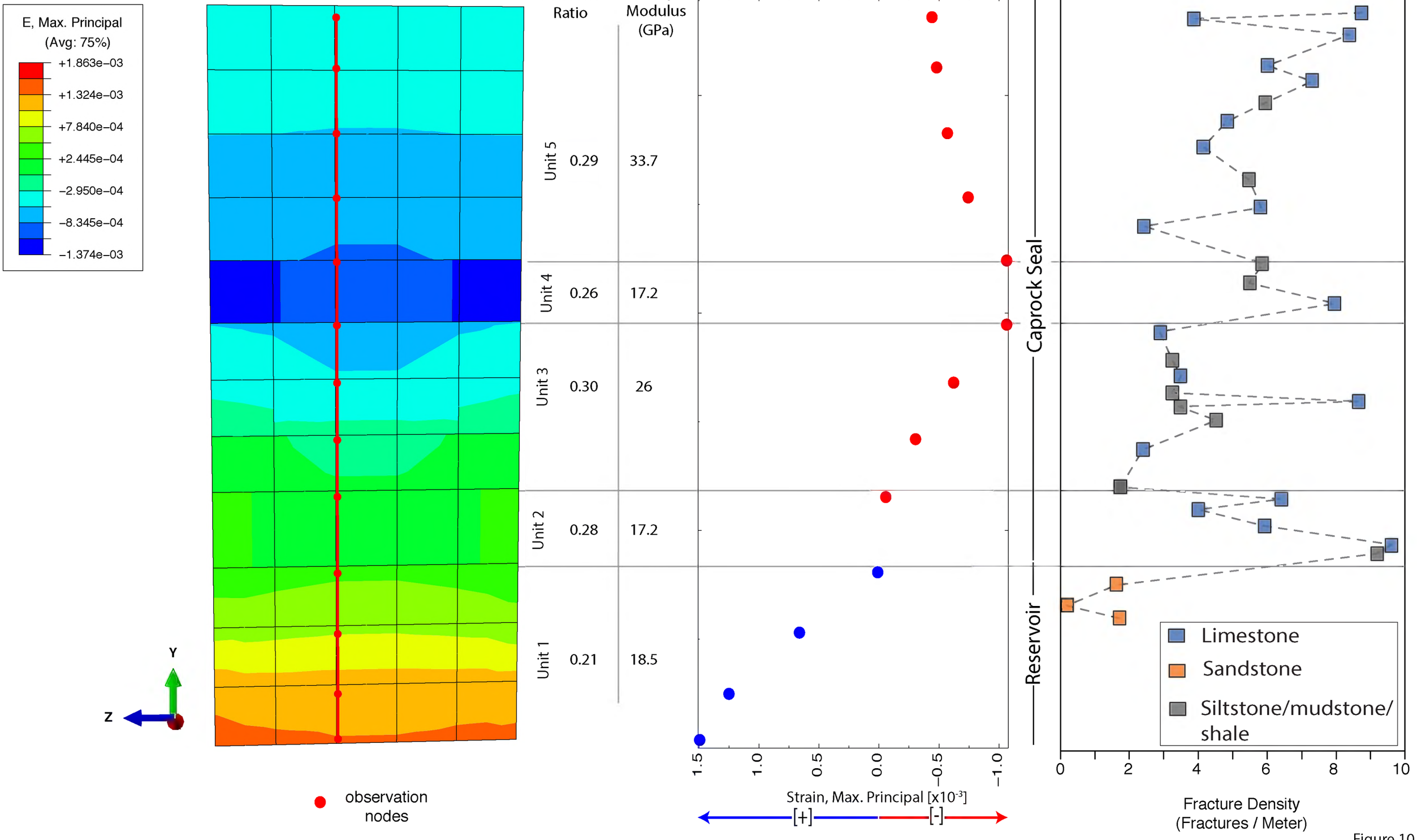
E, Max. Principal
(Avg: 75%)
+1.863e−03
+1.324e−03
+7.840e−04
+2.445e−04
−2.950e−04
−8.345e−04
−1.374e−03
Poisson's Ratio
Young's Modulus (GPa)
Unit 5
0.29
33.7
Unit 4
0.26
17.2
Unit 3
0.30
26
Unit 2
0.28
17.2
Unit 1
0.21
18.5
Caprock Seal
Reservoir
Y
Z
observation nodes
1.5
1.0
0.5
0.0
−0.5
−1.0
Strain, Max. Principal [x10-3]
[+]
[-]
0
2
4
6
8
10
Fracture Density (Fractures / Meter)
Limestone
Sandstone
Siltstone/mudstone/ shale

Figure 10

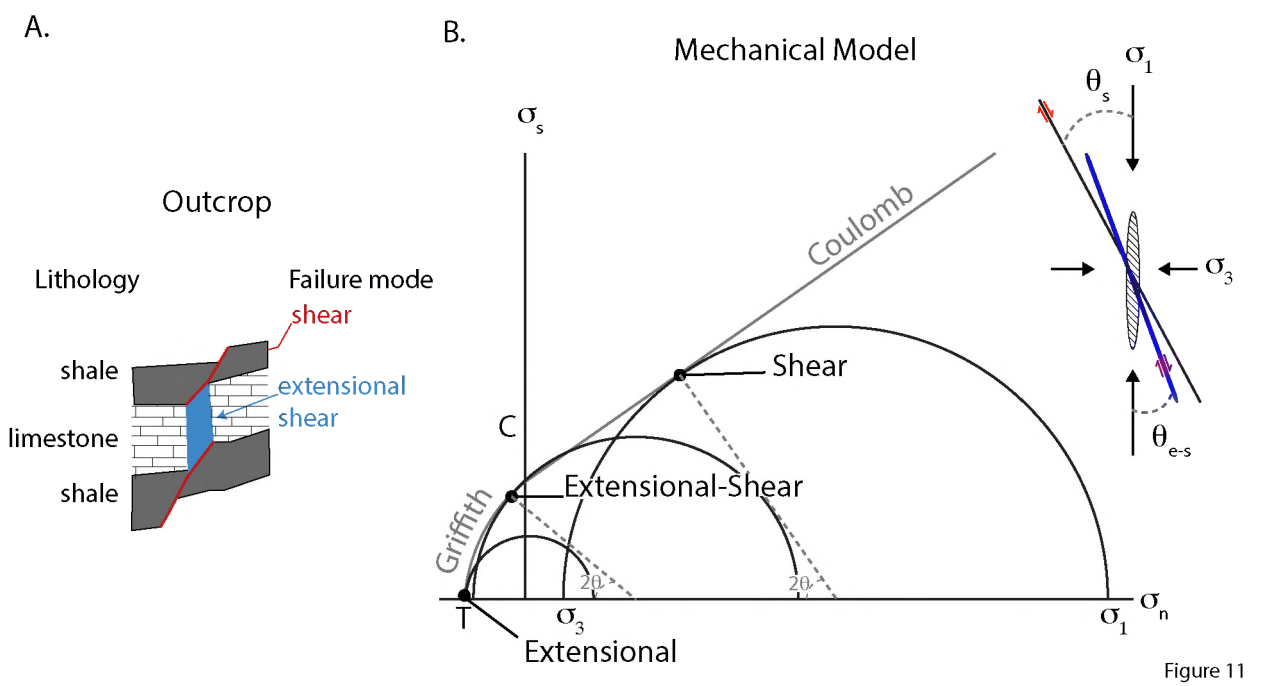
A.
Outcrop
Lithology
Failure mode
shear
shale
extensional
shear
limestone
shale
B.
Mechanical Model
σs
σ1
θs
Coulomb
σ3
Shear
C
Extensional-Shear
θe-s
Griffith
2θ
2θ
T
σ3
σ1
σn
Extensional

Figure 11